Distribution Agreement

In presenting this thesis or dissertation as a partial fulfillment of the requirements for an advanced degree from Emory University, I hereby grant to Emory University and its agents the non-exclusive license to archive, make accessible, and display my thesis or dissertation in whole or in part in all forms of media, now or hereafter known, including display on the world wide web. I understand that I may select some access restrictions as part of the online submission of this thesis or dissertation. I retain all ownership rights to the copyright of the thesis or dissertation. I also retain the right to use in future works (such as articles or books) all or part of this thesis or dissertation.

Signature:

_____ _____

Alicia Lane Date

Signaling mechanisms upregulating protein synthesis ameliorate neuronal phenotypes caused by copper deficiency

By

Alicia Lane
Doctor of Philosophy

Graduate Division of Biological and Biomedical Science
Neuroscience

Approved by:

_____
Victor Faundez, MD, PhD
Advisor
School of Medicine, Department of Cell Biology

_____
William (Mike) Caudle, PhD
Committee Member
Rollins School of Public Health, Department of Environmental Health

_____
Jennifer Kwong, PhD
Committee Member
School of Medicine, Department of Pediatrics

_____
Steven Sloan, MD, PhD
Committee Member
School of Medicine, Department of Human Genetics

_____
Peter Wenner, PhD
Committee Member
School of Medicine, Department of Cell Biology

Accepted:

_____
Kimberly Jacob Arriola, PhD, MPH
Dean of the James T. Laney School of Graduate Studies

_____
Date

Signaling mechanisms upregulating protein synthesis ameliorate neuronal phenotypes caused by copper deficiency

By

Alicia Lane
B.S., Georgia Institute of Technology, 2015

Advisor: Victor Faundez, MD, PhD

An abstract of
A dissertation submitted to the Faculty of the
James T. Laney School of Graduate Studies of Emory University
in partial fulfillment of the requirements for the degree of
Doctor of Philosophy
in Neuroscience
2025

Abstract

Signaling mechanisms upregulating protein synthesis ameliorate neuronal phenotypes caused by copper deficiency

By Alicia Lane

Copper homeostasis is essential for neuronal functions from neurotransmitter synthesis to oxidative phosphorylation (the main supplier of energy for the nervous system). Copper is required to help the brain meet its high energy demands and plays a particularly important role in neurodevelopment, as there is a shift after birth toward mitochondrial respiration over glycolysis. Rare inherited diseases caused by mutations in the copper transporters *SLC31A1* (CTR1) or *ATP7A* induce copper deficiency in the brain and throughout the body, causing seizures and neurodegeneration in infancy through poorly understood disease mechanisms. In this dissertation, I describe a method for quantifying trace metals in biological samples and characterize three model systems to investigate the molecular mechanisms downstream of copper deficiency in neuronal cells. CTR1-null human neuroblastoma cells exhibit copper-dependent impairments in mitochondrial enzymes, leading to decreases in oxidative phosphorylation and increased glycolysis. Multiomics analysis of these cells at the protein and RNA level and corroborative immunoblots identified elevated mTORC1 and S6K activation, reduced PERK signaling, and downstream increased protein synthesis in CTR1-null cells. Pharmacological manipulation of these cells suggests that mTOR activation and increased protein synthesis is a pro-survival response to copper deficiency. These findings were corroborated in vivo in mouse and *Drosophila*. Spatial transcriptomic profiling of $Atp7a^{flx/Y}$ :: $Vil1^{Cre/+}$ mice, which model brain copper deficiency due to impaired absorption of dietary copper, identified upregulated protein synthesis machinery and mTORC1-S6K pathway genes in mutant Purkinje neurons before the onset of neurodegeneration. Pathological epidermis phenotypes in *Drosophila* caused by ATP7 overexpression (inducing copper extrusion) are intensified by RNAi against the mTOR pathway genes Akt, S6k, or raptor. Dendritic phenotypes in copper deficient class IV neurons are partially rescued by either of two genetic mTOR pathway manipulations (S6k overexpression or Thor RNAi) that ultimately increase protein synthesis. Together, this body of work points to increased mTORC1-S6K pathway activation and protein synthesis as an adaptive mechanism by which neuronal cells respond to copper deficiency. More broadly, these data demonstrate the interconnectivity of copper homeostasis, metabolism, and bioenergetics in neuronal cells and the particular importance of these processes during critical time periods in early neurodevelopment.

Signaling mechanisms upregulating protein synthesis ameliorate neuronal phenotypes caused by copper deficiency

By

Alicia Lane
B.S., Georgia Institute of Technology, 2015

Advisor: Victor Faundez, MD, PhD

A dissertation submitted to the Faculty of the
James T. Laney School of Graduate Studies of Emory University
in partial fulfillment of the requirements for the degree of
Doctor of Philosophy
in Neuroscience
2025

Dedication

In loving memory of Tim.

Acknowledgments

Neither life nor science make narrative sense unless we give it meaning. Thank you to everyone who made this a story and not just a destination.

To Paco et al.: Thank you for helping me build the confidence and skills that I needed to get my PhD. You helped me feel like a “real” scientist and enter graduate school with a running start, with lifelong friends and colleagues to help me along the way.

To Victor and my lab: It has been an incredible experience to get my PhD surrounded by stellar scientists who are also stellar human beings. Thank you for your unwavering kindness and compassion, for giving me the space to learn and grow within a supportive and nurturing lab environment, which let me bravely venture into the unknown (i.e. the once dreaded but now routine Western blot, literally and metaphorically).

To my committee (Mike, Jen, Steven, and Pete): I have had the unusual experience of always looking forward to my committee meetings. Your enthusiasm and insights into this project (and for me as a scientist) drove this project (and me) to greater heights than I could have imagined. Thank you for sharing in the joy and excitement of this scientific journey with me. Thank you for not giving me the easy answers when I asked and instead helping me figure out the answers on my own. You helped me navigate the scientific and personal landscape of my PhD and become a better scientist with a better understanding of myself.

To the Emory neuroscience community: You are the reason I chose to do my graduate studies at Emory and are the reason I chose to stay for my postdoc. In the imaginary and impossible scenario of somehow managing to find a time that every one of us was available, if we were to all sit in a circle, I could say “Look to your left. Now look to your right. Both of the people sitting next to you are incredible scientists and wonderful people”, and that would be a true and accurate statement. I am so incredibly grateful to have spent the last 10 years surrounded by such talented, creative, collaborative driven, caring, compassionate scientists. You help give me

faith in science, in academia, in humanity. Thank you for all that you have done to support me in my journey and to build a community at Emory to help neuroscientists learn and thrive.

To my friends and family: Thank you for letting me monologue about copper. Thank you for lovingly keeping me from getting too deep in the weeds of my project, when I forgot that most people don't know what the word "aliquot" means and that there is a world outside the lab where you can feel the sun and touch grass and relax. Thank you for bringing laughter and joy and peace into my life when grad school and the universe conspired to make me a giant wound-up ball of stress. Thank you to everyone who talked books, played stupid video games, or played extremely long and complicated board games with me; thank you to everyone who met up with me for coffee/lunch/dinner and chitchat; thank you to everyone who walking/hiking with me. This has been a tremendously difficult journey—thank you for holding my hand through it all and bringing joy and laughter into my life. (And to my dad: Thank you for your decades-long streak of being my and everyone else's Dad Of The Year. I credit the care and compassion you have for the world and the people around you for helping me become the woman I am today. You are the reason I am the only millennial whose phone app is one of her top used apps.)

To Luke and Devi: Words can't convey all of the gratitude that I have for you. You bring so much joy to my life in ways that I never could have imagined. I might have been able to make it this far without you, but it would have been with a lot less joy, laughter, travel, adventure, and peace… and a lot more frozen pizzas. Luke, thank you for making my world bigger and exploring it with me. Devi, thank you for being the best serotonin support animal I could ask for.

To the Robert W. Woodruff Fellowship Program, ARCS Foundation (in particular, Patty and Doug Reid), and John B. Lyon and family: I would have graduated with significant student loan and medical debt without your support. I cannot overstate the impact that you had on me and my family over the last 5 years. From the bottom of my heart, thank you for your generosity and belief in me (and in science).

And finally, to me: I am so proud of all of the work that brought me to this moment. I want to acknowledge the privilege that helped me throughout professional journey—always having role models that looked like me and spoke like me; studying in my native language surrounded by a culture familiar to me; having relative financial security, a supportive family, and a safety net if needed; and not having chronic pain or other health problems that significantly impacted my academic studies or personal life are just a few examples of challenges that I did not have to face simply due to the circumstances to which I was born. At times the pace feels glacial, but I have hope that we are slowly dismantling the systems that impede brilliant minds who have worked just as hard or harder than I have from being able to pursue a career in science. Two decades of education has left me with a firm belief in knowledge as a tool of empowerment; may I live to see a world where knowledge is celebrated and accessible to all.

> “This may not seem to you like a world for scholars, my dear friend, but I think you’ll be proven wrong. It seems to me that now—suffering in the darkness that might just be the end of everything—is when we need knowledge the most.”
>
> – Brandon Sanderson, *The Hero of Ages*

Table of Contents

List of Figures

Figures are numbered starting from 1 within each chapter.

Chapter 1

Chapter 2

Chapter 3

Chapter 4

List of Tables

Tables are numbered starting from 1 within each chapter.

Chapter 1

Chapter 2

Chapter 3

List of Symbols and Abbreviations

GENERAL	
AMP	Adenosine monophosphate
ADP	Adenosine diphosphate
ATP	Adenosine triphosphate
GTP	Guanosine triphosphate
NMDA	N-methyl-D-aspartate (glutamate receptor)
AMPA	alpha-amino-3-hydroxy-5-methyl-4-isoxazolepropionate (glutamate receptor)
GABA	Gamma-aminobutyric acid
TCA	Citric acid cycle, Krebbs cycle
ETC	Electron transport chain
FDA	U.S. Food and Drug Administration
METHODS/TOOLS/STATISTICAL ANALYSIS	
AGC	Automatic gain control
AOI	Areas of illumination
BEH	Ethylene Bridged Hybrid
CV	Compensative voltage
CRISPR	Clustered regularly interspaced short palindromic repeats
ECAR	Extracellular acidification rate
ENRICHR	Gene list enrichment analysis software tool
FC	Fold change
GIS	Global internal standard
GO	Gene ontology
GSEA	Gene set enrichment analysis
GWAS	Genome-wide association study(ies)

HCD	Higher energy collision-induced dissociation
HLB	Hydrophilic-lipophilic balanced
ICP-MS	Inductively coupled plasma mass spectrometry
ID	Inner diameter
KEGG	Kyoto Encyclopedia of Genes and Genomes database
KO	Knockout
LOQ2	Limit of Quantitation
MSigDB	Molecular Signatures Database
mWTA	Mouse Whole Transcriptome Atlas
NES	normalized enrichment score
OCR	Oxygen consumption rate
OMIM	Online Mendelian Inheritance in Man resource
PCA	Principal component analysis
PCR	Polymerase chain reaction
Q3	Third quantile
R	R coding language
ROI	Regions of interest
RT	Room temperature
SILAC	Stable isotope labeling by amino acids in cell culture
TMT-MS	Tandem mass tag mass spectrometry
ZIP	Zero Interaction Potency score
REAGENTS/COMPOUNDS	
2-DG	2-deoxy-D-glucose
ACN	Anhydrous acetonitrile
BCA	Bicinchoninic acid

BCS	Bathocuproinedisulfonic acid disodium salt
DDM	n-dodecyl β-D-maltoside
DMEM	Dulbecco's Modified Eagle Medium
DTT	1,4-dithiothreitol
EDTA	Ethylenediaminetetraacetic acid
FA	Formic acid
FBS	Fetal bovine serum
HEPES	4-(2-Hydroxyethyl)piperazine-1-ethane-sulfonic acid
IAA	Iodoacetamide
PBS	Phosphate buffered saline
PVDF	Polyvinylidene difluoride
TBS/TBST	TRIS-Buffered Saline (TBS) with Triton X-100 (TBST)
TEAB	Triethylammonium bicarbonate
TFA	Trifluoroacetic acid
CELL LINES	
C-6	Rat glioma cell line
PC-12	Rat medulla pheochromocytoma cell line
SH-SY5Y	Human neuroblastoma cell line
GENE/PROTEIN NAMES	
AARS	Alanyl-tRNA synthetase 1
ACLY	ATP citrate lyase
ACTB	Actin beta
Adcy1	Adenylate cyclase 1
AHCTF1	AT-hook containing transcription factor 1
AKT	AKT serine/threonine kinase family (containing AKT1, AKT2, AKT3)

AKT1S1	AKT1 substrate 1
Aldoc	Aldolase, fructose-bisphosphate C
AMPK	AMP-activated protein kinase complex
APOE	Apolipoprotein E
APP	Amyloid beta precursor protein
Aqp4	Aquaporin 4
ARAF	A-Raf proto-oncogene, serine/threonine kinase
ARHGAP18/26/42	Rho GTPase activating protein 18/26/42
ARHGEF2/33	Rho/Rac guanine nucleotide exchange factor 2/33
ATAD3A/B	ATPase family AAA domain containing 3A/B
ATOX1	Antioxidant 1 copper chaperone
ATP7A/B; ATP7	ATPase copper transporting alpha/beta; ATP7 is fly homolog
BDNF	Brain derived neurotrophic factor
C9orf72	C9orf72-SMCR8 complex subunit
Calb1	Calbindin 1
Car8/10	Carbonic anhydrase 8/10
CBEPB	CCAAT enhancer binding protein beta
Cbln1	Cerebellin 1 precursor
CCS	Copper chaperone for superoxide dismutase
Cep192	Centrosomal protein 192
CNN2	Calponin 2
COA3/4/5/6/7	Cytochrome c oxidase assembly factor 3/4/5/6/7
Cobll1	Cordon-bleu WH2 repeat protein like 1
COX4	Cytochrome c oxidase subunit 4 (COX4I1/2)
COX5B	Cytochrome c oxidase subunit 5B

COX6A1	Cytochrome c oxidase subunit 6A1
COX6C	Cytochrome c oxidase subunit 6C
COX7A2	Cytochrome c oxidase subunit 7A2
COX7C	cytochrome c oxidase subunit 7C
COL14A	Collagen type XIV alpha 1 chain
COX11	Cytochrome c oxidase copper chaperone COX11
COX15	Cytochrome c oxidase assembly homolog COX15
COX17	Cytochrome c oxidase copper chaperone COX17
COX19	Cytochrome c oxidase assembly factor COX19
DBH	Dopamine beta-hydroxylase
DEPTOR	DEP domain containing MTOR interacting protein
Dner	Delta/notch like EGF repeat containing
E2F1	E2F transcription factor 1
EGFR	Epidermal growth factor receptor
EIF2α/eIF2α	Eukaryotic translation initiation factor 2 α
EIF2AK3/PERK	Eukaryotic translation initiation factor 2 alpha (EIF2α) kinase 3
EIF4G1	Eukaryotic translation initiation factor 4 gamma (EIF4λ) 1
Erdr1/Erdr1x	Erythroid differentiation regulator 1 x (*Mus musculus*)
ESRRA	Estrogen related receptor alpha
FGF1/2/14	Fibroblast growth factor 1/2/14
FNIP1/2	Folliculin interacting protein 1/2
FMR1/FRMP	Fragile X mental retardation protein (FMRP), encoded by *FMR1*
Gabra6/b1	GABA type A receptor subunit alpha6/beta1
GFAP	Glial fibrillary acidic protein
GM45929	Mef2bl; myocyte enhancer factor 2B like (*Mus musculus*)

Gpc5	Glypican 5
Gria1	Glutamate ionotropic receptor AMPA type subunit 1
Grid2	Glutamate ionotropic receptor delta type subunit 2
Grik2	Glutamate ionotropic receptor kainate type subunit 2
H4C1	H4 clustered histone 1
HIF-1, HIF1A	Hypoxia-inducible factor 1; α subunit encoded by HIF1A
HIGD2A	HIG1 hypoxia inducible domain family member 2A
HSP90	Heat shock protein 90
HTT	Huntingtin
IFITM1	Interferon induced transmembrane protein 1
IGF1R	Insulin like growth factor 1 receptor
INS/INS1	Insulin
Itpr1	Inositol 1,4,5-trisphosphate receptor type 1
Kcnd2	Potassium voltage-gated channel subfamily D member 2
LOX	Lysyl oxidase
LTC4S	Leukotriene C4 synthase
MACO1	Macoilin 1
MAPK	Mitogen-activated protein kinase family; includes extracellular signal-regulated kinases (ERKs), c-Jun N-terminal kinases (JNKs) and p38 mitogen-activated protein kinases (p38s)
MAPK1/ERK2	Mitogen-activated protein kinase 1; extracellular signal-regulated kinase 2
MAPK3/EKR1	Mitogen-activated protein kinase 3
MAST4	Microtubule associated serine/threonine kinase family member 4
Mcm2	Minichromosome maintenance complex component 2
MEK	Mitogen-activated protein kinase (MAPK) kinase family
MEK1	Mitogen-activated protein kinase (MAPK) kinase 1, encoded by *MAP2K1*

MEK2	Mitogen-activated protein kinase (MAPK) kinase 2, encoded by *MAP2K2*
MERTK	MER proto-oncogene, tyrosine kinase
mLST8	MTOR associated protein, LST8 homolog
MT-CO1/2/3	mitochondrially encoded cytochrome c oxidase subunit I/II/III
MTF1	metal regulatory transcription factor 1
mTOR; mTORC1/2	Mechanistic target of rapamycin kinase; mTOR complex 1/2
MYC	MYC proto-oncogene, bHLH transcription factor
NDUFA4	NDUFA4 mitochondrial complex associated
NDUFB11	NADH:ubiquinone oxidoreductase subunit B11
NGFR	Nerve growth factor receptor
Npas3	Neuronal PAS domain protein 3
Nrep	Neuronal regeneration related protein
NR2F6	Nuclear receptor subfamily 2 group F member 6
OFR356	Olfactory receptor family 7 subfamily C member 70
Olfr62/Or13p10	Olfactory receptor family 13 subfamily P member 10 (*Mus musculus*)
Olfr746/Or11h7	Olfactory receptor family 11 subfamily H member 7 (*Mus musculus*)
PAM	Peptidylglycine alpha-amidating monooxygenase
Pcdhb7	protocadherin beta 7
PDHA1	Pyruvate dehydrogenase E1 subunit alpha 1
PDHB	Pyruvate dehydrogenase E1 subunit beta
Pcp2/4	Purkinje cell protein 2/4
Picb1	Phospholipase C, beta 1
PI3K	Phosphoinositide-3-kinase
PIK3R1	Phosphoinositide-3-kinase regulatory subunit 1
Pmvk	Phosphomevalonate kinase

POLG	DNA polymerase gamma, catalytic subunit
POLG2	DNA polymerase gamma 2, accessory subunit
POLRMT	RNA polymerase mitochondrial
POM121	POM121 transmembrane nucleoporin
PPARG	Peroxisome proliferator activated receptor gamma
PPARGC1A	PPARG coactivator 1 alpha
PPP1R13B/Ppp1r17	Protein phosphatase 1 regulatory subunit 13B/17
PRKCG	Protein kinase C gamma
Prss47	Serine protease 47
Pvalb	Parvalbumin
MAX	MYC associated factor X
Napepld	N-acyl phosphatidylethanolamine phospholipase D
NDRG1	N-myc downstream regulated 1
NDRG2	NDRG family member 2
NFE2L2	NFE2 like bZIP transcription factor 2
NRF1	Nuclear respiratory factor 1
NUP	Nucleoporin (NUP 54, NUP85, NUP93, NUP160, NUP188)
NUP98	nucleoporin 98 and 96 precursor
PSEN1/2	Presenilin 1/2
PSG19	Pregnancy specific beta-1-glycoprotein 19 (*Mus musculus*)
Raf	Family of protein kinases
RAPTOR/RPTOR	Regulatory associated protein of MTOR complex 1
RARG	Retinoic acid receptor gamma
Ras	Family of small GTPases
RASGRP1	RAS guanyl releasing protein 1

RBM15B	RNA binding motif protein 15B
REPIN1	Replication initiator 1
Rheb	Ras homolog, mTORC1 binding
RhoA	Ras homolog family member A
RICTOR	RPTOR independent companion of MTOR complex 2
RPS17	Ribosomal protein S17
RPS6	Ribosomal protein S6
RPS6KA6	Ribosomal protein S6 kinase A6 (a p90-S6K)
RRAGC	Ras related GTP binding C
RSKR	RPS6 kinase related
RSK/S6K	RPS6 kinase family with two subfamilies (p70-S6K and p90-S6K)
RTN1	Reticulon 1
RUNX1	RUNX family transcription factor 1
S6K1	RPS6 kinase 1 (p70-S6K), encoded by *RPS6KB1*
S6K2	RPS6 kinase 2 (p70-S6Kβ), encoded by *RPS6KB2*
SCO1/2	Synthesis of cytochrome C oxidase 1/2
SDHA	Succinate dehydrogenase complex flavoprotein subunit A
Sgpp2	Sphingosine-1-phosphate phosphatase 2
SLC25A3	Solute carrier family 25 member 3 (mitochondrial phosphate carrier)
Slc25a47	Solute carrier family 25 member 47 (mitochondrial transporter thought to uncouple mitochondrial respiration from ATP synthesis)
SLC3A2	Solute carrier family 3 member 2 (L-type amino acid transporter)
SLC7A5	Solute carrier family 7 member 5 (L-type amino acid transporter)
Slc17a7	Solute carrier family 17 member 7 (sodium-dependent phosphate transporter; glutamate transport)
Slc1a6	Solute carrier family 1 member 6 (aspartate/glutamate transporter)

Slc4a4	Solute carrier family 4 member 4 (sodium bicarbonate cotransporter)
SNCA	synuclein alpha
SOD1/3	Superoxide dismutase 1/3
SORBS2/3	Sorbin and SH3 domain containing 2/3
SP1	Sp1 transcription factor
SRF	Serum response factor
SRGAP1	SLIT-ROBO Rho GTPase activating protein 1
SSBP1	Single stranded DNA binding protein 1
STAT1	Signal transducer and activator of transcription 1
STIM1	Stromal interaction molecule 1
SURF1	SURF1 cytochrome c oxidase assembly factor
TBP	TATA-box binding protein
Tenm1	Teneurin transmembrane protein 1
TFAM	Transcription factor A, mitochondrial
TGF-β	Transforming growth factor beta
Tha1	Threonine aldolase 1 (*Mus musculus*)
THOR	4E-binding protein (*Drosophila melanogaster*)
TP53Bp2	Tumor protein p53 binding protein 2
TSC1/2	Tuberous sclerosis protein complex subunit 1/2
TWNK	Twinkle mtDNA helicase
ULK1/2	unc-51 like autophagy activating kinase 1
UQCRC2	Ubiquinol-cytochrome c reductase core protein 2
UVRAG	UV radiation resistance associated
Vcam1	Vascular cell adhesion molecule 1
VGF	VGF nerve growth factor inducible

YY1	YY1 transcription factor

Chapter 1. General Introduction

1.1 Conceptual background and the goals of this thesis

Neuroscience as a discipline aims to understand one of the most complex biological systems in existence. In our efforts toward this lofty goal, genetic approaches comprise a crucial toolkit for delineating the molecular mechanisms governing healthy and diseased brain development and function. Historically, the identification and study of disease-causative mutations has facilitated novel insights into the basic biology of proteins fundamental to the brain and their role in the etiology of neurological disease processes. For example, the amyloid hypothesis of Alzheimer's disease was initially proposed following the discovery of pathogenetic mutations in *APP* and subsequent identification of *PSEN1* and *PSEN2* as genes linked to familiar Alzheimer's disease (Liu et al., 2019; Andrade-Guerrero et al., 2023). The association of *SNCA* (α-synuclein) with early-onset Parkinson's disease established a fundamental disease mechanism in Parkinson's and other synucleinopathies (Calabresi et al., 2023). Similarly, the study of genes causative of fragile X syndrome (*FMRP*; Richter and Zhao, 2021), Huntington disease (*HTT*; Nopoulos, 2016), and amyotrophic lateral sclerosis and/or frontotemporal dementia (*SOD1* and *C9orf72*; Smeyers et al., 2021; Akçimen et al., 2023) demonstrated the crucial role of these proteins in the brain. Particularly when considered with additional genes identified by genome-wide association studies (GWAS) that are not pathogenic but increase disease risk, this non-exhaustive list demonstrates the power of genetics to uncover fundamental biology relevant to human health. Collectively, investigation of these genes has uncovered shared pathological mechanisms such as disrupted proteostasis and energy metabolism which span multiple neurodegenerative diseases (Wilson et al., 2023).

Beyond these paradigmatic examples, "rare" genetic diseases (defined in the United States by a prevalence of less than 200,0000) are of particular interest for neuroscientists, as they disproportionately affect the nervous system early in development (Lee et al., 2020). Analysis of

disease descriptors in the Online Mendelian Inheritance in Man resource, OMIM (https://www.omim.org/statistics/geneMap), revealed that 83% of rare diseases occur in childhood (including pediatric, congenital, and neonatal diseases), and nearly 90% of these impact the nervous system (Lee et al., 2020). In total, almost 70% of rare diseases affect the nervous system (Lee et al., 2020).

In this dissertation, I present evidence that investigating mutations causing rare genetic diseases affecting copper homeostasis opens a window to understanding how copper-dependent mechanisms and metabolism interact to drive brain development. In the following sections, I will introduce this idea by briefly describing copper homeostasis mechanisms and functions in mammalian cells, identifying key roles for copper in the brain and during neurodevelopment, and contextualizing these results with clinical and pre-clinical findings in several diseases of copper deficiency.

1.2 Copper biology

The role of copper in biology is evolutionarily ancient and is tightly linked to oxygen levels, becoming more prominent in response to increases in atmospheric and oceanic oxygen derived from photosynthesis (Festa and Thiele, 2011). Copper is a redox active metal, and its chemical properties (in particular, its ability to exist as Cu^{1+} or Cu^{2+} under physiological conditions) facilitate a wide range of biochemical interactions and functions, both directly and indirectly (reviewed in Festa and Thiele, 2011; Tsang et al., 2021; Lutsenko et al., 2024).

1.2.1 Copper functions

Copper is perhaps best known for its role as a required constitutive cofactor for enzymes involved in energy and redox metabolism (CCO and SOD1/3, respectively); activity of cytochrome *c* oxidase (CCO, the final enzyme of the electron transport chain) and the superoxide dismutases SOD1 and SOD3 is copper-dependent (Culotta et al., 2006; Horn and Barrientos, 2008). Copper also functions as a cofactor in biosynthesis and is required for the activity of dopamine β-

hydroxylase (DBH; converts dopamine to norepinephrine), peptidyl glycine a-hydroxylating monooxygenase (PAM; modifies neuroendocrine peptide precursors such as corticotropin-releasing hormone and vasopressin), and lysyl oxidase (LOX; crosslinks collagen and elastin to maintain tissue structure) (Lutsenko et al., 2024).

More recently, two novel roles for copper have been identified: cuproptosis and copper allostery. “Cuproptosis” is a copper-dependent mechanism of regulated cell death distinct from apoptosis, ferroptosis, or necroptosis. In cuproptosis, accumulation of copper in the mitochondria induces proteotoxic stress due to aggregation of lipoylated proteins involved in respiration (Cobine and Brady, 2022; Tsvetkov et al., 2022). Copper allosteric regulation of cell signaling and transcription has been reported for many signaling pathways. Copper is required for kinase activity of ULK1/2 (Tsang et al., 2020) and MEK1/2 (Brady et al., 2014; Grasso et al., 2021), which are involved in autophagy and MAPK signaling, respectively. The transcription factor HIF-1 exhibits selective copper-dependent regulation of gene expression resulting from changes in its binding of critical motifs in HIF-1α regulatory elements (Zhang et al., 2014; Wu et al., 2019). Copper similarly affects activity and binding by the transcription factors MTF1 and SP1 (Song et al., 2008; Tavera-Montañez et al., 2019; Li et al., 2023). Copper is also known to modulate neurotransmission by AMPA and NMDA receptors (reviewed by Gale and Aizenman (2024) and described in more detail in section 1.2.3). The recently coined terms “metalloallostery” to describe metal-dependent regulation of protein activity by binding at allosteric sites rather than active sites (Pham and Chang, 2023) and “cuproptosis” (Tsvetkov et al., 2022) are a testament to our rapidly evolving understanding of the vast influence of copper and other metals in biology.

1.2.2 Systemic and cellular copper homeostasis

Copper in circulation exists as copper(II) and is mainly bound by ceruloplasmin, with small amounts detected in albumin and other small proteins or complexes (Cabrera et al., 2008; Linder, 2016; Kirsipuu et al., 2020). In contrast to more abundant redox-inactive metals like calcium and

sodium, whose free ion concentrations undergo dramatic changes during signaling, redox-active metals like copper must be tightly regulated and bound by chaperones or other molecules to avoid the production of free radicals (Tsang et al., 2020). This dichotomy is clearly represented by the comparative levels of labile copper (10^{-18} M) (Rae et al., 1999; Morgan et al., 2019) as compared to the concentration of calcium (~10^{-7} M) (McNaughton et al., 1986; Maravall et al., 2000; Bagur and Hajnóczky, 2017) or sodium (~10 mM) (Lijnen et al., 1984; Tashiro et al., 2005; Lambert et al., 2015) (see Bionumber ID 107486; Milo et al., 2010; Martin, 2006). Thus, there exists an extensive family of copper transporters and chaperones to sequester and localize copper in the cell and across tissues.

Three key transporters regulate intracellular copper levels and copper levels throughout the body (reviewed in Festa and Thiele, 2011; Tsang et al., 2021; Lutsenko et al., 2024). CTR1 (copper transporter 1, encoded by *SLC31A1*) resides in the cell membrane and is the primary protein mediating uptake of copper into the cell. ATP7A and ATP7B (copper-transporting ATPases 1 and 2, respectively) translocate between the Golgi and the plasma membrane; they use ATP hydrolysis to transport copper into the Golgi or (under conditions of increased intracellular copper) extrude copper from the cell. Differential expression of these three transporters on the basolateral and apical membranes of polarized cells enables copper transport through tissues such as the blood brain barrier, intestinal epithelium, and the canalicular membrane in the liver (Polishchuk et al., 2014; Pierson et al., 2019; Roy and Lutsenko, 2024). Before circulating copper(II) can be imported and used by the cell, it is reduced to copper(I) principally by Steap reductases, although it has been proposed that this reductive step can be facilitated by CTR1 itself (Ohgami et al., 2006; Galler et al., 2020). Recent studies provide evidence that DMT1 (divalent metal transporter 1) can facilitate copper uptake in vitro in the absence of CTR1, perhaps even as copper(II) (Lin et al., 2015; Pezacki et al., 2022), but its role in copper biology remains poorly understood. Once copper reaches the cytosol, copper-binding

proteins like metallothioneins and glutathione regulate the labile (biologically available) pool of intracellular copper, preventing toxicity by buffering and storing copper within the cell.

While less is known about intracellular copper transport, many other transporters and chaperones have been identified that are involved in regulation of copper transport, buffering, and storage, often with specific proteins dedicated to copper delivery to and utilization by particular cellular compartments (reviewed in Festa and Thiele, 2011; Maung et al., 2021; Tsang et al., 2021; Lutsenko et al., 2024). Within the cytoplasm, CCS (copper chaperone for superoxide dismutase) delivers copper to SOD1. In the secretory pathway, ATOX1 (antioxidant 1 copper chaperone) delivers copper to ATP7A/B, which are responsible for copper transport into the Golgi for metalation of enzymes like DBH and SOD3 (reviewed in Festa and Thiele, 2011; Tsang et al., 2021; Lutsenko et al., 2024). Within the mitochondria, the outer mitochondrial membrane is permeable to copper and other ions (Kühlbrandt, 2015). After passing the outer membrane, copper is delivered to SLC25A3 (localized to the inner mitochondrial membrane), which is primarily responsible for copper transport into the matrix (Boulet et al., 2018; Cobine et al., 2021; McCann et al., 2022). Mitochondrial copper is then either used by SOD1 or by the complex IV assembly factor and metallochaperone COX17, which coordinates with other complex IV assembly factors such as COX11, COX19, COA4/6, and SCO1/2 to promote the assembly of cytochrome c oxidase (reviewed in Horn and Barrientos, 2008; Garza et al., 2022b). These complex IV assembly factors reside in the intermembranous space of the mitochondria, and the mechanism of copper delivery to these factors remains unclear. Comparatively less is known about the mechanisms for copper import and export into/from other organelles and structures such as the nucleus, lysosomes, or vesicles (Maung et al., 2021; Lutsenko et al., 2024).

1.2.3 Copper in the nervous system

Many of the pan-cellular roles for copper discussed above are relevant to the nervous system. In particular, copper is required for mitochondrial respiration and is a key nutrient for

tissues like the brain with high energy demands, metabolic activity, and oxygen consumption (Scheiber et al., 2014; discussed further in section 1.2.4). In addition, copper has several neural-specific functions within the brain (Telianidis et al., 2013). As described previously, copper entry to the brain is mediated by CTR1, ATP7A, and ATP7B, and the activity of important brain enzymes such as DBH and PAM is dependent on their metalation in the Golgi (Lutsenko et al., 2024). Recent studies have also linked copper to neurotransmission. In hippocampal neurons, NMDA receptor activation induces reversible trafficking of ATP7A to neuronal processes, where it releases copper extracellularly through an unknown mechanism that is proposed to prevent excitotoxicity by regulating NMDA activity in a copper-*independent* manner (Schlief et al., 2005; Schlief et al., 2006; You et al., 2012). Copper-*dependent* enhancement of AMPAergic and GABAergic neurotransmission in rat hippocampal primary cultures has also been observed, which causes the accumulation of AMPA receptors at the plasma membrane and an increase in PSD95 (Colledge et al., 2003; Peters et al., 2011). In primary cultured rat hippocampal neurons, copper colocalizes with F-actin in dendritic spines (Domart et al., 2020); notably, both copper chelation and supplementation impacted dendritic actin dynamics (Perrin et al., 2017). This non-comprehensive set of examples supports the crucial role of copper to the brain and illustrates why disruption to copper homeostasis is linked to a number of neurodegenerative diseases (discussed further in section 1.3).

Relative to other organs and fluids in the body, the brain and cerebrospinal fluid (CSF) is enriched in copper. The brain has the second highest copper concentration among organs in the body (5.2 μg/g), and CSF has the highest copper levels of all internal milieu fluids (5 μg/g), which is approximately 5-fold the amount in plasma (Linder, 1991; Linder and Hazegh-Azam, 1996). Copper half-life is dramatically longer in the brain (457 days) as compared to plasma, liver, muscle, or kidney, in which copper half-life ranges between several days to several months (Levenson and Janghorbani, 1994). The steady-state copper landscape within the brain differs both spatially and temporally, exemplified by the following studies in adult rat brains. Copper is

enriched in the choroid plexus and is present at lower levels in the globus pallidus as compared to the striatum, cingulate cortex, and ventral hippocampus (Ashraf et al., 2019). Silver-staining optimized for metal detection revealed differential copper localization within the locus coeruleus and cerebellum, with copper detected primarily in the neuropil at pre-synapses in the locus coeruleus and to the mitochondria in the granular layer of the cerebellum (Sato et al., 1994). Copper levels increase with age in the subventricular zone, choroid plexus, cortex, corpus striatum, hippocampus, midbrain and medulla, and cerebellum, with the highest overall levels in the midbrain and medulla (Palm et al., 1990; Fu et al., 2015). These results were partially reproduced in a comprehensive study of the mouse brain between 3 to 18 months of age in which copper levels were unaltered in the cortex and hippocampus with age but increased in the striatum, cerebellum, and midbrain (Suryana et al., 2024). In humans, multiple studies have reported elevation of copper in the substantia nigra (Loeffler et al., 1996; Popescu et al., 2009; Davies et al., 2013) as well as the cerebellum (Davies et al., 2013). ATP7A/B and CTR1 were detected in humans by immunoblot and immunohistochemistry in all brain regions studied with cell type-specific patterning; for example, ATP7A/B were highly expressed in Purkinje neurons but not Bergmann glia (Davies et al., 2013). This elevated expression of ATP7A in Purkinje neurons was also observed in mouse and was notable in that it remained elevated with age, while ATP7A expression decreased in most other brain regions (Niciu et al., 2006).

Less is known about the role for copper in non-neuronal cells, but ATP7A protein expression has been detected in astrocytes, microglia, oligodendrocytes, and endothelial cells in the mouse brain (Niciu et al., 2006). Copper uptake has been shown in vitro in both astrocytes and microglia (Scheiber et al., 2010; Zheng et al., 2010). Microglia activated by interferon-gamma increase expression of ATP7A and CTR1, which is associated with increased copper uptake and trafficking of ATP7A to vesicles (Zheng et al., 2010). Astrocytes are proposed to be particularly important for transporting copper across the blood brain barrier; astrocytes in the subventricular zone are enriched in copper, which is distributed in copper storage vesicles that increase with

age (Pushkar et al., 2013; reviewed in Ellison et al., 2022). Primary cultured astrocytes have half the amount of copper found in primary cultured neurons (Hare et al., 2013).

While an active area of investigation with much to be discovered, it is clear that copper levels and expression of copper chaperones, copper transporters, and cuproenzymes exhibit regional, cellular, subcellular, and age-sensitive differences in rodents and humans (reviewed in Telianidis et al., 2013; Scheiber et al., 2014; Ellison et al., 2022; Lutsenko et al., 2024).

1.2.4 Copper and metabolism during neurodevelopment

The brain is particularly vulnerable to copper toxicity as well as copper deficiency (Scheiber et al., 2014), and neurodevelopment is a particularly vulnerable time for copper insults due to 1) the high energy consumption and transitions in metabolism by the brain during this period (Bülow et al., 2022) and 2) the increased neuronal demand for copper after differentiation (Hatori et al., 2016; Chakraborty et al., 2022). While the fetal brain produces energy primarily by glycolysis, after birth there is a shift toward a reliance on mitochondrial respiration, with brain consumption of glucose and oxygen in humans peaking at age 5 at almost double the amount consumed by the adult brain (Goyal et al., 2014; Kuzawa et al., 2014; Steiner, 2020; Oyarzábal et al., 2021). This transition from glycolysis to oxidative phosphorylation is in part cell autonomous, as it is also observed in differentiating neurons and muscle cells in culture (Vest et al., 2018; Iwata et al., 2023; Casimir et al., 2024; Rajan and Fame, 2024), and is necessary for neurodevelopment (Zheng et al., 2016; Sakai et al., 2023; Casimir et al., 2024; Iwata and Vanderhaeghen, 2024). In fact, aberrant hyperglycolytic metabolism in neurons induces dysfunction and damage in vitro and in vivo (Jimenez-Blasco et al., 2024). As copper is required for mitochondrial respiration, these studies demonstrate the tight association between regulation of copper and metabolism in neuronal cells.

Accordingly, neurodevelopment has stringent requirements for copper levels and localization within organelles and across tissues and organs, and the expression of copper

transporters, chaperones, and copper-dependent enzymes is tightly regulated temporally and spatially. For example, Hatori et al. (2016) and Chakraborty et al. (2022) reported an increased demand for copper after neuronal differentiation in vitro. As compared to undifferentiated neuroblastoma cells, differentiated SH-SY5Y cells upregulate ATOX1 and ATP7A (but not ATP7B) and increase gene expression of COX17, COX1, and CTR1; accordingly, there is an increase in copper levels in whole cell lysates as well as in the fraction containing the trans-Golgi network. This is consistent with the increased production of enzymes like DBH that are loaded with copper as they travel through the secretory pathway (Hatori et al., 2016). Similarly, differentiated PC-12 cells increase CTR1 expression and copper levels in whole cells and in post mitochondrial fractions (containing the trans-Golgi network). In addition, these neurons exhibited increased expression of SLC25A3 and COX17, consistent with the observations of increased copper levels in the mitochondria (Chakraborty et al., 2022). In contrast, differentiation causes C-6 cells (a glia cell line) to *decrease* total cellular copper, and no changes in expression of any of the aforementioned copper transporters and chaperones were observed. Differential subcellular localization of ATP7A in neurons and glia suggests that copper plays a key role in neuronal but not glia differentiation through the secretory pathway, while glia sequester copper into endosomes during differentiation (Chakraborty et al., 2022).

Similar regulation of copper and related proteins is observed in vivo. For example, the copper transporter ATP7A exhibits age-dependent changes in expression in early development in the neocortex, cerebellum, hippocampus, and olfactory bulb (Niciu et al., 2006; El Meskini et al., 2007) and traffics to neuronal processes prior to synaptogenesis (El Meskini et al., 2005; Niciu et al., 2006). The crucial role for copper in neurodevelopment is underscored by the impact of disruption to these pathways. Defects in copper homeostasis are linked to dysfunctional neuronal differentiation, organization, migration, and arborization; axonal outgrowth; synaptogenesis; and neurotransmission in multiple brain regions (Purpura et al., 1976; Hirano et

al., 1977; Büchler et al., 2003; Niciu et al., 2006; El Meskini et al., 2007; Scheiber et al., 2014; Zlatic et al., 2015).

1.3 Neurological and neurodegenerative diseases of copper dyshomeostasis

Copper dyshomeostasis (or disruption to copper homeostasis) is causative of or associated with a variety of neurodevelopmental and neurodegenerative diseases. These can arise when environmental exposure alters copper levels, mutations impair the function of copper transporters or chaperones, and/or processes upstream or downstream of copper are disturbed (Waggoner et al., 1999; Opazo et al., 2014b). Of these disorders, genetic diseases of copper metabolism provide an opportunity to study the confluence of homeostatic mechanisms regulating copper and metabolism that interact to drive brain development.

Here, I will focus on describing a set of rare childhood diseases of copper deficiency caused by mutations in the copper transporters *ATP7A* and *SLC31A1* (CTR1), followed by a brief summary of the role of copper deficiency in more prevalent diseases.

1.3.1 ATP7A*-related diseases*

Mutations that mislocalize, reduce, or abolish expression of the copper transporter ATP7A or interfere with its copper transport activity cause one of three sex-linked diseases, all of which present with prominent neurological symptoms (Kaler, 2011). The most severe condition is Menkes disease (OMIM: 309400), which classically presents at 1-3 months of age with seizures and growth defects (Menkes et al., 1962; Tümer and Møller, 2010; Kaler, 2011) and has a prevalence as high as 1 per 8664 live male births (Kaler et al., 2020). Occipital horn syndrome (OHS; OMIM: 304150) is associated with similar but milder symptoms that appear in early to middle childhood, while *ATP7A*-related distal motor neuropathy (DMN; OMIM: 300489) is typically diagnosed in early adulthood (Kaler, 2011). The type and severity of the *ATP7A* mutation determines the onset and range of symptoms of the disease (Kaler, 2011; Skjørringe et al., 2017),

and complete loss of ATP7A function is embryonic lethal in mice (Lenartowicz et al., 2015). For the remainder of this section, I will focus on Menkes disease.

ATP7A is widely expressed in many different tissues, and copper homeostasis is disrupted throughout the body in Menkes, and the inability to absorb and release dietary copper into the bloodstream ultimately renders the brain and many other organs copper-deficient (Tümer and Møller, 2010). Characteristic disease phenotypes can be attributed to insufficient activity of particular copper enzymes, such as hair and skin hypopigmentation (tyrosinase), connective tissue abnormalities (lysyl and amino oxidases), and anemia (ceruloplasmin and hephaestin). While certain key brain enzymes play a role in brain pathology in Menkes disease (notably cytochrome C oxidase, superoxide dismutase, DBH, and PAM), the mechanism(s) by which copper deficiency in the brain produces progressive neurodegeneration, epileptic encepha-lopathy, and early death in infants remain unknown (Tümer and Møller, 2010; Kaler, 2011; Comstra and Faundez, 2017). Notably, Purkinje neurons are particularly impacted in Menkes disease and experience rapid and specific pathology relative to other cell types and regions of the brain in both humans (Ghatak et al., 1972; Vagn-Hansen et al., 1973; Purpura et al., 1976; Hirano et al., 1977; Troost et al., 1982; Kodama et al., 2012) and mouse models (Yamano and Suzuki, 1985; Niciu et al., 2007; Lenartowicz et al., 2015; Guthrie et al., 2020).

Early diagnosis and administration of copper histidine or other copper compounds systemically or intracerebrally is the only available treatment for Menkes disease, though experimental gene therapy is underway and the FDA-approved drug elesclomol (a cell-permeant compound which delivers copper(II) preferentially to the mitochondria; Zheng et al. (2022)) shows promise in mouse models of Menkes (Donsante et al., 2011; Blackman et al., 2012; Nagai et al., 2012; Ogawa and Kodama, 2012; Guthrie et al., 2020). For any therapeutic benefits, patients must have some residual ATP7A copper transport activity; regardless, no treatment fully rescues patients with the disease (Kaler, 2011).

Notably, symptoms do not arise immediately after birth in Menkes disease or in mouse models. For example, most mouse models of Menkes disease and severe brain copper deficiency have been reported to exhibit substantial neurodegeneration by postnatal day 10 (P10) to P14, and these mice typically die between 2-3 weeks of age (Donsante et al., 2011; Lenartowicz et al., 2015; Guthrie et al., 2020; Yuan et al., 2022). Neuronal cell death is not yet observed in macular or mottled brindled mice at P7 (Yajima and Suzuki, 1979; Iwase et al., 1996). Similarly, neurological symptoms are not apparent at birth in humans with Menkes disease and develop in early infancy (Kaler, 2011; Fujisawa et al., 2022). The delay in Menkes disease onset after birth determines the window when copper supplementation therapy can be effective in mice and humans (reviewed in Kaler, 2011; Lenartowicz et al., 2015). In patients with copper-responsive mutations, copper-histidine administration improves neurological symptoms only if therapy is initiated before 1 month of age (Sarkar et al., 1993; Kaler et al., 2008). Similarly, the therapeutic benefits of this treatment in mice when delivered during the first postnatal week are lost if administration is delayed until P12 (Fujii et al., 1990), and early treatment starting at P7 with the copper compound elesclomol rescues mouse models of Menkes (Guthrie et al., 2020; Yuan et al., 2022).

This critical therapeutic window for copper delivery suggests the existence of a development-sensitive mechanism of resilience to copper deficiency that could delay neurological phenotypes and may be causally linked to concurrent changes in brain metabolism early in life. In addition to the nature of the *ATP7A* genetic defect, increasing neurodevelopmental demands for copper and/or neurodevelopment-sensitive mechanisms conferring resilience to copper deficiency may contribute to differences in disease severity and onset of *ATP7A*-related diseases.

1.3.2 SLC31A1*-related diseases*

SLC31A1 genetic defects (OMIM: 620306) cause neurological symptoms similar to Menkes disease, including neurodegeneration, seizures, and vascular tortuosity of brain arteries

(Batzios et al., 2022; Dame et al., 2022). *ATP7A* and *SLC31A1* mutations do not produce identical diseases; for example, the characteristic kinky, coarse hair for which Menkes disease was originally named was not observed in patients with CTR1 deficiency (Dame et al., 2022), perhaps because these patients retain functional ATP7A which is able to deliver copper to tyrosinase through the secretory pathway (Setty et al., 2008).

Batzios et al. (2022) describe a patient that died at 1 month of age, suggesting that some *SLC31A1* mutations may cause a disease with earlier onset and with more severe brain atrophy than mutations in *ATP7A*. This has been proposed to be the result of impaired fetal copper uptake due to CTR1 deficiency (Dame et al., 2022). This is consistent with the embryonic lethality observed in mouse models with complete loss of CTR1 (Lee et al., 2001). However, like Menkes disease, particular *SLC31A1* mutations will likely cause diseases of differing severity and onset depending on the amount of transporter activity remaining. The two patients identified by Dame et al. (2022) were both alive at 3 years of age and did not develop neurological symptoms until 2-3 months of age.

These first reports of a disease associated with *SLC31A1* mutations were both published in 2022, and as such there remains much to be discovered. The diseases reviewed here caused by mutations in *ATP7A* and *SLC31A1* demonstrate the importance of the developmental regulation of copper for health brain development. The comparative study of CTR1 and ATP7A deficiency may enable the differentiation of disease mechanisms caused by loss of each protein specifically from those caused by overall copper deficiency. For example, neural- and glial-specific KO of ATP7A in mouse increases the propensity for NMDA-induced seizures and produces sensorimotor deficits in the absence of copper deficiency but does not reproduce the severe neurological phenotypes observed following global KO of ATP7A (Hodgkinson et al., 2015). This is further evidence that cell-autonomous requirements for ATP7A and CTR1 within the brain must be considered within the context of copper deficiency.

1.3.3 ATP7B-*related diseases*

Wilson's disease (OMIM: 277900, reviewed in Członkowska et al. (2018)) is caused by autosomal recessive mutations in *ATP7B* that induce copper toxicity throughout the body. The disease has a variety of clinical presentations in patients, perhaps due to the nature of the genetic defects impacting ATP7B function and/or interaction with other genetic risk factors (Lutsenko et al., 2024). As discussed above (section 1.2.2), ATP7B regulates copper efflux at the plasma membrane and delivery of copper to the Golgi. ATP7B is the primary efflux copper transporter for the liver and is also involved in regulating copper levels in the brain (see section 1.2.3). Accordingly, most patients experience progressive liver disease (which can ultimately lead to liver failure if not treated), and a subset of patients present with neurological and psychiatric symptoms, including parkinsonism, mood disorders, and deficits in executive function, which can progress to neurodegeneration (Litwin et al., 2017; Dusek et al., 2019; Viveiros et al., 2021; Antos et al., 2023). The neuropathology associated with these neurological symptoms is not well defined, and whether it is caused by cuproptosis remains to be explored (Tsvetkov et al., 2022).

1.3.4 Alzheimer's disease, Parkinson's disease, amyotrophic lateral sclerosis, and schizophrenia

Copper dyshomeostasis is also associated with more prevalent neurodegenerative diseases (Scheiber et al., 2014). Both Parkinson's disease (PD) and amyotrophic lateral sclerosis (ALS) are genetically linked to copper homeostasis. Regional deficits in the copper intake transporter CTR1 and copper levels are observed in the substantia nigra and locus coeruleus of PD brains (Davies et al., 2014), and neuromelanin-expressing neurons of PD patients had lower copper levels than controls (Carmona et al., 2024). Mutations in genes responsible for ATP7A trafficking are associated with some cases of PD, and individuals with Wilson's disease (which arises due to defects in the copper transporter ATP7B) frequently exhibit parkinsonism (Członkowska et al., 2018; Zlatic et al., 2018). Overexpression of the copper-dependent enzyme

tyrosinase in the rat substantia nigra causes PD-like motor and degenerative phenotypes (Carballo-Carbajal et al., 2019). An estimated 10-15% of cases of familial ALS are associated with the copper/zinc superoxide dismutase SOD1 (Rosen et al., 1993; Pramatarova et al., 1995; Tokuda and Furukawa, 2016). Alzheimer's disease (AD) is associated with brain-specific copper depletion, which may influence amyloid processing (Schrag et al., 2011; Roberts et al., 2012; Rembach et al., 2013).

Copper is also linked to schizophrenia, a developmental rather than degenerative neurological disorder. Deficiency of dysbindin-1, genetically linked to schizophrenia (Fatjó-Vilas et al., 2011; Wang et al., 2017), has been reported to modify copper homeostasis through changes in expression of ATP7A, ATP7B, CTR1, and ATOX1 and altered copper-dependent trafficking of ATP7A to the cell surface (Gokhale et al., 2015). In humans, CTR1 expression was significantly altered in the entorhinal cortex and molecular layer of the dentate gyrus of the hippocampus of patients with schizophrenia as compared to controls, and the substantia nigra has been reported to exhibit reduced dysbindin-1, CTR1, and total copper in patients with schizophrenia (Schoonover et al., 2020; Schoonover et al., 2021).

These diseases reveal the fundamental roles of copper in neurodevelopment and maintaining central and peripheral nervous system functions and health.

1.4 Significance of this dissertation research and overview of findings

Determining how copper-dependent processes intersect with and impact the molecular pathways that regulate metabolism and affect neuronal function will improve current models of Menkes disease and CTR1 deficiency. It is unknown to what degree copper deficiency modulates signal transduction and metabolism in neuronal cells, as well as how these signaling mechanisms are influenced by the *extent* of copper deficiency and/or *subcellular distribution* of copper across different compartments. The answer to these questions will distinguish generalized copper deficiency phenotypes from disease-specific pathology and may identify related resilience

mechanisms. For example, it remains unclear why patients with Menkes disease do not exhibit symptoms at birth (see section 1.3.1). It is possible that the brain engages adaptive responses to copper deficiency that delay Menkes disease onset, which could be shared with or distinct from the milder and later onset occipital horn syndrome. Similarly, loss of ATP7A or CTR1 is likely to cause a set of shared responses due to insufficient copper regardless of the mutation, along with unique responses arising due to the particular functions of each protein.

This dissertation contributes to the body of knowledge aiming to answer these questions, testing the following **overall hypothesis:**

> Neurological phenotypes in genetic forms of copper deficiency are the result of an equilibrium between adaptive and maladaptive mechanisms.

In Chapter 2, I establish a protocol by which to quantify trace elements present in biological specimens with limited sample amounts using inductively coupled plasma mass spectrometry, a critical technique for the study of metals in biology. Chapter 3 describes results using 3 models of neuronal copper deficiency in a human cell line, *Drosophila*, and mouse. Several “omics” techniques are used to unbiasedly characterize signaling mechanisms engaged in copper-deficient neuroblastoma cells and the brain of a Menkes mouse model at a pre-symptomatic timepoint to uncover mechanisms engaged before cell death. Pharmacogenetic tools are used in cells and *Drosophila* to determine whether particular copper deficiency-induced mechanisms are adaptive or deleterious.

1.4.1 Model Systems Utilized in this Dissertation

As discussed in section 1.2, ATP7A sequesters cytosolic copper into the Golgi and responds to elevated intracellular copper by moving to the cell membrane and extruding excess copper from the cell. In Menkes disease, the brain is copper deficient because loss-of-function ATP7A mutations prevent the absorption of dietary copper and its release into the bloodstream (Tümer and Møller, 2010; Kaler, 2011). A challenge of replicating this model in vitro is that the

same mutation (ATP7A-KO) would induce *excess* cellular copper by impairing copper extrusion. Thus, ATP7A mutations causative of Menkes are inappropriate models for studying copper deficiency in vitro.

To identify cell-autonomous mechanisms downstream of copper deficiency, applicable to both Menkes disease and CTR1 deficiency, I used 3 model systems (Figure 1):

1. **CTR1-KO SH-SY5Y human neuroblastoma cells**: *SLC31A1*-null cells lack the copper intake transporter CTR1, the main copper uptake transporter in mammals, preventing copper import.
2. **ATP7-OE in the epidermis or class IV sensory neurons in Drosophila**: Overexpression of ATP7 leads to copper extrusion from the cell and cell autonomous copper deficiency.
3. **Intestinal ATP7A-KO in mouse**: Loss of ATP7A from the intestines prevents absorption of dietary copper, phenocopying Menkes disease (Wang et al., 2012).

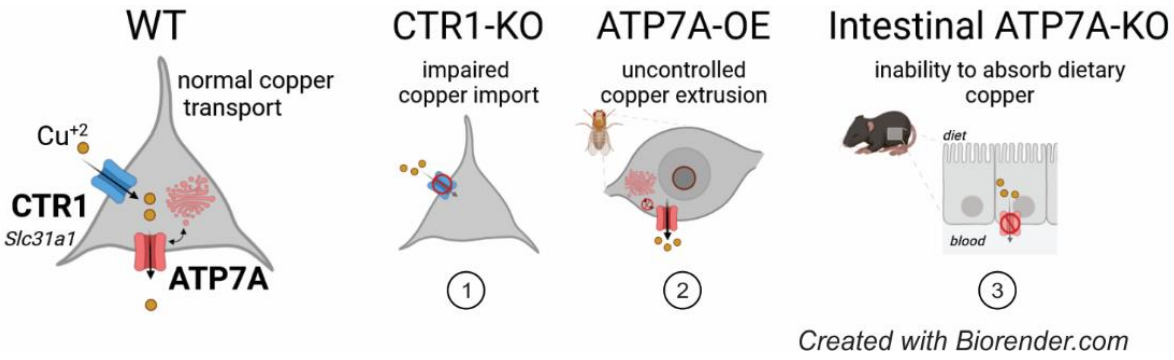

Figure 1. Model systems for copper deficiency.

Diagrams showing copper transport functions of ATP7A and CTR1 in wildtype (WT) and copper deficient mutants. **WT**: CTR1 is the primary copper uptake transporter in mammals. ATP7A translocates between the Golgi and the plasma membrane and extrudes excess copper from the cell. **Model 1**: CTR1-KO blocks copper import and causes copper deficiency in vitro. **Model 2**: Cell autonomous ATP7A-OE in neurons in *Drosophila* produces copper deficiency by inducing release of

copper from the cell. **Model 3**: ATP7A-KO in the intestines prevents absorption of copper from the diet, ultimately causing brain copper deficiency.

Using these three model systems, we discovered that CTR1 KO cells have defects in DBH and complex IV, the latter producing reduced ATP-dependent and basal respiration concurrent with increased glycolysis. These mitochondrial respiratory phenotypes were rescued by treatment with elesclomol, which preferentially delivers copper to the mitochondria (see section 3.3.1). This is consistent with previous reports of copper deficiency in other cell types (Zeng et al., 2007; Ghosh et al., 2014; Soma et al., 2018).

1.4.2 Overview of Findings

Copper deficiency-induced changes in signal transduction pathways increase protein synthesis in neuronal cells

While it is known that multiple kinases have copper-binding domains which regulate their activity (Brady et al., 2014; Tsang et al., 2020; Perea et al., 2023), to date very few proteomics and/or transcriptomic studies have been published to broadly characterize the impact of copper deficiency on signaling pathways. Most of these studies induced copper deficiency with copper chelators or copper-deficient media rather than a genetic approach, and no proteomics studies have been performed in copper-deficient neurons or neuronal-like cells (Hsieh et al., 2013; Kang et al., 2014; Voli et al., 2020; Schulten et al., 2022; Poursani et al., 2023).

We performed multiomics and confirmatory immunoblots to discover that mTOR signaling pathway activity was upregulated in CTR1 KO cells (see sections 3.3.2 and 3.3.3). The most dramatic change was a decrease in levels of DEPTOR, an mTOR inhibitor, at both the protein and RNA level. Among the other mTOR substrate proteins we identified, we observed increased phosphorylation of Ribosomal Protein S6 (RPS6) and increased expression and phosphorylation of p70-S6K. Concomitantly, we also identified decreased expression and phosphorylation of EIF2AK3 (PERK, eukaryotic translation initiation factor 2 alpha kinase 3) in CTR1 mutant cells.

The convergence of these changes in RPS6 and PERK represents the modification of two distinct pathways in CTR1 KO cells in a manner predicted to elicit increased protein synthesis, which we confirmed by puromycin incorporation and immunoblot (see section 3.3.5).

We hypothesized that increased activation of the mTOR signaling pathway and protein synthesis in copper deficient CTR1 KO cells represent an adaptive response to copper deficiency. To test this hypothesis, we measured cell survival when exposed to combinations of drugs that should promote (insulin) or inhibit/fail to stimulate mTOR pathway activity (Torin 2, rapamycin, low serum media), along with drugs to decrease (BCS) or increase copper levels (elesclomol) (see section 3.3.4). We also assessed cell respiration over several days under conditions which should inhibit mTOR activation (low serum media) or inhibit protein synthesis (treatment with emetine) (see section 3.3.5). CTR1 KO cell survival was more resistant to serum depletion and responded less to insulin as compared to wildtype cells, consistent with increased mTOR activity in these cells. In assays looking at synergistic drug effects, the pro-survival effects of serum were antagonized more strongly by mTOR inhibition in CTR1 KO cells, and there was no significant effect on drug synergy between mTOR inhibitors and either elesclomol or BCS. The IC50 for the protein synthesis inhibitor emetine was modestly decreased in CTR1 KO cells, and CTR1 KO cell respiration was resistant to both emetine and low serum as compared to wildtype cells. Together, this demonstrates that mTOR inhibition and protein synthesis inhibition are indeed more toxic to copper deficient cells, suggesting that increased protein synthesis is an adaptive response to copper deficiency.

Increased protein synthesis and mTOR activation is an adaptive response observed in neurons in vivo

Limited proteomics and transcriptomics studies have been performed to study the brain of mouse models of copper deficiency or humans with Menkes disease. There are no such studies performed in the mouse brain, and only one case study has been reported in human, which

quantified the transcriptome in bulk tissue from the brain (Liu et al., 2005). However, this post-mortem study only captured the molecular landscape of the brain after substantial pathology, providing little clarity as to mechanisms by which the brain responds to copper deficiency *before* cell death and neurodegeneration. In addition, studies of bulk tissue provide insights into broad changes within the brain but fail to identify cell-type specific responses to copper deficiency (see section 1.2.3). Thus, we sought to characterize the transcriptome in a mouse model of Menkes disease at a presymptomatic timepoint and in a cell-type specific manner, focusing on Purkinje neurons.

We first performed spatial transcriptomics of the cerebellum in copper deficient $Atp7a^{flx/Y}$ :: $Vil1^{Cre/+}$ mice (see section 3.3.6). At postnatal day 10 before the onset of neurodegeneration, copper deficient Purkinje neurons upregulate protein synthesis machinery transcripts involved in formation of ribosomal subunits and translation initiation. In addition, we observed increased abundance of insulin and phosphorylation of the insulin-like growth factor receptor 1 in bulb cerebellum in mutant mice. This evidence supports increased mTOR pathway activity and downstream protein synthesis in the brain of copper deficient mice at a timepoint before neuronal cell death.

To test whether protein synthesis is also adaptive in vivo, we moved to *Drosophila* as a more tractable genetic system to manipulate targets of interest. We combined ATP7 overexpression to induce copper deficiency in either the thoracic epidermis or class IV sensory neurons with a swath of genetic manipulations of the mTOR pathway. In the epidermis, wounds caused by ATP7-OE were exacerbated by RNAi-mediated loss of mTOR pathway genes *S6k*, *raptor*, or *Akt*. In turn, overexpression of *S6k* or *Thor* RNAi (both manipulations which promote protein synthesis downstream of mTOR) partially rescued dendritic phenotypes caused by ATP7A-OE in class IV sensory neurons. These results demonstrate that stimulation of protein synthesis partially reverts neuronal phenotypes in copper deficient neurons.

1.4.3 Summary

Based on our pharmacogenomics in cells and Drosophila genetics, we conclude that mTOR activation and upregulation of protein synthesis is an adaptive mechanism engaged in response to copper deficiency. Our results show a novel convergence of two mechanisms modulating protein synthesis machinery that increase cellular resilience to genetic defects causing neurodevelopmental and neurodegenerative phenotypes. Beyond the relevance of these studies for childhood neurodevelopmental disorders caused by mutations in *ATP7A* or *SLC31A1*, we believe these results inform our understanding of the neuropathology of more common diseases known to be associated with metals (see section 1.3) and clarify the role of metabolic transitions during neurodevelopment and in certain disease conditions (see section 1.2.4).

Chapter 2. Sulfur- and phosphorus-standardized metal quantification of biological specimens using inductively coupled plasma mass spectrometry

Alicia R Lane[1], Avanti Gokhale[1], Erica Werner[1], Anne Roberts[2], Amanda Freeman[1,3], Blaine Roberts[2,4], Victor Faundez[1]

[1]Department of Cell Biology, Emory University School of Medicine, Atlanta, GA 30322, USA
[2]Department of Biochemistry, Emory University School of Medicine, Atlanta, GA 30322, USA
[3]Center for the Study of Human Health, Emory University, Atlanta, GA 30322, USA

This chapter is published in *STAR Protoc*. 2022 Apr 19;3(2):101334. doi: 10.1016/j.xpro.2022.101334 and is licensed under CC BY-NC-ND 4.0.

2.1 Abstract

This protocol describes how inductively coupled plasma mass spectrometry (ICP-MS) can quantify metals, sulfur, and phosphorus present in biological specimens. The high sensitivity of ICP-MS enables detection of these elements at very low concentrations, and absolute quantification is achieved with standard curves. Sulfur or phosphorus standardization reduces variability that arises because of slight differences in sample composition. This protocol bypasses challenges because of limited sample amounts and facilitates studies examining the biological roles of metals in health and disease. For complete details on the use and execution of this protocol, please refer to Hartwig et al. (2020).

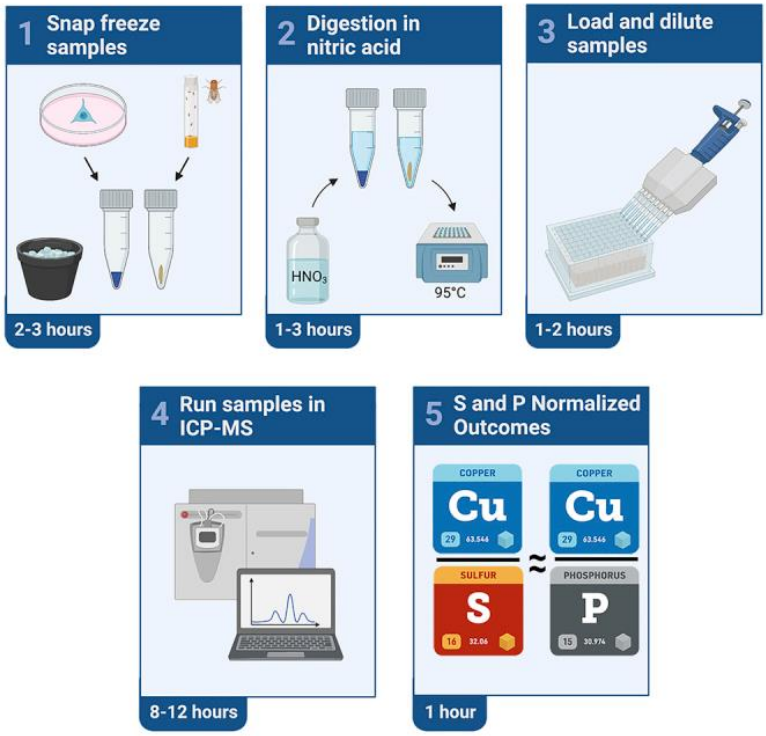

Figure S1. Graphical Abstract.

Graphical abstract describing sample preparation and analysis to measure metals by inductively coupled plasma mass spectrometry (ICP-MS).

2.2 Protocol Overview

This protocol describes how inductively coupled plasma mass spectrometry (ICP-MS) can quantify metals, sulfur, and phosphorus present in biological specimens. The high sensitivity of ICP-MS enables detection of these elements at very low concentrations, and absolute quantification is achieved with standard curves. Sulfur or phosphorus standardization reduces variability that arises due to slight differences in sample composition. This protocol bypasses challenges due to limited sample amounts and facilitates studies examining the biological roles of metals in health and disease.

2.3 Before you begin

This protocol was adapted from the recent publication from Hartwig et al. (2020) (based on McAllum et al. (2020) and Ganio et al. (2016)), where we quantified total larval copper content in several *Drosophila melanogaster* strains harboring different transgenes to modulate expression of the copper transporter ATP7, the homolog to human ATP7A and ATP7B. We confirm here that systemic overexpression of ATP7 does not significantly modify larval copper content.

The innovation of the present protocol is a streamlined oxygen-based detection method to quantify endogenous metals, phosphorus, and sulfur using a triple quadrupole ICP-MS instrument. This protocol streamlines the measurement of sulfur, phosphorus, and target elements to a single analysis. (This is in contrast to running the sample twice to obtain measurements of sulfur or phosphorus and then target elements, which requires more sample and instrument time.) The measurement of sulfur or phosphorus provides an internal standard that is proportional to protein, phospholipid, and nucleic acid concentration in cellular and larval samples. The sulfur and/or phosphorus content can be used as equivalent internal normalizing factors that are less susceptible to error as compared to measuring cell number, cellular protein, cellular DNA, or larval weight in equivalent yet independent samples where metals are measured.

Note: Room temperature in this protocol ranges from 20°C–25°C.

Note: Abbreviations: ICP-MS, inductively plasma-coupled mass spectrometry; PBS, phosphate buffered saline; EDTA, ethylenediaminetetraacetic acid; BCS, bathocuproinedisulfonic acid.

2.3.1 Culture cell lines

Timing: 1–3 h (24 h for cell attachment and growth)

Note: This protocol describes the steps for preparing SH-SY5Y neuroblastoma cell samples as in

. Steps are similar for other cell types, but certain parameters (e.g., centrifugation speed and time) may need to be optimized based on cell type and/or genotype. These areas of optimization are noted in the relevant sections of the protocol. Minor specific parameters which deviate from this standard protocol are described in the figure legends as appropriate. We recommend cells passage number 30 or less.

Note: Depending on the scale and purpose of your experiment, plan for total number of cells required, number of replicates, and various controls. This may require optimization depending on the cells and conditions you are using and the metals you plan to quantify. In our experiments, we aim to use 3–5 technical replicates per experimental condition. All replicates and conditions contain the same number of cells at the time of plating. The Biorad Cell Counter is used to measure cell counts. For accuracy, cell count measurements were made in duplicates.

Note: One million cells are more than sufficient for simultaneous metal, sulfur, and phosphorus detection, so we ensure a minimum of 1 million cells per replicate are plated on 10 cm plates or in total on a 15 cm plate (i.e., 1 million cells each across five 10 cm plates or 5 million cells on a single 15 cm plate). This number may vary depending on the cell type or line used, as cell sizes may differ. Here, we list the steps to use a 15 cm plate to prepare 5 replicates per condition. This protocol can be easily modified to utilize one 10 cm plate per replicate.

Note: Example: For SH-SY5Y cells, we seeded 6 million cells on a 15 cm dish. 48 h after seeding, the cells were at 60%–80% confluence. One 15 cm plate of SH-SY5Y cells at 80% confluency yields at least 10×10^6 cells (approximately 5 mg total protein lysate), which is sufficient to prepare 5 technical replicates (each with 2×10^6 cells or approximately 1 mg total protein).

1. On Day 1, seed a minimum of 5 million cells on a 15 cm plate.

2. On Day 2, confirm your cells at the desired level of confluency (we recommend at least 80% confluency).
    a. If you are not treating your cells, simply change media the day before you intend to freeze your samples.
    b. If cells are too sparse, change media and wait for 24 h.

2.3.2 Prepare for **D. melanogaster** *sample collection*

Timing: 30 min (optional 24 h)

3. Prior to the experiment, prepare the 1× PBS to be used for larval collection.

    Optional: Make SYLGARD™-filled petri dishes and allow to cure a minimum of 24 h. (Here, we used SYLGARD™-filled petri dishes as this helps maintain the surface tension of the PBS pool, which keeps larvae in a smaller field of view and easier to localize under the microscope. Empty petri dishes may also be used).

2.3.3 Prepare buffers for ICP-MS

Timing: 1–2 h

4. Prior to the experiment, prepare the chemicals and buffers to be used for ICP-MS, listed below. These can be used within 2 months.
    a. 2% nitric acid.
    b. Internal Standard for ICP-MS.
    c. Sulfur Calibration Standard for ICP-MS (100 mg/mL).
    d. Multielement Calibration Standard for ICP-MS (1,000 $\mu g * L^{-1}$ and 100 $\mu g * L^{-1}$).

CRITICAL: Nitric acid (HNO_3) is highly corrosive, and exposure to liquid and fume form can irritate the eyes, skin, and mucous membrane among other harmful outcomes. All work with concentrated nitric acid should be done with appropriate work practice controls and personal protective equipment (PPE), i.e., working with small volumes while using a chemical fume hood, lab coat, protective eyewear, and gloves. Nitric acid bottles can build pressure inside and should be vented monthly. Only plastic pipettes should be used with 70% nitric acid.

CRITICAL: You should prepare blank controls with no sample for all ICP-MS experiments. These blank controls that are free of any biological materials will enable the quantification of any elements derived from the tubes and reagents used.

CRITICAL: Use only analytical grade reagents to avoid contamination with trace metals. (See Problem 2).

Key resources table

REAGENT or RESOURCE	SOURCE	IDENTIFIER
Chemicals, peptides, and recombinant proteins		
ICP Internal Standard	AccuStandard	Cat#AG-INT2-ASL-5
Multi-element Calibration Standard #2A	AccuStandard	Cat#AG-MECAL2A-ASL-5
Sulfur Standard	Inorganic Ventures	Cat#AAS1
Phosphorus ICP Standard	AccuStandard	#ICP-41W-1, CAS: 7723-14-0
ICP-MS iCAP TQ Tune Solution	Thermo Fisher Scientific	Cat#S55611.AP
Trace Elements Serum L-2	Seronorm	Cat#203113
Trace Elements Serum L-1	Seronorm	Cat#201413
~Ultra-high purity oxygen (99.999%)	Select Gases	Cat#UN1072
ˆ∗~Copper(II) chloride	Sigma-Aldrich	Cat#203149; CAS: 7447-39-4
ˆ∗~Bathocuproinedisulfonic acid (BCS)	Sigma-Aldrich	Cat#B1125; CAS: 52698-84-7
~Phosphate Buffered Saline (PBS)	Corning	21-040-CV
∗~Trypsin Ethylenediaminetetraacetic Acid (EDTA) 0.25%	Corning	25-053-CI
∗~Ethylenediaminetetraacetic Acid (EDTA) Disodium Salt Solution	Sigma-Aldrich	E7889-100mL
∗~DMEM [+] 4.5 g/L glucose, L-glutamine, sodium pyruvate media	Corning	10-013-CV
Experimental models: Cell lines		

REAGENT or RESOURCE	SOURCE	IDENTIFIER
Human: SH-SY5Y Cells (Passage 20)	ATCC	Cat#CRL-2266; RRID: CVCL_0019
Human: HAP1 Cells (Passage 20)	Horizon Discovery	Cat#C631; RRID: CVCL_Y019
Experimental models: Organisms/strains		
D. melanogaster: wildtype: w1118 (female, 3rd instar)	Bloomington Drosophila Stock Center (NIH P40OD018537)	Cat#5905; RRID: BDSC_5905
D. melanogaster: Actin5C-GAL4,UAS-GFP (female, 3rd instar)	Bloomington Drosophila Stock Center (NIH P40OD018537)	Cat#42713; RRID: BDSC_42713
D. melanogaster: UAS-ATP7-wt (female, 3rd instar)	Richard Burke, Monash University, Australia	N/A
Software and algorithms		
Qtegra	Thermo Fisher Scientific	Cat#IQLAAEGABSFAOVMBCZ
Other		
∗~Biosafety Cabinet	NuAire	NU-425-400, Option A-0
∗~CO2 Incubator	Thermo Fisher Scientific	3110
∗~Refrigerated Microcentrifuge	Eppendorf	5425 R
∗~Refrigerated Centrifuge	Eppendorf	5810 R
ˆ∗~ Automated Cell Counter	Bio-Rad	1450102
ˆ∗~ Automated Cell Counter slides	Bio-Rad	1450011
#~ Drosophila units	SHEL LAB	SRI20P
#~ Drosophila Incubator, IB-15G	Lab Companion	AAH21176U
#~ Drosophila Vials	Genesee Scientific	32-110
#~ Dissecting Microscope	Zeiss	Stemi 2000
#~ Analytical Balance	OHAUS	PA114
#~ Dumont #2 Laminectomy Forceps	Fine Science Tools	11223-20

REAGENT or RESOURCE	SOURCE	IDENTIFIER
#~ Petri dishes (35 × 10 mm)	Genesee	32-103
#ˆ~ SYLGARD™ 184 Silicone Elastomer Kit	Dow	2646340
Chemical Fume Hood	N/A	N/A
~Microcentrifuge	Eppendorf	5430
~Dry Bath Heater	Corning	6895-FB
~iCAP TQ ICP-MS	Thermo Fisher Scientific	731546
ˆ~2DX prepFAST M5	Elemental Scientific	2DXF-73A
~MASTERBLOCK 96-Well Storage Plate, Polypropylene, 1.2 mL, Chimney Style, Round Bottom, Clear	VWR	780201
~X-Pierce Sealing Films for Robotics & High-Throughput Processing	Southern Labware	XP-100
Milli-Q® ultrapure water	N/A	N/A
ˆ~Adjustable Tip Spacing Multichannel Pipette 125 µL	Integra Biosciences	4722
ˆ~125 µL Tips for Adjustable Tip Spacing Multichannel Pipette	Integra Biosciences	4422
ˆ~Repeater Pipette	Eppendorf	4982000322
ˆ~0.5 mL tips for Repeater Pipette	Eppendorf	0030089456
ˆ~5 mL tips for Repeater Pipette	Eppendorf	0030089421
Microcentrifuge tubes	Sarstedt	72.607
Microcentrifuge tube screw caps	Sarstedt	65.716.999
15 mL tubes	VWR 352097	N/A
Kimwipes	Kimberly-Clark Professional	34155
Dry ice	N/A	N/A

Note: Symbols indicate the following: ~ this item or an equivalent; ∗ only necessary for cell culture experiments; # only necessary for D. melanogaster experiments; ˆ optional but recommended or experiment-specific.

2.4 Materials and equipment

2.4.1 Final buffer/chemical concentrations and volumes

PBS-Trypsin

Reagent	Final concentration	Volume to 44 mL
Trypsin EDTA 0.25%	10:1 v/v (0.02%)	4 mL
PBS		40 mL

Store at 4°C. Use within 1 month.

PBS-EDTA

Reagent	Final concentration	Stock concentration	Volume to 50 mL
EDTA	10 mM	0.5 M	1 mL
PBS			49 mL

Store at 4°C. Use within 1 month.

Media with copper(II) chloride for SH-SY5Y cells (300 µM)

Reagent	Final concentration	Stock concentration	Volume to 50 mL
Copper(II) chloride	300 µM	30 mM	500 µL
DMEM or media of choice			49.5 mL

Store at 4°C. Prepare same day.

Media with copper(II) chloride for HAP1 cells (400 µM)

Reagent	Final concentration	Stock concentration	Volume to 50 mL
Copper(II) chloride	400 µM	30 mM	667 µL
IMDM or media of choice			49.4 mL

Store at 4°C. Prepare same day.

Media with BCS for HAP1 cells (400 µM)

Reagent	Final concentration	Stock concentration	Volume to 50 mL
BCS	400 µM	400 mM	50 µL
IMDM or media of choice			50 mL

Store at 4°C. Prepare same day.

Standard fly flood

Reagent	Final concentration	Volume to 1 L	Mass
active dry yeast	4.8% (w/v)		48 g
cornmeal	12% (w/v)		120 g
agar	9% (w/v)		9 g
molasses	12% (w/v)		120 g
tegosept	0.24% (w/v)		2.4 g
propionic acid	0.9% (w/v)	9 mL	

Milli-Q water		900 mL	

Store at 4°C. Use within 3 weeks. (See Hartwig et al. (2020) and Gokhale et al. (2016) for more information).

Nitric acid (2%)

Reagent	Final concentration	Stock concentration	Volume to 1 L
Nitric acid	2%	70%	28.6 mL
Milli-Q water			971.4 mL

Store at room temperature. Use within 2 months.

Internal Standard for ICP-MS

Reagent	Final concentration	Stock concentration	Volume to 2 L
ICP Internal Standard	10 $\mu g * L^{-1}$	100 $mg * L^{-1}$	200 µL
2% Nitric Acid	2%	2%	2 L (volumetric flask)

Store at room temperature. Use within 2 months.

Sulfur Calibration Standard for ICP-MS

Reagent	Final concentration	Stock concentration	Mass to 50 g*
Sulfur Standard	100 $mg * L^{-1}$	1,000 $mg * L^{-1}$	5.0 g
2% Nitric Acid			45.0 g

Store at room temperature. Use within 2 months. (*See note at end of this section).

Multielement Calibration Standard for ICP-MS (1,000 ppb/1,000 $\mu g * L^{-1}$)

Reagent	Final concentration	Stock concentration	Mass to 50 g*
Multi-element Calibration Standard #2A	1,000 $\mu g * L^{-1}$	10,000 $\mu g * L^{-1}$	5.0 g
2% Nitric Acid			45.0 g

Store at room temperature. Use within 2 months. (*See note at end of this section).

Multielement Calibration Standard for ICP-MS (100 ppb/100 $\mu g * L^{-1}$)

Reagent	Final concentration	Stock concentration	Mass to 50 g*
Multi-element Calibration Standard #2A	100 $\mu g * L^{-1}$	10,000 $\mu g * L^{-1}$	0.5 g
2% Nitric Acid			45.0 g

Store at room temperature. Use within 2 months. (*See note at end of this section).

Note: Preparing the standard solution by weight rather than by volume is recommended, as this method is more precise (0.02% precision for 50 g on a balance with 0.01 g accuracy). Additionally, it

is easier to weigh larger volumes and there is reduced risk of contamination as fewer containers are required.

CRITICAL: For safety information while working with nitric acid (HNO_3), please refer to Prepare buffers for ICP-MS in the Before you begin section.

Alternatives: We recommend using an adjustable tip spacing multichannel pipette and the 2DX prepFAST M5 system to prepare and run samples and standards for ICP-MS experiments in order to save time and reduce the likelihood of pipetting error, particularly when working with large numbers of samples. However, users can also prepare and load samples without this equipment (see notes throughout the protocol where applicable).

2.5 Step-by-step method details

2.5.1 Cell sample preparation

Cell growth and drug treatment

Timing: 1–2 h

Confirm that your cells will be ready the following day and change media.

1. If your experiment involves drug treatments:
    a. When cells reach approximately 80% or desired level of confluency, change media and replace with media containing vehicle or your drug of interest.
    b. Treat for 24 h.

Note: Here, we used 300 µM copper(II) chloride in SH-SY5Y cells. We used 400 µM copper(II) chloride and 400 µM BCS in HAP1 cells.

Note: Drug and metal concentrations should be selected based on the cell type studied and the goals of the experiment (see Problem 3). If a metal or drug dose that may cause toxicity is being tested for ICP-MS, cell survival in increasing concentrations of the metal or drug should be performed first. For example, the IC50 for copper can for copper can be determined by quantifying cell survival using colorimetric assays like crystal violet (Comstra et al., 2017) or fluorescence assays such as

Resazurin, and primary cultured fibroblasts can be treated with 50 μM without overt toxicity (Morgan et al., 2019). Thus, we recommend treating cells with 50–400 μM copper(II) chloride.

2. If you are not treating your cells:
    a. Simply change media the day before you intend to freeze your samples.

Preparation of cell pellets

Timing: 2–3 h

Detach your cells and snap freeze them for storage at −80°C.

Note: You can detach cells using PBS with either trypsin or EDTA (referred to here as PBS-Trypsin and PBS-EDTA). We describe both methods here, as trypsin may be preferred if speed of dissociation is a priority, whereas EDTA may be preferred for some experiments as it better maintains cell integrity. Additionally, some highly adherent cell types (e.g., fibroblasts) may be difficult to detach using PBS-EDTA. In the data shown here, we used PBS-Trypsin.

Note: The concentration of trypsin used to detach cells may differ depending on cell type. In SH-SY5Y cells, the 10:1 v/v dilution of 0.25% trypsin-EDTA in PBS described here is sufficient to detach cells without cell damage.

Note: Cell pellets can be prepared up to a month before the ICP-MS analysis.

3. Preparation on the day of the experiment:
    a. For each 15 cm plate, label 1 × 15 mL tube and 5 × microcentrifuge tubes.
    b. Label an additional 15 mL tube and 5 × microcentrifuge tubes for blank controls.
    c. If using PBS-Trypsin:
        i. Warm PBS and PBS-Trypsin to 37°C.
        ii. Place additional PBS on ice.
        iii. Fill each 15 mL tube with 3 mL of media. (This will neutralize the trypsin).
    d. If using EDTA:
        i. Place PBS and PBS-EDTA on ice.
    e. Get dry ice.

f. Cool centrifuge and microcentrifuge to 4°C.

Dissociation with trypsin

Note: Skip to step 11 if using PBS-EDTA.

4. Wash cells once with 10 mL of warm PBS.
5. Add 3 mL PBS-Trypsin and incubate for 2 min at 37°C until cells begin to detach.

   Note: This may take longer depending on the cell type.

   Note: Do not treat cells too long with trypsin, as this will can cause cell rupture and alter cytoplasmic pools of metals and other elements.

6. Detach cells from the plate with gentle aspiration using a pipette.
   a. Transfer cell suspension to a 15 mL tube and dilute with 6 mL of warm PBS.
   b. For blank controls, add 3 mL of PBS with trypsin and 6 mL of PBS to the corresponding 15 mL tube.
7. Centrifuge at 130 × *g* (800 rpm) for 5 min at 4°C to pellet the cells.
8. Remove supernatant.
   a. Resuspend in 5 mL of ice-cold PBS.
   b. Mix well and add 1 mL of your cell suspension to each microcentrifuge tube.

   Note: If you wish to prepare samples with known cell number, replace step 8 with steps 19 and 20.

9. Centrifuge at 210 × *g* (1,500 rpm) for 5 min at 4°C to pellet the cells.
   a. Remove supernatant (taking care to remove as much PBS as possible).
   b. Immediately transfer tubes to dry ice to snap freeze your samples.
10. Leave samples on dry ice for 15–30 min.
    a. Transfer to −80°C for long-term storage.

    Pause point: Cell pellets can be prepared up to a month before the ICP-MS analysis.

Dissociation with EDTA

Note: Skip to step 19 if using PBS-Trypsin.

11. Wash each plate twice with 10 mL ice-cold PBS.
12. Add 10 mL PBS-EDTA to each plate and place on ice for 10 min.

    Note: This may take longer depending on the cell type.

13. Detach cells from the plate with gentle aspiration using a pipette.
    a. Place the suspension in a 15 mL tube.
    b. For blank controls, add 10 mL of PBS-EDTA to a tube.
14. Centrifuge at 130 × *g* (800 rpm) for 5 min at 4°C to pellet the cells.
15. Remove the supernatant.
    a. Resuspend the pellet in 5 mL of ice-cold PBS.
    b. Transfer to labeled screw cap tubes.

    Note: If you wish to prepare samples with known cell number, replace step 15 with steps 19 and 20.

16. Centrifuge this cell suspension at 210 × *g* (1,500 rpm) for 5 min at 4°C.
17. Remove the supernatant (taking care to remove as much PBS as possible).
    a. Immediately transfer tubes to dry ice to snap freeze your samples.
18. Leave samples on dry ice for 15–30 min before transferring to −80°C for long-term storage.

    Pause point: Cell pellets can be prepared up to a month before the ICP-MS analysis.

Normalization of sulfur and phosphorus content to cell count

Note: As sulfur and/or phosphorus content were used to standardize measurements across replicates, it is not necessary to count cells before preparing cell pellets. Phosphorus and sulfur are present in multiple biomolecules and represent 1.1% and 0.2% of the mass of a human body respectively (see ID#101913 in BioNumbers (Milo et al., 2010; Rumble, 2021)). These facts make sulfur and phosphorus good standards likely to be stable under diverse biological natural and

experiments conditions. Sulfur is present in cysteine and methionine in proteins and in sugars, nucleic acids, lipids, vitamin cofactors and metabolites, thus acting as a proxy for cell mass that can replace cell number counts or protein determinations. A compendium of biomolecules that contain sulfur can be found in Raab and Feldmann (2019). Phosphorus is an abundant element present in nucleic acids, nucleotides, and phospholipids, making it another good proxy for abundant biomolecules (Walsh, 2021).

Note: If you wish to prepare samples with known cell number as we did here, incorporate these additional steps as you prepare the cell pellets.

19. If preparing samples with known cell number (otherwise, disregard):
    a. After dissociating your cells and transferring the cell suspension to a 15 mL tube (step 6 or 13):
        i. Mix well and count cells.
        ii. Calculate the volume of PBS needed to aliquot 1 mL of your cell suspension per tube with your desired cell number.
            1. (Example: For 1×10^6 cells per tube, if you count 8×10^6 cells, resuspend in 8 mL PBS).
20. If preparing samples with known cell number (otherwise, disregard):
    a. After the first centrifugation (step 7 or 14):
        i. Resuspend in approximately *half* of the cold PBS needed to obtain your desired cell concentration.
        ii. Mix well and count cells again.
        iii. Dilute the cell solution with cold PBS to get desired cell concentration.
        iv. Mix well and add 1 mL of your cell suspension to each microcentrifuge tube.

Note: As cells can be lost during centrifugation, not adding the full volume of PBS initially ensures that cells are not over-diluted and final counts are accurate.

Note: For our samples, we generated cell number curves in SH-SY5Y cells (Figure 1A) and HAP1 cells treated with copper(II) chloride or BCS (Figures 2A and 2B). Example for SH-SY5Y cells: We first resuspended cells to 2×10^6 cells/mL to prepare samples with 1×10^6, 2×10^6, or 3×10^6 cells (0.5 mL, 1 mL, or 1.5 mL of cell suspension per tube, respectively). We diluted the remaining cells by 4 in PBS (500,000 cells/mL) to prepare samples with 250,000 or 500,000 cells (0.5 mL or 1 mL of cell suspension per tube, respectively).

Note: The number of cells per sample should be optimized for each mass spectrometry system and selected based on the expected outcomes, i.e., more cells may be needed to detect smaller differences between groups. Our results suggest high sensitivity for detection of as few as 250,000 cells, with similar correlations between sulfur or phosphorus and metal content for all groups (Figures 1C and 1E, see r^2 values). (See the **Limitations** section for additional discussion of the sensitivity of measurements of ultra-trace elements like Co.) Based on extrapolation from the cell counts and standard curves used here, we anticipate that our ICP-MS system can accurately quantify Fe, Cu, and Zn from samples with as few as 1,000 cells, though we prepare larger samples when cells can easily be collected in bulk.

2.5.2 D. melanogaster *larvae sample preparation*

Larvae collection

Timing: 1–2 h

Collect larvae from each genotype and wash in PBS to remove food particles.

Note: *D. melanogaster* crosses utilized the UAS system (Brand and Perrimon, 1993) and were raised in polystyrene vials containing 10 mL of standard fly flood. Vials were kept at 24°C in a humidified incubator with a 12 h:12 h light:dark cycle. Females from the Actin5C-GAL4,UAS-GFP driver line were crossed to either male w1118 animals or male UAS-ATP7-wt. This allowed comparison between controls and animals overexpressing ATP7 (later referred to as Con and ATP7-OE, respectively). (See Hartwig et al. (2020) for more information).

Note: Complete the steps below for each genotype separately. After collecting, weighing, and freezing all the larvae for one genotype, rinse both petri dishes and refill with fresh PBS before collecting larvae from an additional genotype.

21. Preparation on the day of:
    a. Place small puddles of 1× PBS in each of two SYLGARD™-filled petri dishes or empty petri dishes.
    b. Get tweezers, Kimwipes, analytical balance, and dry ice.

Note: The PBS is being used to rinse the larvae, so the quantity does not need to be precise. A smaller pool of PBS in the petri dish where larvae are initially collected will make it easier to keep within the field of view under the microscope.

22. Use forceps to collect 3–5 wandering, third-instar larvae, and place them in the pool of 1× PBS in one of the petri dishes.

Note: The initial pool of PBS will become cloudy with food residue, so it is best to collect larvae from the vial in small batches.

23. With aid of a dissecting microscope, select female larvae for analysis and remove male larvae.

Note: Male larvae can be distinguished by the presence of gonads under the cuticle in the posterior ventral segment of the animal (Karabasheva and Smyth, 2020).

24. Lightly grasp an individual larva with the forceps and gently jostle it side-to-side within the PBS to remove the food residue.
    a. If any food residue is still visible after this process, use the side of one forceps tip to gently brush along the larval body to dislodge the food residue.
25. Once cleaned, move female larva to the pool of PBS in the second petri dish.

Note: If the larvae are cleaned sufficiently prior to being moved to the second petri dish, this PBS should remain clear and will not need to be replaced as additional larvae of the same genotype are collected. If food particles are visible in the second petri dish, repeat steps 24 and 25 using a third petri dish.

26. If additional animals are needed, clean the petri dish used in step 22, add fresh PBS, and repeat steps 23–25.

Weighing and freezing larvae

Timing: 1–2 h

After all animals of a single genotype have been collected, individually weigh and freeze each larva.

27. Use forceps to remove an individual larva from the petri dish. Place it on a Kimwipe to remove PBS.
28. Use forceps to pick up larva from the Kimwipe and place it gently in a microcentrifuge tube. Screw on the cap and label the tube.
    a. For blank controls, prepare empty microcentrifuge tubes.

    Note: If you wish to prepare samples with known larval weight, first determine the baseline weight of the microcentrifuge tube and screw cap using an analytical balance. Record this value. Reweigh the microcentrifuge tube with the larva and cap and record this value. The baseline value can be subtracted from this post-weight to determine the weight of individual larva. See steps 31 and 32 for pooling samples.

29. Transfer tube to dry ice to snap freeze the larva.
30. Repeat steps 27–29 for each larva collected.

    Pause point: Samples can be stored at −80°C for up to a month before the ICP-MS analysis.

Normalization of sulfur or phosphorus content to fly number or weight

Timing: 1–2 h

Pool larvae together to prepare samples that can be normalized to fly number and/or weight.

Note: As sulfur content is used as a proxy for fly mass to standardize measurements across replicates (see above: “Normalization of Sulfur Content to Cell Count”), it is not necessary to weigh flies before preparing samples. If you wish to prepare samples with known fly weight and/or pool samples from multiple larvae with similar total weight as we did here, incorporate these additional steps.

31. If preparing samples with known larvae weight (otherwise, disregard):
    a. To pool larvae, assign larvae by weight to groups for analysis so that the average fly weight is similar across samples.
32. If preparing samples with known larvae weight (otherwise, disregard):
    a. Gather all microcentrifuge tubes with individual larva and place on dry ice.
    b. Combine all larvae for a given group in a single tube.
        i. This can be done using forceps or by gently tapping the microcentrifuge tube containing the larvae to be transferred over the top of the destination tube.
        ii. If the larva is stuck to the side of the tube, gently flick the tube or tap against the bench to dislodge it before transferring.

Note: For our samples, we analyzed between 2–3 independent biological replicates of groups consisting of 1, 2, 4, and 8 individual larvae for each genotype (Figure 1F). This data was pooled to give a total of 12 independent replicates for WT flies and 10 independent replicates for ATP7-OE flies (Figures 1F and 1G).

Note: The number of larvae per sample should be optimized for each mass spectrometry system and selected based on the expected outcomes, i.e., more flies may be needed to detect smaller differences between groups. (See **Problem 3**.) Our results suggest high sensitivity for detection even for single larva, with similar correlations between sulfur and metal content for all groups (Figure 1G, see r^2 values).

2.5.3 ICP mass spectrometry

Timing: 1–12 h depending on the number of samples

Sample preparation

Timing: 1–3 h depending on the number of samples

Dissolve samples in 70% nitric acid.

33. Turn on heat block and set to 95°C.

34. Rinse a 25 mL or 50 mL tube with MilliQ water.
    a. Add a small volume 70% nitric acid (approximately 2 mL) to the tube.
35. Add 20 µL 70% nitric acid to each sample using the repeating pipettor. Take care to ensure that the same volume is added to each tube.
    a. Briefly centrifuge to collect the nitric acid and the sample at the bottom of the tube if required.

Note: Use as little nitric acid as possible to dissolve your samples to maximize the metal content loaded into the ICP-MS. 20 µL is the minimum volume we used. Larger volumes can be used if needed, but it is recommended that you start from 20 µL nitric acid and only add more acid if the sample does not fully dissolve. We increased the volume of acid used for samples with 1 million cells or more to be able to re-run samples if necessary (see volumes listed in Table 1). We scaled the volume of acid based on cell or larvae number; however, this is not necessary. We would recommend increasing the amount of acid only if necessary to yield a homogeneous solution clear of precipitates for each sample.

36. Incubate samples in the heat block at 95°C for 10 min.

Note: Fully dissolved samples should be fully homogeneous without any particulates and are typically yellow in color. For samples with a particularly high lipid content, like brain tissue, follow the incubation with nitric acid with equal volume of concentrated trace element grade hydrogen peroxide. For further details, see McAllum et al. (2020) and Problem 1.

Pause point: Samples in 70% nitric acid can be immediately diluted with 2% nitric acid for analysis or stored at room temperature for 1–3 months. (Typically, we leave samples at room temperature for 24 h before diluting and running the samples. See Problem 5 if samples are stored long-term and undergo evaporation).

Table 1. Nitric acid dilutions used in this study

Sample type	Number cells or larvae	Volume nitric acid used (µL)
SH-SY5Y Cells	250,000	20
SH-SY5Y Cells	500,000	20

SH-SY5Y Cells	1 million	50
SH-SY5Y Cells	2 million	50
SH-SY5Y Cells	3 million	50
SH-SY5Y Cells, treated with vehicle or copper (Figure 1)	Between 1–2 million	50
HAP1 Cells, treated with vehicle, copper, or BCS (Figure 2)	Between 0.5–3 million	50
D. melanogaster	1	20
D. melanogaster	2	40
D. melanogaster	4	80
D. melanogaster	8	80
Blank	–	20

Sample dilution

Dilute samples in 2% nitric acid and load them into the 96 well plate.

37. Dilute samples 1:40 in 2% nitric acid (add 780 µL to each tube containing 20 µL of sample).
    a. Transfer each of your samples to a deep 96 well plate (minimum volume 400 µL).

Note: Alternatively, you can transfer the samples in 70% acid directly to the deep 96 well plate and dilute in 2% nitric acid in the well plate.

Note: We used adjustable tip spacing multichannel pipettes to load our samples in order to save time and reduce the likelihood of pipetting error. This is not necessary but is suggested when working with large numbers of samples.

Note: We recommend arranging your samples in a tube rack as you load them into the 96 well plate, then take a picture of the layout. This will help ensure that the plate layout can be matched to each sample.

Pause point: If required, seal the 96 well plate with sealing tape and store at room temperature for up to 1 month; otherwise, analyze immediately. (Evaporation is more easily controlled with concentrated nitric acid; thus, it is typically recommended to stop after step 36 if necessary).

Instrument set-up, calibration, and running samples

Note: Operating procedures may vary between instruments and models. Contact the instrument technical specialist to learn more about how to configure the ICP-MS being used.

Note: We recommend the use of the 2DX prepFAST M5 system. Alternatively, a user can manually prepare the standard curve through standard dilution practices.

Note: Store all standards in polyethylene bottles washed using 1% HNO_3 in MilliQ-H_2O prior to use.

Note: The wash, sample dilution, and sample carrier solutions are 2% nitric acid in 18.2 Milli-Ω water.

Note: Here, quantitation of trace elements in larvae or cultured cells were determined with a Thermo iCAP-TQ series inductively coupled plasma triple quadrupole mass spectrometer (ICP-MS). A triple quadrupole ICP-MS is required for this method. The instrument was operated in oxygen reaction mode with detection of elements of interest with the third quadrupole (see Table 2). This method removes polyatomic interferences by mass shifting the target element by 16Da after reaction with oxygen. The oxygen mass shift and MS/MS detection using a triple quadrupole instrument are critical to measure sulfur and phosphorus. The measurement of S^+ and P^+ with standard single quad ICP-MS using oxygen mass shift suffers from the inability to distinguish $^{48}SO^+$ & $^{47}PO^+$ from $^{47}Ti^+$, $^{48}Ca^+$, $^{36}Ar^{12}C^+$ and $^{48}Ti^+$ spectral interferences. The implementation of a triple quadrupole allows for the first quad to mass filter for m/z ion at 31 and 32 which filters out the Ti and Ca interference ions. The reaction of S^+ and P^+ with O_2 in the octopole then mass shifts them by one oxygen. Because the $^{47}Ti^+$, $^{48}Ti^+$, and $^{48}Ca^+$, and spectral interferences were filtered out by the first quadrupole, the detection at m/z 47 and 48 of $^{48}SO^+$ & $^{47}PO^+$ after the third quadrupole occurs without poly atomic or ion Ca and Ti interference (Diez Fernández et al., 2012; Balcaen et al., 2013). Together, the relatively recent introduction of the triple quad ICP-MS instruments improves the selectivity and sensitivity for detection of S and P in biological samples.

Table 2. Typical operational ICP-MS parameters for Thermo iCAP-TQ-ICP-MS

Parameter	Value
RF power	1,550 W
Sample depth	5.0 mm
Nebulizer flow	1.12 $L*min^{-1}$

Auxiliary Flow	0.8 L min^{-1}
Spray chamber temperature	3°C
Extraction lens 1, 2	−195, −215 V
Reaction gas	O_2, 0.3 mL min^{-1}

38. Prepare a nine-point external calibration curve to quantify iron (Fe), copper (Cu), manganese (Mn), cobalt (Co), and zinc (Zn).
    a. Prepare 50 mL stock solutions of Multielement Calibration Standard for ICP-MS in 2% nitric acid (1,000 and 100 $\mu g * L^{-1}$; see Prepare buffers for ICP-MS and **Materials and equipment**).
    b. Prepare solutions for the calibration curve. The calibration curve values should range from 0.5 to 1,000 $\mu g * L^{-1}$ and increase by 2× at each point (0, 0.5, 1, 5, 10, 50, 100, 500 and 1,000 $\mu g * L^{-1}$).
        i. Dilutions can be prepared using the 2DX prepFAST M5 system (Elemental Scientific) or manually through standard dilution practices.
39. Control and monitor for potential instrument drift by automatic dilution of the sample with the Internal Standard for ICP-MS during sample introduction using the 2Dx prepFAST M5 system.

    Note: The Internal Standard for ICP-MS is a reference element solution containing 10 $\mu g * L^{-1}$ of Li-6, Sc, Y, In, Tb, and Bi (see Prepare buffers for ICP-MS and Materials and equipment). The 2Dx prepFAST M5 system automatically dilutes the sample with the Internal Standard during sample introduction. Commonly, the Internal Standard solution is introduced with the sample via a 'T' piece using a peristaltic pump. Alternatively, the Internal Standard can be added manually immediately before analysis is performed; however, this is exceedingly rare.

40. Prepare a four-point standard curve for S.
    a. Dilute stock solutions of the Sulfur Calibration Standard for ICP-MS, a 100 $mg * L^{-1}$ solution (0.5, 1, 5, 10 $mg * L^{-1}$), in 2% nitric acid. Prepare 50 mL of each concentration.

b. Dilutions can be prepared using the 2DX prepFAST M5 system (Elemental Scientific) or manually through standard dilution practices.

Note: Here, we did not use a phosphorus standard, so all data in Figure 2 are presented as counts per second (cps). However, we plan to perform quantitation of P similarly to S in the future using a certified P standard. (See the key resources table for catalog information for the Sulfur and Phosphorus Standards).

41. Warm-up and tune the instrument as recommended by the manufacturer. (Typically requires 20–30 min).

Note: ICP-MS iCAP TQ Tune Solution is the tuning solution for instrument optimization (see the key resources table for catalog information). It contains 1 μg L^{-1} of cerium (Ce), cobalt (Co), lithium (Li), thallium (Tl), and Y in 2% nitric acid.

Note: Table 3 contains the acquisition parameters used. The r^2 for calibration curves was > 0.9998. The prepFast system was set up with a 0.25 mm ID sample probe and a 250 μL sample loop. The 0.25 mL Precision Method used was provided as a prebuilt program by the manufacturer (Elemental Scientific) that is standard with any PrepFAST system and automates sample uptake, dilution, internal standard introduction, and sample introduction.

42. Make up Seronorm Trace Elements Serum L-1 and L-2 standard reference material according to the manufacturer's instructions.

Note: Seronorm™ Trace Elements Serum L-1 and L-2 are used to externally assess analytical performance.

43. Replace any sealing tape previously added with X-Pierce Sealing Film for robotics.
44. Add samples and Seronorm Trace Elements Serum L-1 and L-2 to the sample deck and build the worklist.
45. Run the Seronorm Trace Elements Serum L-1 and L-2 (800 μL of a 1:40 dilution in 2% nitric acid) and verify measurement of elements are within +/-20% of the accepted values (see Problem 2).

46. Continue with measurement of samples (see Problem 3 and Problem 4).
    a. Intersperse a Seronorm measurement every 20–30 samples.
47. Conduct data analysis within the Qtegra software.
    a. Export values from Qtegra.
    b. Statistical analysis can be conducted with Excel, GraphPad Prism, or any other relevant statistical analysis software.

Table 3. Thermo iCAP-TQ-ICP-MS acquisition parameters

Element	Q3 analyte	Internal standard	Dwell time (s)	Q1 resolution[a]
Phosphorus	31P.16O	45Sc.16O	0.05	High
Sulfur	32S.16O	45Sc.16O	0.1	High
Scandium	45Sc.16O	–	0.02	Normal
Manganese	55Mn	45Sc.16O	0.05	Normal
Iron	56Fe.16O	45Sc.16O	0.1	Normal
Cobalt	59Co	45Sc.16O	0.05	Normal
Copper	63Cu	45Sc.16O	0.05	Normal
Zinc	66Zn	45Sc.16O	0.05	Normal
Selenium	80Se.16O	89Y.16O	0.1	Normal
Yttrium	89Y.16O	–	0.02	Normal

[a] Q3 resolution was set to normal for all of the elements. The list can be expanded to include other elements of interest. Each element was measured 4 times.

2.6 Expected outcomes

This protocol describes how inductively coupled plasma mass spectrometry (ICP-MS) can be used to quantify metals, sulfur, and phosphorus present in biological specimens. Classically, ICP-MS and trace analysis are optimized for geological and environmental samples. These sample types do not have the same constraints as biological samples, which have limited amounts available for analysis. With current ICP-MS analytical technology, the measurement of trace elements in the biological sciences is readily achievable, yet many core ICP-MS facilities require large mL to gram quantities. Here we describe the application of ICP-MS to biological samples.

The main adaptions that are required relate to sample introduction and sample preparation. One challenge in measuring biological samples that have unknown quantities and/or contain µg of sample (rather than gram) is normalization. When conducting an analysis of trace-elements, it is not possible to normalize with housekeeping proteins or total protein in each sample as they are destroyed in the ionization process. Normalization to cell number is possible but can be time-consuming and can have low accuracy, as determined by the coefficient of variation (see Table 5). However, ICP-MS offers a similar internal normalization approach. Here, we apply the measurement of sulfur or phosphorus as a surrogate marker of total biological content. Measurement of sulfur and phosphorus is made possible by the recent commercialization of the triple quad ICP-MS combined with the use of oxygen as a reaction gas. This is particularly useful when care is taken to prevent contaminations from common buffers and reductants (e.g., dithiol threitol, sodium dodecyl sulfate, ammonium sulfate, or drugs that contain sulfur in their structure). Here, we illustrate how this protocol can be used to quantify metals in cultured cells and *D. melanogaster* (Figure 1). We compared the performance of sulfur or phosphorus as surrogate standards with similar outcomes (Figure 2). Both standardization methods similarly detect cellular conditions where copper content has been increased by copper chloride incubation (Figures 1D and 2, blue symbols) or decreased by the addition of the copper chelator BCS (Figure 2, black symbols). The sensitivity of the standardization method can be observed in Figure 2A, where incubation with BCS increases the amount of sulfur per cell due to the presence of 2 mols of sulfur per mol of BCS ($C_{26}H_{20}N_2O_6S_2$, $p < 0.0001$, Figure 2A, compare BCS and control). This shift is abrogated when normalization is performed with phosphorus (Figure 2A). Sulfur content is highly correlated with cell number and fly number (Figures 1A, 1B, and 1F) and is a more accurate normalizing factor with a lower coefficient of variation than cell number (see Table 5). Similar results are obtained when cell number is correlated with phosphorus content (Figure 2A, sulfur $r^2>0.86$; phosphorus $r^2 >0.74$). We compared the correlations between cell numbers with either sulfur or phosphorus content and noticed no differences by Fisher r-to-z transformation statistics

(Figure 2A). There is a strong fit of sulfur content to cell number correlation with a linear model, as depicted in Figure 1B showing a predicted vs actual plot for each replicate with r^2 values >0.9 calculated using Prism v9.2.0. Our results are highly consistent across replicates, with accurate quantification of biologically relevant metals even in single larva or with as few as 250,000 cells.

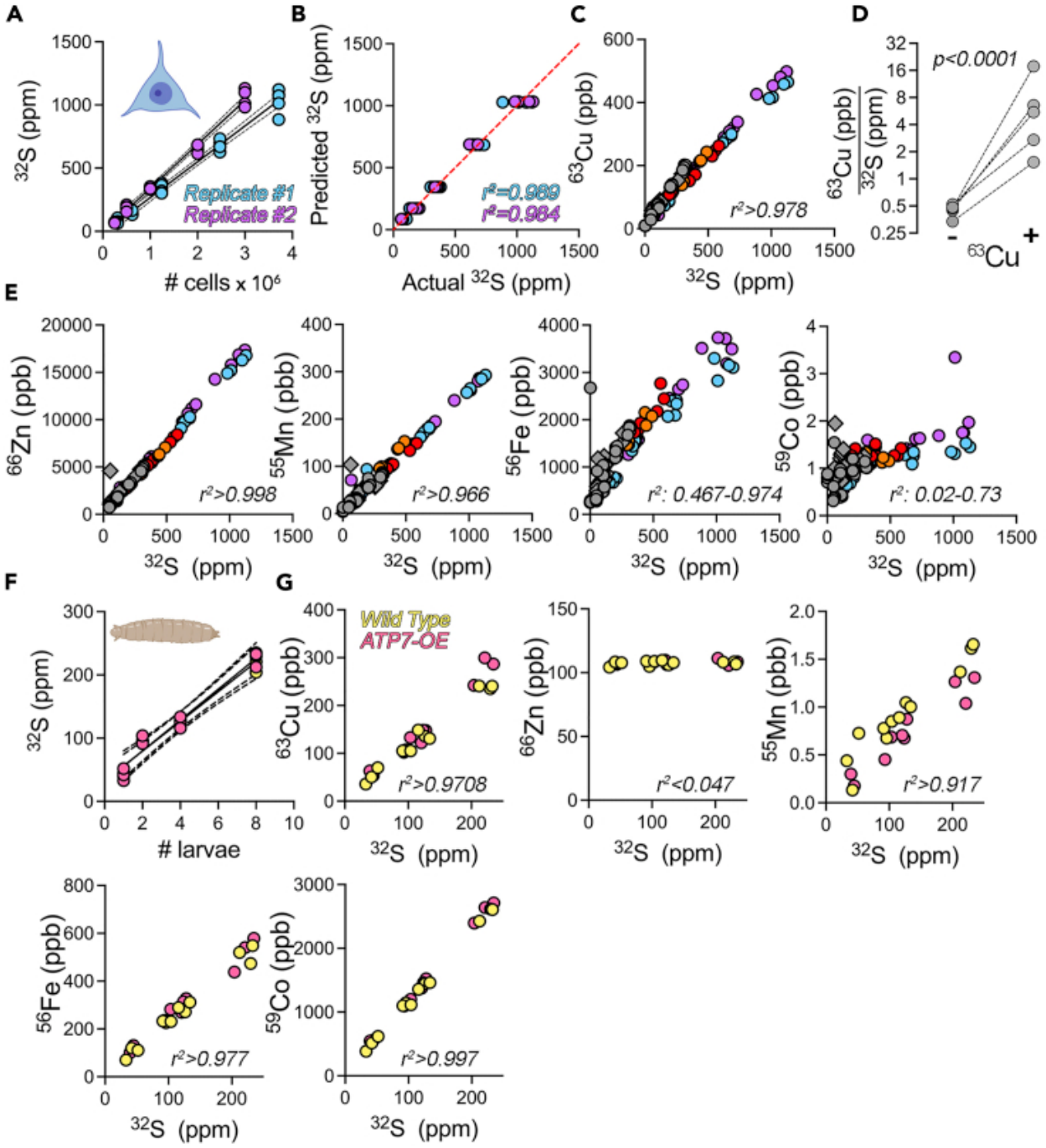

Figure 1. Metal quantification in SH-SY5Y cells and *D. melanogaster* larvae using ICP-MS.

(**A–E**) Metal content in WT SH-SY5Y cells (colors indicate biological replicates). (**A** and **B**) 32S correlation with cell number using a linear model. The 2 replicates with samples for all cell numbers quantified were included in this analysis. (**B**) Plot of predicted vs. actual of 32S content using a linear model (r^2 values = 0.969 and 0.964). Predicted model considers a straight line using as least squares regression fitting with an origin at 0. (**C**–**E**) 63Cu, 66Zn, 55Mn, 56Fe, and 56Co versus 32S content. (**C** and **E**) Plot of metal content vs. sulfur content. (**D**) 63Cu normalized to 32S content in five distinct single cell clonal lines of WT SH-SY5Y cells treated with 300 μM copper for 24 h (two tailed Mann-Whitney test $p < 0.001$). (**F** and **G**) Metal content in WT and ATP7-OE larvae (yellow and pink, respectively). (**F**) 32S content versus larva number. (**G**) 63Cu, 66Zn, 55Mn, 56Fe, and 56Co vs. 32S content. Abbreviations: sulfur (32S), copper (63Cu), zinc (66Zn), manganese (55Mn), iron (56Fe), cobalt (56Co). In all graphs, r^2 values depicted as a range represent the lowest and highest value in each biological replicate.

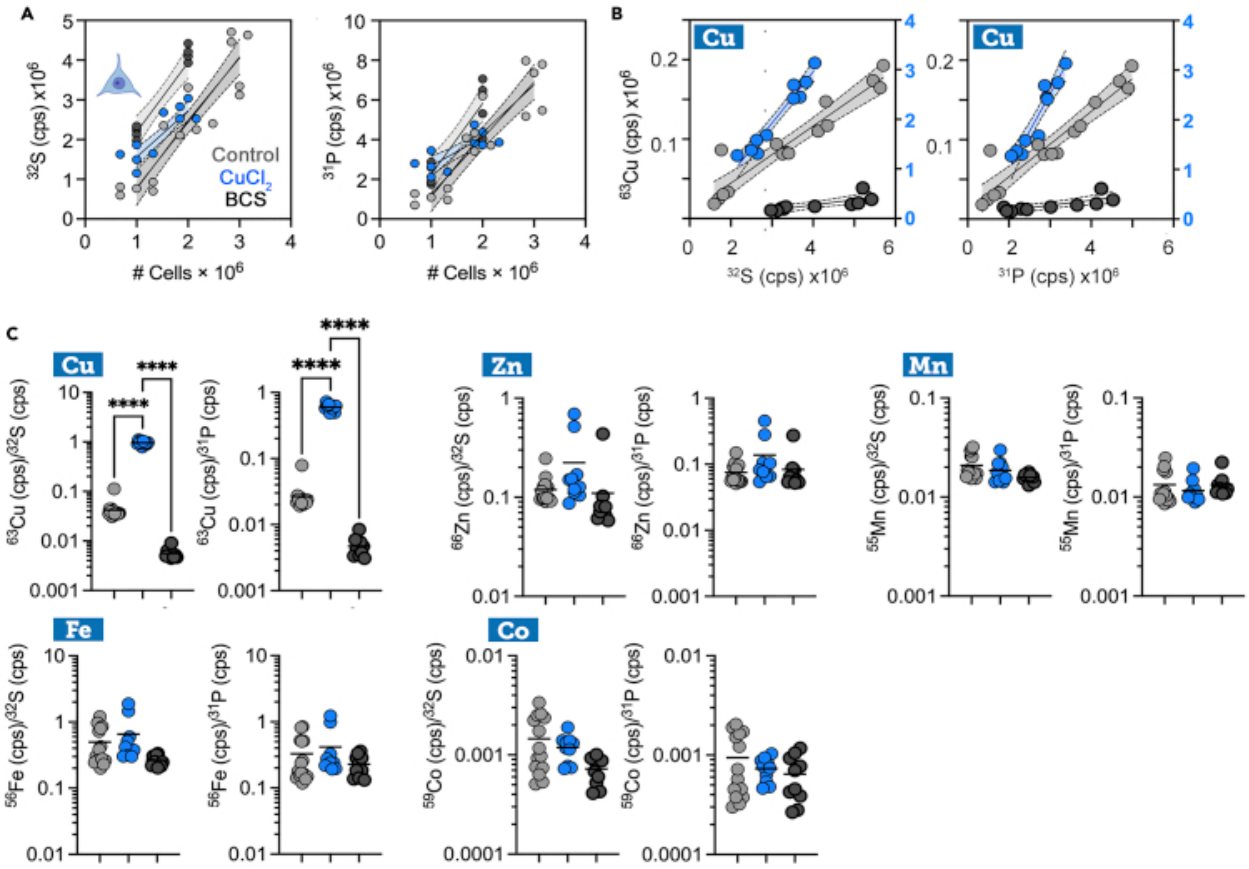

Figure 2. Comparison of sulfur and phosphorus standardized metal quantification in HAP1 cells using ICP-MS.

(**A**) Metal content in increasing numbers of WT HAP1 cells control (gray symbols) or incubated in the presence of either copper chloride (400 μM, blue symbols) or BCS (400 μM, white symbols) for 24 h. r^2 for sulfur correlations = 0.8924, 0.8787, and 0.8619 for control, copper chloride-, and BCS-treated cells. r^2 for phosphorus correlations = 0.8610, 0.7429, and 0.8317 for control, copper chloride-, and BCS-treated cells. (**B**) 32S and 31P correlation with copper content in control, copper chloride-, and BCS-treated cells. r^2 for sulfur correlations = 0.9014, 0.9464, and 0.6233 for control-, copper chloride-, and BCS-treated cells. r^2 for phosphorus correlations = 0.9012, 0.9082, and 0.6174 for control, copper chloride-, and BCS-treated cells. In (**A** and **B**), best fit correlation and 95% confidence interval are depicted. (**C**) 63Cu, 66Zn, 55Mn, 56Fe, and 56Co normalized to 32S and 31P content. Symbols colored as in (**A**). Two-tailed Anova with Bonferroni multiple corrections reveal p<0.001 for copper measurements using both sulfur and phosphorus normalization. All other metal determinations were not significantly different. (Note: Cells were prepared according to this protocol with the following

changes: steps 3–7: Cells were collected in 2 mL PBS-trypsin, neutralized with 1 mL media, and diluted with 7 mL PBS. Step 9: Cells were microcentrifuged at 3,000 g for 2 min).

Table 4. Average metal content per cell in SH-SY5Y cells[1] plus or minus SD

	Sulfur	Copper	Zinc	Manganese	Iron	Cobalt
Metal content (g)	8.7E-12	4.7E-15	1.4E-13	2.6E-15	4.5E-14	4.2E-17
SD (g)	4.5E-12	1.8E-15	7.3E-14	1.4E-15	1.6E-14	2.7E-17
Metal content (fg)	8700	4.7	140	2.6	45	0.042
SD (fg)	4500	1.8	73	1.4	16	0.027

[1] Data in this table correspond to Figure 1.

Table 5. Coefficient of variation in metal content in SH-SY5Y cells[1] normalized to cell number or sulfur content

	Copper	Zinc	Manganese	Iron	Cobalt
Normalized to cell number	42%	61%	75%	61%	106%
Normalized to sulfur	23%	41%	51%	42%	81%

[1] Data in this table correspond to Figure 1.

This method is robust and can be used to compare groups based on genotype or drug treatment. For example, we illustrate a dramatic increase in copper content in cells following 24 h treatment irrespective of whether we use sulfur or phosphorus to normalize data (Figures 1D, 2B, and 2C). It is important to emphasize that expected outcomes of copper cellular content were achieved when cells were incubated with copper or the copper chelator BCS (Figures 2B and 2C). The effect of these additions to cultured cells was selective for copper without affecting other metals (Figure 2C). Further, this protocol can be easily adapted for new purposes, including metal quantification in specific cellular compartments. For example, we have used it to quantify metals in fractions enriched in mitochondria. Metal quantification can also be performed in single cells by infusing the cell suspension into the instrument, although some other modifications are required for single cell analysis. Alternatively, we can calculate the metal content per cell from analyses

such as those presented in Figures 1 and 2. For example, we estimate a cellular content of 4.7 fentograms of copper per cell (Table 4). This is in the range of what has been previously determined in a single yeast cell (2 fentograms/mammalian nucleated cell equivalent) or red blood cell (6 fentograms/ mammalian nucleated cell equivalent) after adjusting by nucleated cell volume. We used a HeLa cell volume of ~3,000 cubic microns to normalize other cell volume values (Puck et al., 1956; Rae et al., 1999; Cao et al., 2020).

2.7 Limitations

This method is broadly applicable to all samples of biological origin. However, normalization based on sulfur content cannot be done if buffers and detergents containing sulfur are used. Commonly used sulfur containing compounds used in biological research include, dithiothreitol, sodium dodecyl sulfate (SDS), HEPES (4-(2-hydroxyethyl)-1-piperazineethanesulfonic acid) buffer and ammonium sulfate. Similarly, if phosphorus is used for data normalization then the use of phosphate-based buffer saline solutions should be replaced with saline buffered with sulfur- and phosphate-free buffers such as TRIS (Tris(Hydroxymethyl)aminomethane). There may also be limitations with the measurement of ultra-trace elements like Co where potential imprecision at the sub 1ppb level requires a larger number of cells than would be needed for Fe, Cu and Zn (see Figure 1G). In both larval and cell counts above ~500,000, there is a better linear response for Co (Figure 1G).

2.8 Troubleshooting

2.8.1 Problem 1

The sample is not breaking down in 70% nitric acid (step 36).

Potential solution

Start with 20 µL of 70% nitric acid per sample. If the sample does not dissolve, add more acid and return samples to the heat block for another 10 min. Inspect tube for particulates and repeat as

necessary. (Example: We prepared samples with 3 million HAP1 cells, not shown here. These samples dissolved once we added 100 µL of acid).

Samples with large amounts of lipids (such as brain tissue) may need to be further broken down with hydrogen peroxide. In this case, hydrogen peroxide (analytical grade) should be added 1:1 with the volume of 70% nitric acid. Incubate at 95°C for 10 min. In addition, some samples (e.g., tissue) may require homogenization. In this case, samples can be homogenized by manual Dounce or sonication for 5 min using Tris buffered saline (50 mM Tris pH 8.0, 150 mM sodium chloride + EDTA free protease inhibitors; avoid buffers with detergents). Clarify homogenates by centrifugation at 16,000 × *g* for 5 min. Collect the resulting supernatant and keep samples at 4°C. (Note: All samples must be centrifuged prior to loading into the deep well plate.) See Hare et al. (2013); Ganio et al. (2016); Lothian and Roberts (2016); McAllum et al. (2020).

2.8.2 Problem 2

Blanks produce background noise (step 45).

Potential solution

It is important to use only analytical grade chemicals, materials, and reagents that have minimal levels of trace metals. We highly recommend conducting preparation blanks (see the Prepare buffers for ICP-MS section for more information) before doing any biological experiments to validate that the buffers, solvents, and plasticware being used are not contaminated. Similarly, all bottles and beakers used should be rinsed with MilliQ water. If you need to lyse your sample, you can use RIPA buffer (0.5% Nonidet P-40, 50 mM Tris pH 8, 0.5% sodium deoxycholate, 2 mM EDTA, 150 mM NaCl). Triton X and tween are also acceptable detergents to use.

2.8.3 Problem 3

Measurements for one or more metals are below detection limits (step 46).

Potential solution

Usually the lower abundant elements (including Cu, Co, and Mn) are the limiting factors in dilution of the sample. To better detect these metals, increase the number of cells/larvae in each sample. You can also treat with a solution containing the metal if desired (see step 1).

2.8.4 Problem 4

Variation is seen in sulfur or phosphorus content between replicates (step 46).

Potential solution

It is possible that different amounts of each sample were loaded into the ICP-MS. This could arise due to the accuracy of the cell counting method and preparation of cell samples (i.e., loading different numbers of cells) or differing larval weights across replicates. If sulfur or phosphorus content for each replicate is only slightly variable and is well correlated with other metals, no additional action needs to be taken, though additional attention can be directed toward preparing samples with precision.

If needed, additional methods can be used to normalize metal content. For example, you can normalize to total protein. This requires you to measure protein after either preparing samples in RIPA buffer and sonicating as described above. For flies, you can normalize to fly weight rather than fly number and/or pool larvae to prepare samples of similar weights.

It is possible that some conditions may affect sulfur or phosphorus content (such as treatment with BCS in Figure 2A). Figure 2A clearly illustrates the benefit of quantifying both sulfur and phosphorus and using both as normalization factors, as BCS-treated cells have increased levels of sulfur per cells but phosphorus remains unchanged.

2.8.5 Problem 5

The liquid evaporates from samples stored in 70% nitric acid (step 36).

Potential solution

When samples are stored for an extended period of time, it is not uncommon to have complete evaporation of the small amount of nitric present. You can avoid this by adding 70% nitric acid to your samples and running them in the same week. If samples have been stored long-term and some or all of the acid has evaporated, bring each sample to 800 µL with 2% nitric acid. When absolute concentration beyond 1%–2% accuracy is required, we suggest fully drying the samples in the heat block and resuspending with 800 µL of 2% nitric acid. Alternatively, you can estimate the volume remaining using a p20 pipette and bring the volume of each sample to 800 µL or simply add 800 µL 2% nitric acid to each sample. The important variable is to treat all the samples the same. (The error in having 5 µL vs 20 µL when diluting to a total volume of 800 µL is less than 1.5%, which does not significantly impact the experiment due to the large biological variation observed).

2.9 Resource availability

Lead contact

Further information and requests for resources and reagents should be directed to and will be fulfilled by the lead contacts, Blaine Roberts (blaine.roberts@emory.edu) and Victor Faundez (vfaunde@emory.edu).

Materials availability

This study did not generate new unique reagents.

2.10 Acknowledgments

This work was funded by NIH grants 1RF1AG060285 and RF1AG060285-01A1S1 (V.F.).

Author contributions

Conceptualization, V.F., B.R., and A.L.; Methodology, B.R. and A.L.; Validation, B.R.; Formal Analysis, V.F.; Investigation, A.G., A.F., A.L, A.R., E.W., and B.R.; Resources, V.F. and B.R.;

Writing – Original Draft, V.F., A.G., A.F., A.L, and B.R.; Writing – Review & Editing, V.F., A.L., and B.R.; Visualization, V.F. and A.L.; Supervision, V.F. and B.R.; Funding Acquisition, V.F.

Declaration of interests

The authors declare no competing interests.

Institutional permissions

No institutional permissions were necessary for these experiments. If adapting this protocol for use in vertebrates or higher invertebrates, acquire permissions from the relevant institution(s) and ensure that all experiments are performed in accordance with relevant institutional and national guidelines and regulations.

2.11 Contributor Information

Blaine Roberts, Email: blaine.roberts@emory.edu.

Victor Faundez, Email: vfaunde@emory.edu.

2.11.1 Data and code availability

The study did not generate any unique datasets or code.

Chapter 3. Adaptive protein synthesis in genetic models of copper deficiency and childhood neurodegeneration

Alicia R. Lane[1], Noah E. Scher[1*], Shatabdi Bhattacharjee[2*], Stephanie A. Zlatic[1], Anne M. Roberts[3,4], Avanti Gokhale[1], Kaela S. Singleton[1], Duc M. Duong[3], Mike McKenna[5], William L. Liu[6], Alina Baiju[6], Felix G Rivera Moctezuma[7], Tommy Tran[2], Atit A. Patel[2], Lauren B. Clayton[9], Michael J. Petris[8], Levi B. Wood[7], Anupam Patgiri[6], Alysia D. Vrailas-Mortimer[9], Daniel N. Cox[2], Blaine R. Roberts[3,4], Erica Werner[1#], Victor Faundez[1#]

[*]These authors contributed equally
[#]Co-corresponding author

[1]Department of Cell Biology, Emory University, Atlanta, Georgia, USA, 30322
[2]Neuroscience Institute, Georgia State University, Atlanta, GA 30303
[3]Department of Biochemistry, Emory University, Atlanta, Georgia, USA, 30322
[4]Department of Neurology, Emory University, Atlanta, Georgia, USA, 30322
[5]NanoString Technologies, 530 Fairview Ave N, Seattle, WA 98109
[6]Department of Pharmacology and Chemical Biology, Emory University, Atlanta, Georgia, USA, 30322
[7]George W. Woodruff School of Mechanical Engineering and Parker H. Petit Institute for Bioengineering and Bioscience, Georgia Institute of Technology, Atlanta, GA 30332
[8]Departments of Biochemistry, Molecular Microbiology and Immunology, Ophthalmology, and Christopher S. Bond Life Sciences Center, University of Missouri, Columbia, MO, 65211
[9]Department of Biochemistry & Biophysics and Linus Pauling Institute, Oregon State University, Corvallis, OR 97331

This chapter is published in *Mol Biol Cell*. 2025 Mar 1;36(3):ar33. doi: 10.1091/mbc.E24-11-0512. Epub 2025 Jan 29 and licensed under CC-BY-NC 4.0.

3.1 Abstract

Rare inherited diseases caused by mutations in the copper transporters *SLC31A1* (CTR1) or *ATP7A* induce copper deficiency in the brain, causing seizures and neurodegeneration in infancy through poorly understood mechanisms. Here, we used multiple model systems to characterize the molecular mechanisms by which neuronal cells respond to copper deficiency. Targeted deletion of CTR1 in neuroblastoma cells produced copper deficiency that was associated with a metabolic shift favoring glycolysis over oxidative phosphorylation. Proteomic and transcriptomic analysis of CTR1 KO cells revealed simultaneous upregulation of mTORC1 and S6K signaling and reduced PERK signaling. Patterns of gene and protein expression and pharmacogenomics show increased activation of the mTORC1-S6K pathway as a pro-survival mechanism, ultimately resulting in increased protein synthesis. Spatial transcriptomic profiling of *Atp7a*$^{flx/Y}$ *:: Vil1*$^{Cre/+}$ mice identified upregulated protein synthesis machinery and mTORC1-S6K pathway genes in copper-deficient Purkinje neurons in the cerebellum. Genetic epistasis experiments in *Drosophila* demonstrated that copper deficiency dendritic phenotypes in class IV neurons are partially rescued by increased S6k expression or 4E-BP1 (Thor) RNAi, while epidermis phenotypes are exacerbated by Akt, S6k, or raptor RNAi. Overall, we demonstrate that increased mTORC1-S6K pathway activation and protein synthesis is an adaptive mechanism by which neuronal cells respond to copper deficiency.

3.2 Introduction

Copper is an essential micronutrient but can be toxic if not regulated appropriately (Zlatic et al., 2015; Lutsenko et al., 2024). Neurodevelopment has stringent temporal and spatial requirements for copper levels and localization within organelles and across tissues, and a failure of mechanisms controlling copper homeostasis is causative of or associated with a variety of neurodevelopmental and neurodegenerative diseases (Waggoner et al., 1999; Opazo et al., 2014a). Defects in copper homeostasis are linked to dysfunctional neuronal differentiation, organization, migration, and arborization; axonal outgrowth; synaptogenesis; and neurotransmission in multiple brain regions (Purpura et al., 1976; Hirano et al., 1977; Büchler et al., 2003; Niciu et al., 2006; El Meskini et al., 2007; Scheiber et al., 2014; Zlatic et al., 2015).

As copper is a redox active metal required for oxidative phosphorylation, it is tightly linked to bioenergetics (Garza et al., 2022b). Thus, tissues with high energy demands, like the brain, are particularly susceptible to copper toxicity and deficiency (Scheiber et al., 2014). Neurodevelopment is a particularly vulnerable time due to the high energy consumption and transitions in metabolism by the brain during this period (Bülow et al., 2022) and the increased neuronal demand for copper after differentiation (Hatori et al., 2016). While the fetal brain produces energy by glycolysis, after birth there is an increase in brain consumption of glucose and oxygen that peaks in humans at age 5, nearly doubling the consumption of the adult brain (Goyal et al., 2014; Kuzawa et al., 2014; Steiner, 2020; Oyarzábal et al., 2021). This transition from glycolysis to oxidative phosphorylation is in part cell-autonomous, as it is also observed in differentiating neurons and muscle cells in culture (Vest et al., 2018; Iwata et al., 2023; Casimir et al., 2024; Rajan and Fame, 2024), and is necessary for neurodevelopment (Zheng et al., 2016; Sakai et al., 2023; Casimir et al., 2024; Iwata and Vanderhaeghen, 2024). In fact, aberrant hyperglycolytic metabolism in neurons induces dysfunction and damage in vitro and in vivo (Jimenez-Blasco et al., 2024).

Mutations affecting copper homeostasis provide an opportunity to understand how copper-dependent mechanisms and metabolism interact to drive brain development. For example, mutations affecting the copper transporter ATP7A cause conditions of varying severity and age of onset but which all present with prominent neurological symptoms (OMIM: 309400, 304150, 300489; Kaler, 2011). In its most severe form, Menkes disease, overt neurological symptoms and neurodegeneration appear between 1-3 months of age (Menkes et al., 1962; Tümer and Møller, 2010; Kaler, 2011; Skjørringe et al., 2017). Similarly, most Menkes mouse models exhibit substantial neurodegeneration by postnatal days 10 to 14, typically culminating in death by day 21 (Yajima and Suzuki, 1979; Iwase et al., 1996; Donsante et al., 2011; Kaler, 2011; Lenartowicz et al., 2015; Guthrie et al., 2020; Yuan et al., 2022). Whether this delay in disease appearance is impacted by increasing neurodevelopmental demands for copper and/or neurodevelopmental-sensitive mechanisms conferring resilience to copper depletion has not been considered.

Here, we sought to identify cell-autonomous mechanisms in neurons downstream of copper deficiency. We generated *SLC31A1*-null cells that lack the ability to import copper through the plasma membrane copper transporter CTR1. *SLC31A1* genetic defects (OMIM: 620306) cause symptoms similar to Menkes disease (Batzios et al., 2022; Dame et al., 2022). We discovered that these copper-deficient cells exhibit impaired mitochondrial respiration concurrent with increased glycolysis. Using multiomics approaches, we discovered the modification of two distinct pathways involved in regulation of protein synthesis in CTR1 KO cells: increased mTORC1 signaling pathway activation and reduced activity of EIF2AK3 (PERK, eukaryotic translation initiation factor 2 alpha kinase 3). Accordingly, CTR1-null cells had increased protein synthesis as measured by puromycin incorporation. Similarly, copper-deficient *Atp7a*$^{flx/Y}$ *:: Vil1*$^{Cre/+}$ mice upregulate protein synthesis machinery and mTOR pathway transcripts. Based on our pharmacogenomics in cells and genetic epistasis experiments in *Drosophila*, which demonstrate a partial rescue of dendritic phenotypes by S6k overexpression or Thor RNAi, we conclude that

mTOR activation and upregulation of protein synthesis is an adaptive mechanism engaged in response to copper deficiency.

3.3 Results

3.3.1 Metabolic phenotypes in a cell-autonomous model of copper deficiency

To establish a cell-autonomous model of copper deficiency, we generated *SLC31A1* null (hereafter referred to as CTR1 KO) SH-SY5Y clonal cells by CRISPR genome editing (Supplemental Figure S1). *SLC31A1* encodes the copper importer CTR1, for which protein expression was abolished after CRISPR genome editing (Figure 1A and Supplemental Figure S1A). CTR1 KO clones were characterized by their increased resistance to copper (Supplemental Figure S1B) and reduced abundance of the copper-dependent Golgi enzyme dopamine-β-hydroxylase (DBH, Figure 1A). We confirmed that relative to wild type cells, whole CTR1 KO cells were selectively depleted of copper but not zinc as measured by inductively-coupled mass spectrometry (ICP-MS) (Wilschefski and Baxter, 2019; Lane et al., 2022) (Figure 1B and Supplemental Figure S1D). Mitochondrial-enriched fractions were also selectively depleted of copper but not zinc in CTR1 KO cells (Figure 1B and Supplemental Figure S1D). These whole cell and mitochondrial copper phenotypes were rescued by a non-toxic dose of elesclomol (Figure 1B and Supplemental Figure S1C), a small molecule that delivers copper preferentially to the mitochondria (Kirshner et al., 2008; Wu et al., 2011; Blackman et al., 2012; Soma et al., 2018; Garza et al., 2022a). As copper is essential for the assembly and function of the electron transport chain, particularly Complex IV, we chose to examine the levels of subunits of respiratory chain complexes as well as assembly of supercomplexes. The protein abundance of the copper-dependent mitochondrial Complex IV in CTR1 KO cells was 55% of wild-type levels, while there was no decrease in levels of the other respiratory complexes (Figure 1C). Using blue native gel electrophoresis with digitonin to preserve supercomplexes, we demonstrated Complex I, III, and

IV organization into complexes was compromised in CTR1 KO cells, with more pronounced changes in Complex III and IV. We did not detect modifications of Complex II (Figure 1D).

To examine the function of the electron transport chain in CTR1 KO cells, we performed Seahorse oximetry using the Mito Stress Test. Consistent with their reduced levels and impaired assembly of Complex IV, CTR1 KO cells exhibited decreased basal and ATP-dependent respiration (0.53x and 0.54x wild-type levels, respectively; Figure 1, E and F, compare columns 1 and 2). These differences attributable to copper deficiency in CTR1 KO cells since they were magnified by treatment with the cell-impermeant copper chelator BCS (Figure 1F, compare columns 2 and 8), while BCS had no effect on wild-type cells under these conditions (Figure 1F, compare columns 1 and 7). Copper delivery via elesclomol treatment at a low, non-toxic concentration rescued the respiration defects and increased media acidification (suggesting increased glycolysis) in CTR1 KO cells back to wild type levels (Figure 1F, compare columns 1, 2, and 4; Supplemental Figure S1, C and E). BCS suppressed the elesclomol-mediated rescue of respiration and acidification phenotypes in CTR1 KO cells (Figure 1F, compare columns 4 and 6; Supplemental Figure S1E), confirming the requirement for copper in this rescue (Supplemental Figure S1E). There was no difference in maximal respiration in untreated cells or in response to BCS or elesclomol (Figure 1F). The increased media acidification by CTR1 KO cells suggests increased glycolysis as compared to wild type cells (Supplemental Figure S1E). To characterize the glycolytic parameters of CTR1 KO cells, we used the Glycolysis Stress Test. CTR1 KO cells exhibited elevated extracellular acidification rate, with increased glycolysis (2.03x wild-type levels), increased glycolytic capacity (1.18x wild-type levels), and reduced glycolytic reserve (0.20x wild-type levels) as compared to wild-type cells (Figure 1G). CTR1 KO respiration and glycolysis phenotypes correlated with modifications in energy charge (Supplemental Figure S1F) (Atkinson and Walton, 1967) and lactate levels (Supplemental Figure S1G), which were fully or partially restored by elesclomol (Supplemental Figure S1). Together, these findings demonstrate that CTR1 KO cells have compromised copper-dependent Golgi and mitochondrial enzymes. The

impairment of the function and organization of the respiratory chain in CTR1 KO cells induces a metabolic shift favoring glycolysis over oxidative phosphorylation.

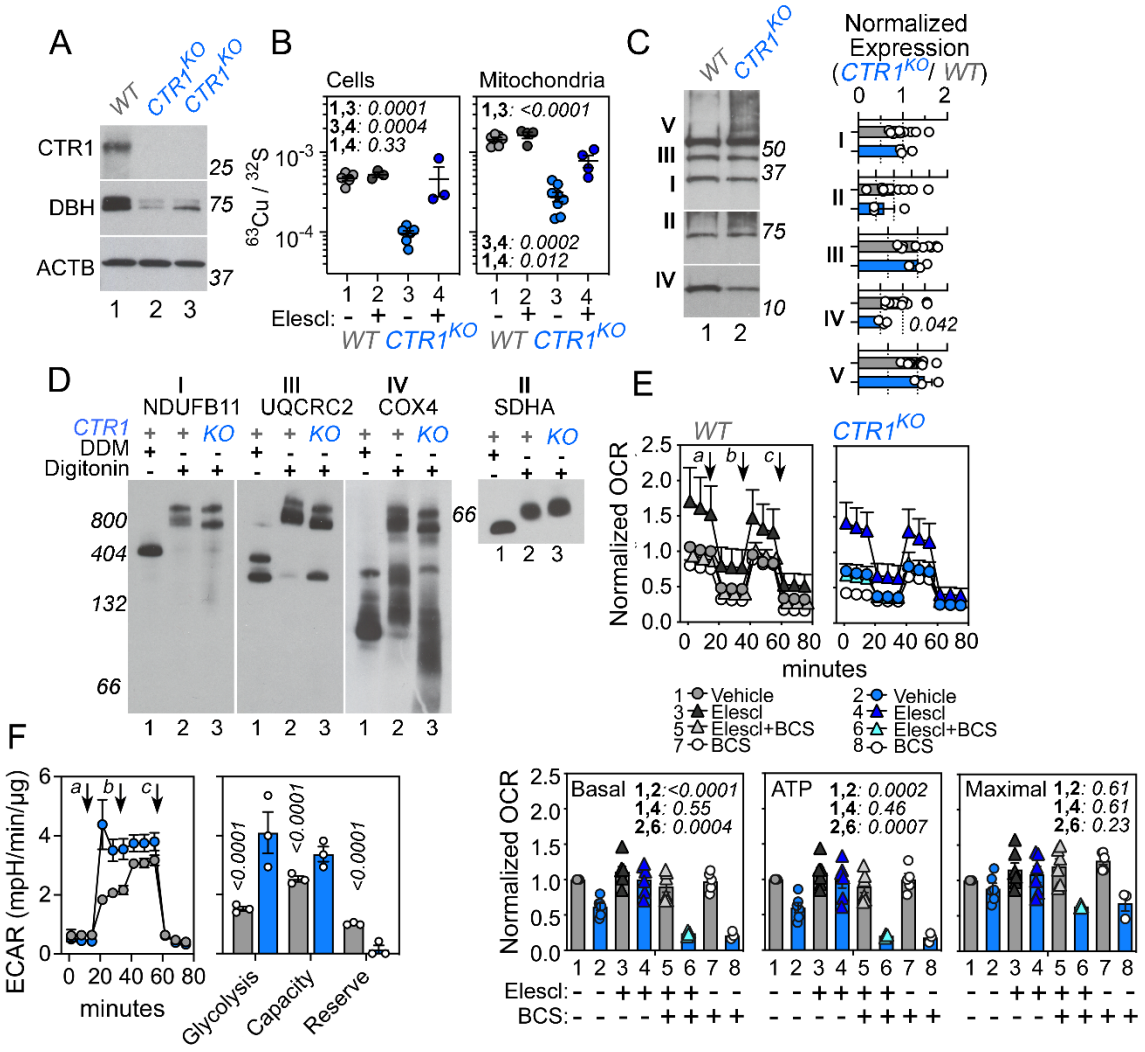

Figure 1. CTR1 (*SLC31A1*) null mutation disrupts electron transport chain assembly and function and increases glycolysis.

A. Immunoblot of cellular extracts from wild-type (lane 1) and two independent *SLC31A1Δ/Δ* mutant (CTR1 KO, lanes 2-3) SH-SY5Y cell clones probed for CTR1 and DBH with beta-actin as a loading control. **B**. 63Cu quantification in whole cells or mitochondria in CTR1 KO cells treated with vehicle or 1 nM elesclomol, normalized to 32S. Italicized numbers represent q values (One-Way ANOVA, followed by Benjamini, Krieger, and Yekutieli multiple comparisons correction). **C**. Immunoblot with OxPhos antibody mix in mitochondrial fractions from wild-type and CTR1 KO cells. Complex II was

used as a loading control as it does not form respiratory supercomplexes (Iverson et al., 2023). (Each dot is an independent biological replicate. Italicized numbers represent p values analyzed by two-sided permutation t-test.) **D**. Blue native electrophoresis of mitochondrial fractions from wild-type and CTR1 KO cells (Clone KO3) solubilized in either DDM or digitonin to dissolve or preserve supercomplexes, respectively (Wittig et al., 2006; Timón-Gómez et al., 2020). Shown are native gel immunoblots probed with antibodies against Complex, I, II, III, and IV. Italicized numbers represent p values. Complex II was used as a loading control. Immunoblots were also prepared with CTR1 clone KO20 (not shown). **E-G**. Seahorse stress tests in wild-type and CTR1 KO cells. Arrows indicate the sequential addition of oligomycin (a), FCCP (b), and rotenone-antimycin (c) in the Mito Stress Test (E) to cells treated with vehicle, 1 nM elesclomol, or 200 μM BCS for 72 hours (E, F, BCS n =3, all other treatments n=6-7) or the addition of glucose (a), oligomycin (b), and 2-Deoxy-D-glucose (c) in the Glycolysis Stress Test (G, n=3). Basal cellular respiration and glycolysis were measured for 90 min after additions using Seahorse. **E,F**. Mito Stress Test data are presented normalized to basal respiration of wild-type cells in the absence of drug, analyzed by a One-Way ANOVA followed by Benjamini, Krieger, and Yekutieli multiple comparisons correction (italics show q values). CTR1 clone KO20 was used. **G**. Glycolysis Stress Test data are presented normalized to protein, analyzed by two-sided permutation t-test (italicized numbers represent p values). All data are presented as average ± SEM.

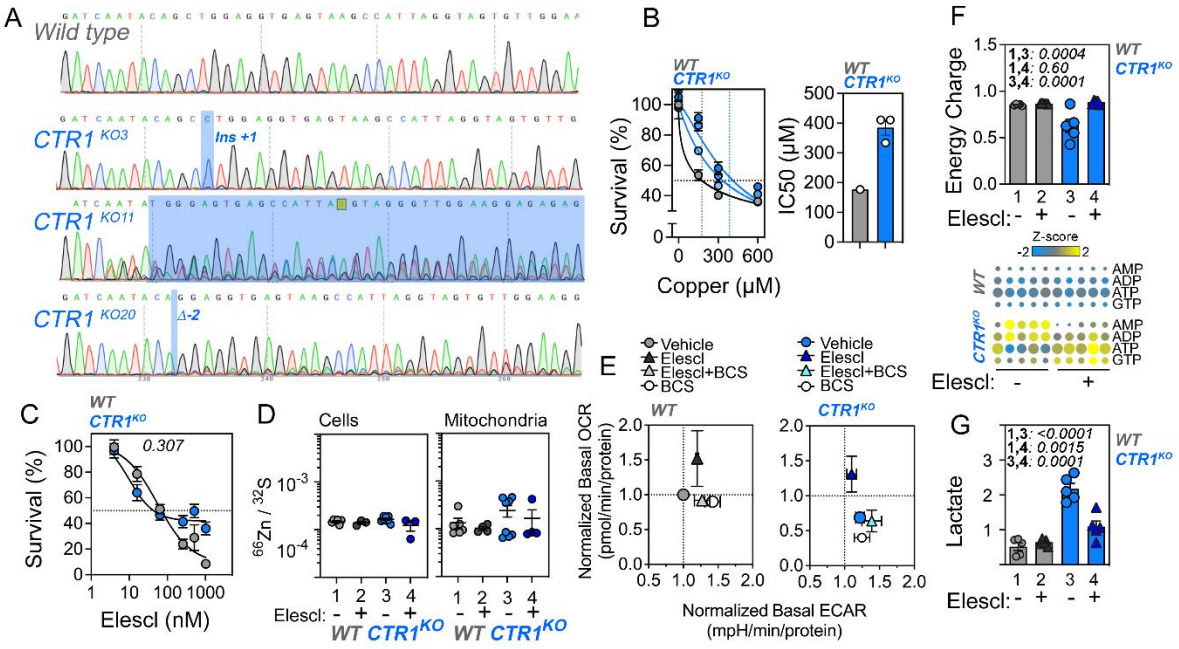

Figure S1. Generation and characterization of CTR1 (*SLC31A1*)-null mutant neuroblastoma cells.

A. DNA sequence chromatograms of one wild type and three *SLC31A1* CRISPR-edited SH-SY5Y clonal lines. Blue boxes mark the mutated sequence. **B**. Cell survival analysis of *SLC31A1* mutants with increasing concentrations of copper. Blue shaded symbols represent three different clones (n=3 replicates for 1 or 3 clones for wild type or *SLC31A1* mutants respectively). IC50 was calculated by fitting data to a non-linear model using Prism. **C**. Cell survival analysis of wild type and CTR1 mutants with increasing concentrations of elesclomol (n = 11 and 14, p value Sum-of-squares F test analysis). **D**. 64Zn quantification in whole cells or mitochondria in CTR1 KO cells treated with vehicle or 1 nM elesclomol, normalized to 32S. There are no significant differences by treatment or genotype as assessed by One-Way ANOVA, followed by Benjamini, Krieger, and Yekutieli multiple comparisons correction. **E**. Metabolic map of basal OCR and ECAR from the Mito Stress Test of wild-type and CTR1 KO cells (clone KO20) normalized to untreated wild-type cells treated with vehicle, elesclomol, or BCS as described in Figure 1. **F-G**. Mass spectrometry quantification of metabolites, analyzed by One-Way ANOVA followed by Benjamini, Krieger, and Yekutieli multiple comparisons correction. CTR1 clone KO20 was used. **G**. Quantification of energy charge, calculated by dividing the amount of [ATP] + 0.5[ADP] by the total levels of [ATP]+[ADP]+[AMP] (Atkinson and Walton, 1967). Heat

maps show the levels of the adenylate nucleotides used for the calculation and GTP for comparison. G. Quantification of lactate levels. All data are presented as average ± SEM.

3.3.2 Unbiased discovery of copper deficiency mechanisms using proteomics and NanoString transcriptomics

Next, we sought to comprehensively identify pathways and signal transduction mechanisms altered by CTR1 KO copper deficiency. We performed quantitative mass spectrometry of the whole cell and phosphorylated proteomes by Tandem Mass Tagging (Figure 2, source data in Supplemental Data File 1), focusing on the phosphoproteome as multiple kinases are known to have copper-binding domains which regulate their activity (Brady et al., 2014; Tsang et al., 2020). We quantified 8,986 proteins and 19,082 phosphopeptides (from 4066 proteins) across wild type cells and two CTR1 KO clones (Figure 2A volcano plot, Supplemental Data File 1). The proteome and phosphoproteome did not segregate by genotype in principal component analysis until after thresholding data ($p<0.01$, fold change ≥ 1.5; Figure 2B, PCA). This indicates discrete modifications of the global proteome and phosphoproteome in CTR1 KO cells. We identified 210 proteins and 224 phosphopeptides (from 162 proteins) that exhibited differential abundance in CTR1 KO cells ($p<0.01$, fold change ≥ 1.5, source data in Supplemental Data File 1), of which 26 proteins differed in both abundance and phosphorylation. 153 proteins and 138 phosphopeptides were more abundant while 57 proteins and 86 phosphopeptides decreased in abundance in CTR1 KO cells as compared to wildtype, respectively.

As further confirmation of Complex IV impairments and metabolic dysfunction in CTR1 KO cells (Figure 1, source data in Supplemental Figure S1), we used a replication TMT proteome (TMT2) to quantify Complex IV subunits and chaperones. Overall, we identified 184 differentially expressed proteins in CTR1 KO cells (Figure 2C, Venn diagram, TMT2). These two proteome datasets overlapped 9.1 times above what is expected by chance ($p=6.7E-12$, hypergeometric probability). Both datasets are enriched 11-fold in a protein interaction network annotated to the GO term generation of precursor metabolites and energy (GO:0006091, $p=1E-31$, hypergeometric probability; Figure 2C, Venn diagram and interactome, Supplemental Data File

1). This network of proteins included 9 proteins belonging to Complex IV, such as MT-CO1, MT-CO2, and MT-CO3, all of which were decreased in CTR1 KO cells ≥ 1.5-fold ($p<0.01$; Figure 2D, Complex IV subunits, upper heat map; Supplemental Data File 1). This finding is consistent with the reduction of Complex IV subunits and supercomplexes by immunoblot and reduced respiration in CTR1 KO cells (Figure 1, C–F). This protein network also included seven Complex IV assembly factor and copper chaperones, such as COX17, whose levels were increased in CTR1 KO cells ≥ 1.5-fold ($p<0.01$; Figure 2D, Complex IV assembly factors, bottom heat map). Overall, this suggests copper-deficient cells upregulate assembly factors and chaperones for Complex IV in response to impaired assembly of this respiratory complex.

To identify ontological terms represented in the integrated CTR1 KO proteome and phosphoproteome (consisting of 345 total proteins with differential abundance and/or phosphorylation, source data in Supplemental Data File 1, TMT1), we queried the NCAST Bioplanet discovery resource with the ENRICHR tool and multiple databases with the Metascape tool (Huang et al., 2019). Both bioinformatic approaches identified the mTOR signaling pathway (ENRICHR q=4.76E-3 and Metascape q=9.8E-5), S6K1 signaling (ENRICHR q=1.4E-3), and Rho GTPase cycle in the top enriched terms (Figure 2E, gene ontology, Supplemental Data File 1). Metascape analysis merged the CTR1 proteome and phosphoproteome into a network of 16 protein-protein interactions annotated to mTORC1-mediated signaling, which include these proteins: EIF4G1, mTOR, RPTOR (Raptor), AKT1S1, DEPTOR, RPS6, and RPS6KA6 (R-HSA-166208 and KEGG hsa04150, q=1.25E-9, z-score 22; Figure 2F, mTORC1 and Figure 2G, pathway diagram). As only 6 protein-protein interactions annotated to the Rho GTPase cycle (Figure 2, E and F, compare odds ratios), we focused on the mTOR-S6K pathway.

The most pronounced changes in the steady state mTOR proteome encompassed decreased levels of DEPTOR and increased levels of Ribosomal Protein S6 Kinase A6 (RPS6KA6 or RSK4) (Figure 2H). DEPTOR is an mTOR inhibitor (Peterson et al., 2009), and

RPS6KA6 is a member of the ribosomal S6K (RSK) family. RSK proteins (RSK1-RSK4) are activated downstream of MEK/ERK signaling, while the S6K family (S6K1 and S6K2) is phosphorylated by mTOR, but both families regulate translation through phosphorylation of ribosomal protein S6 (RPS6) and other related proteins (Meyuhas, 2015; Wright and Lannigan, 2023). These changes in abundance of DEPTOR and RPS6KA6 suggest heightened mTOR activity and RPS6 activation in copper deficiency. In support of this idea, CTR1 KO cells have increased phosphorylation of mTOR, RPS6, EIF4G1 (eukaryotic translation initiation factor 4 gamma 1), ACLY (ATP-citrate synthase), and UVRAG (UV radiation resistance associated) without changes in their steady state levels (Figure 2H). The increased phosphorylation of these proteins was in phosphoresidues known to be responsive to mTOR activity, which include: mTOR S1261 and S2448, both correlated with increased mTOR activity and targets for the insulin/phosphatidylinositol 3–kinase (PI3K) pathway and the latter a target of RPS6KB1 (Ribosomal Protein S6 Kinase B1 or S6K1) (Chiang and Abraham, 2005; Holz and Blenis, 2005; Acosta-Jaquez et al., 2009; Copp et al., 2009; Rosner et al., 2010; Smolen et al., 2023); EIF4G1 S984 (Raught et al., 2000); RPS6 S235, S236, and S240, which are targets of S6K1 and RSK4 (Holz and Blenis, 2005; Roux et al., 2007; Magnuson et al., 2012; Meyuhas, 2015); and ACLY and UVRAG at S445 and S458, respectively (Kim et al., 2015; Covarrubias et al., 2016; Martinez Calejman et al., 2020). Increased phosphorylation of mTOR at S2448 and P70S6K at T389 was confirmed by immunoblot (Figure 3C). We also observed increased protein expression and phosphorylation of AKT1S1 (PRAS40) at T246, a residue that is a target of AKT1 and whose phosphorylation correlates with active mTOR (Figure 2H) (Sancak et al., 2007). Importantly, we identified increased phosphorylation of RPTOR (Raptor, regulatory-associated protein of mTOR) at the RSK4 target residue S722 (Meyuhas, 2015) but observed no changes in RICTOR (RPTOR-independent companion of MTOR complex 2), suggesting that mTORC1 but not mTORC2 signaling is impacted (Ma and Blenis, 2009). Beyond the mTOR-S6K pathway, the proteome also revealed decreased protein levels of EIF2AK3 (PERK, eukaryotic translation initiation factor 2

alpha kinase 3), an ER stress response kinase and negative regulator of protein synthesis (Almeida et al., 2022), which was confirmed by immunoblot (Figure 3C) and paralleled reduced content of two of its phosphopeptides (Figure 2H, S551 and S555). While not known to be a direct target of mTOR, EIF2AK3 activity decreases by an AKT1-dependent mechanism (Peng et al., 2020). We conclude that genetic defects in CTR1 KO cells modify the proteome and signaling pathways converging on mTOR- and PERK-dependent signaling mechanisms upstream of protein synthesis pathways (Mounir et al., 2011; Hughes et al., 2020).

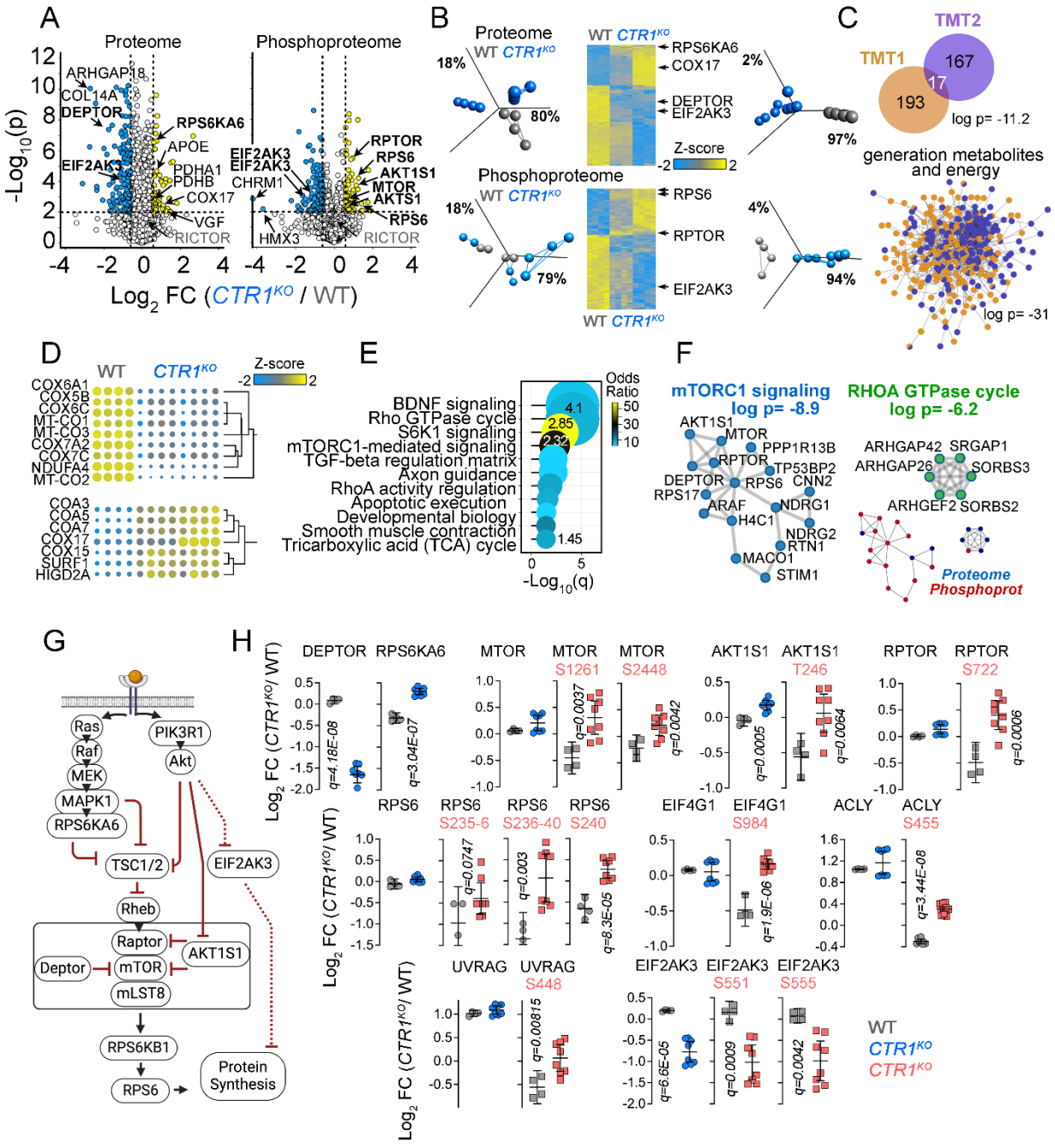

Figure 2. CTR1 mutant proteome and phosphoproteome have increased activation of mTOR-Raptor-S6K signaling and protein synthesis pathways.

A. Volcano plots of the CTR1 KO cell proteome and phosphoproteome (TMT1), where yellow dots represent proteins or phosphoproteins whose expression is increased in KO cells and blue dots represent decreased expression in KO cells. n=4 for wild type cells and n=4 for KO cells in two independent clones (KO3 and KO11). **B**. Principle component analysis (PCA) of the whole proteome

and phosphoproteome from wild type (gray) and two CTR1 KO clonal lines (blue symbols). Hierarchical clustering and PCA of all proteome or phosphoproteome hits where differential expression is significant with q<0.05 and a fold of change of 1.5 (t-test followed by Benjamini-Hochberg FDR correction). **C**. Replication TMT Proteome (TMT2) in independent CTR1 KO clone experiment (KO3 and KO20), Venn diagram overlap p value calculated with a hypergeometric test. Merged protein-protein interaction network of both TMT experiments is enriched in the GO term GO:0006091 generation of precursor metabolites and energy. **D**. TMT proteome levels of Complex IV subunits and assembly factors expressed as Z-score from TMT2. All 16 proteins changed more than 1.5-fold as compared to wild type cells with a q<0.05. **E**. Gene ontology analysis of differentially expressed proteins or phosphopeptides in CTR1 mutant proteome and phosphoproteome (TMT1). The Bioplanet database was queried with the ENRICHR engine. Fisher exact test followed by Benjamini-Hochberg correction. **F**. Metascape analysis of the proteome and phosphoproteome (TMT1). Ontology enrichment analysis was applied to a protein-protein interaction network of all components to select molecular complexes with MCODE based on significant ontologies. **G**. mTOR signaling pathway diagram modified from KEGG map04150. **H**. Mass spectrometry quantification of ontologically selected proteins and phosphopeptides (TMT1). Proteins are shown with blue circles and phosphopeptides are shown with red squares. Vertical numbers represent q values. See Supplemental Data File 1 for source data.

We used NanoString nCounter transcriptomics as an orthogonal approach to proteomics to identify molecular mechanisms downstream of CTR1 KO-dependent copper deficiency. We examined steady-state mRNA levels using NanoString panels enriched in genes annotated to metabolic pathways and neuropathology processes, which collectively measure levels of over 1400 transcripts (Supplemental Figure S2 and Supplemental Data File 1), including 66 genes annotated to the mTOR pathway (KEGG). We identified 131 metabolic and 37 neuropathology annotated transcripts whose levels were altered in CTR1 KO cells (q<0.05 and fold of change ≥2, Supplemental Figure S2, A–C; Supplemental Data File 1). Metabolic transcripts were enriched in genes annotated to lysosome and mTOR signaling (KEGG, p<5.8E-6 and z-score >18; Supplemental Figure S2D; Supplemental Data File 1). Similar ontology analysis but with the

combined 168 transcripts whose levels were altered in CTR1 KO cells was enriched in genes annotated to central carbon metabolism in cancer and the PI3K-Akt signaling pathway (p=2.3E-11 z-score 8.8. and p=1.78E-6 and z-score 9.6; Supplemental Data File 1). With the exception of DEPTOR, a negative regulator of mTOR, 14 of the 15 transcripts annotated to mTOR and PI3K-Akt signaling were increased in CTR1 KO cells (Supplemental Figure S2C). The copper dependency of these transcripts level changes was demonstrated using the copper chelator BCS. Differences in gene expression between wild type and CTR1 KO cells at baseline were magnified by BCS (Supplemental Figure S2, A and B; Supplemental Data File 1). A subset of these genes was sensitive to copper chelation in both wild-type and CTR1 KO cells, including PIK3R1, SLC7A5, and SLC3A2 (Supplemental Figure S2B).

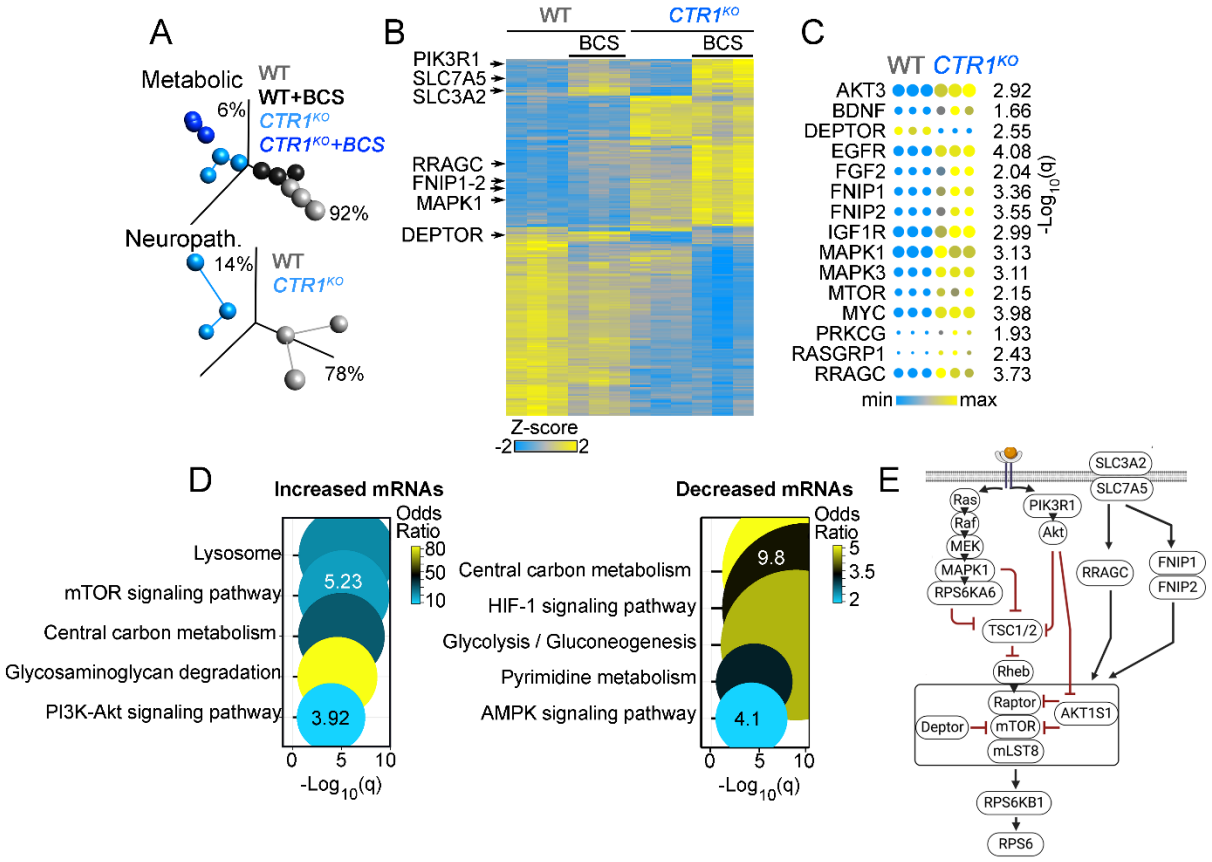

Figure S2. Transcript changes in CTR1 mutants reflect increased activation of the mTOR and PI3K-Akt signaling pathways.

A. Principal component analysis of the Metabolic and Neuropathology annotated transcriptomes from wild type (gray) or CTR1 KO (blue symbols; KO20) clonal lines in the absence or presence of BCS (200 μM, 72 hours). **B.** Hierarchical clustering of the metabolism annotated transcriptome differentially expressed at a significancy of q<0.05 (analyzed by one-way ANOVA followed by Benjamini-Hochberg FDR correction). **C.** mTOR pathway annotated transcript levels, expressed as relative level. Each of these transcripts changed >1.5-fold as compared to wild type cells (q<0.05). **D.** Gene ontology analysis of metabolism annotated transcripts with increased or decreased expression in CTR1 mutants. KEGG database was queried with the ENRICHR engine. Fisher exact test followed by Benjamini-Hochberg correction. **E.** mTOR signaling pathway diagram modified from KEGG map04150. See Supplemental Data File 1 for raw data.

We analyzed the CTR1 KO proteome, phosphoproteome, and metabolic transcriptome to determine whether increased mitochondrial biogenesis could be contributing to copper deficiency phenotypes (Supplemental Figure S3; Supplemental Data File 1). We explored enrichment of cis-regulatory elements responsive to transcription factors across these datasets (Supplemental Figure S3A). The CTR1 KO cell proteomes and transcriptome were not enriched in genes containing transcription factor sites implicated in mitochondrial biogenesis such as PPARGC1A, NRF1, NFE2L2, ESRRA, or YY1 (Scarpulla et al., 2012; Corona and Duchen, 2016; Popov, 2020). Furthermore, there were no gross changes to the mitochondrial proteome (Supplemental Figure S3B), including mitochondrial nucleoid proteins as a proxy for mitochondrial genome copy number (Supplemental Figure S3C). These results argue against increased mitochondrial biogenesis in CTR1 KO cells.

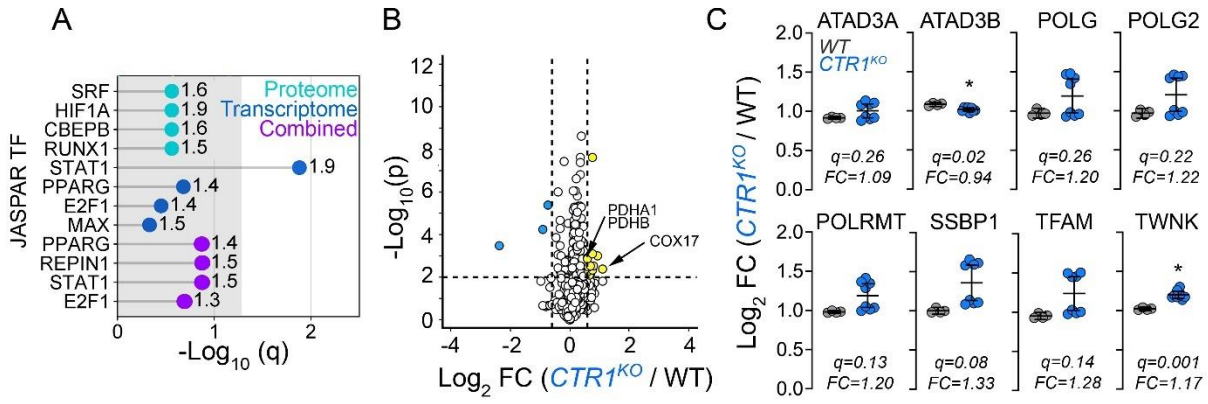

Figure S3. No evidence of increased mitochondrial biogenesis in the CTR1 mutant proteome and metabolic transcriptome.

A. Analysis of transcription factor enrichment in the CTR1 proteome, metabolic transcriptome, or combined datasets (Supplemental Data File 1: tabs 2A, S2B, S3A). The Enrichr engine was used to query the Jaspar Core database (Rauluseviciute et al., 2024). Fisher exact test followed by Benjamini-Hochberg correction (q values). Values on top of lollipops correspond to the odds ratio. There is no significant enrichment of proteins whose genes contain transcription factor sites implicated in mitochondrial biogenesis (PPARGC1A, NRF1, NFE2L2, ESRRA, YY1) (Scarpulla et al., 2012; Corona and Duchen, 2016; Popov, 2020). **B**. Volcano plot of the 901 Mitocarta 3.0

annotated proteins presented in the TMT proteome in Figure 2A. COX17, PHDHA1, and PDHB are presented as landmarks for comparison. **C**. Representative examples of proteins in panel B annotated to the mitochondrial nucleoid. Nucleoid proteins are used as indicators of mitochondrial content and/or biogenesis. In panels B and C most proteins do not significantly change in CTR1 null cells ($q<0.05$ and fold of change >1.5).

Collectively, the metabolic transcriptome and proteome of CTR1 KO cells provide independent evidence of increased activation of PI3K-Akt and mTORC1-S6K signaling pathways.

3.3.3 Increased steady-state activity of the mTOR-S6K pathway in CTR1 KO cells

To confirm the findings of our proteomic and transcriptomic datasets, we examined steady-state levels of several proteins identified in the CTR1 KO proteome by immunoblot and compared them to the housekeeping protein beta-actin (Figure 3A). CTR1 KO cells exhibit increased levels of the copper chaperone COX17, as well as reduced levels of DEPTOR and EIF2AK3 (Figure 3A). However, despite the severe copper depletion in CTR1 KO cells (Figure 1B), we did not observe changes in the levels of ATP7A or CCS (Figure 3A), two proteins frequently altered in copper depletion (Bertinato et al., 2003; Kim et al., 2010). In agreement with the proteomic profiling of these cells, there was no change in protein levels of RPTOR or RICTOR, both components of mTOR complexes (Figure 3A).

We tested the hypothesis of heightened mTOR signaling in CTR1 KO cells by measuring the phosphorylation status of mTOR and p70/p85 S6K1. We used serum depletion and serum addition paradigms to inhibit or stimulate, respectively, mTOR-S6K and PI3K-Akt signaling pathway activity (Liu and Sabatini, 2020). We focused on mTOR S2448 and S6K1 T389 phosphorylation as sensors of mTOR signal transduction. mTOR S2448, which we identified in the CTR1 KO phosphoproteome (Figure 2H), is present in the mTOR catalytic domain, is sensitive to nutrient availability and insulin, and is an S6K target (Navé et al., 1999; Reynolds et al., 2002; Cheng et al., 2004; Chiang and Abraham, 2005). The phosphoresidue T389 in S6K1 is phosphorylated by an insulin- and mTOR-dependent mechanism and indicates increased S6K

activity (Burnett et al., 1998; Pullen et al., 1998; Liu and Sabatini, 2020). Relative to wild type cells, CTR1 KO cells had an increased mTOR and S6K1 phosphorylation at time 0 after an overnight serum depletion paradigm, revealing elevated mTOR activity even in the absence of an mTOR activating stimulus (Figure 3B, compare lanes 1 and 5). Exposing these cells to serum progressively increased mTOR and S6K1 phosphorylation to a higher degree when comparing CTR1 KO to wild type cells (Figure 3B, compare lanes 2-4 to 6-8). Additionally, CTR1 KO cells displayed increased phosphorylation of mTOR and S6K1 at baseline (0h in complete media) and over time after removal of serum (Figure 3C), indicating that the mTOR signaling is resistant to serum deprivation in CTR1 KO cells. These results demonstrate that CTR1 KO cells have heightened activity of the mTOR-S6K signaling pathway.

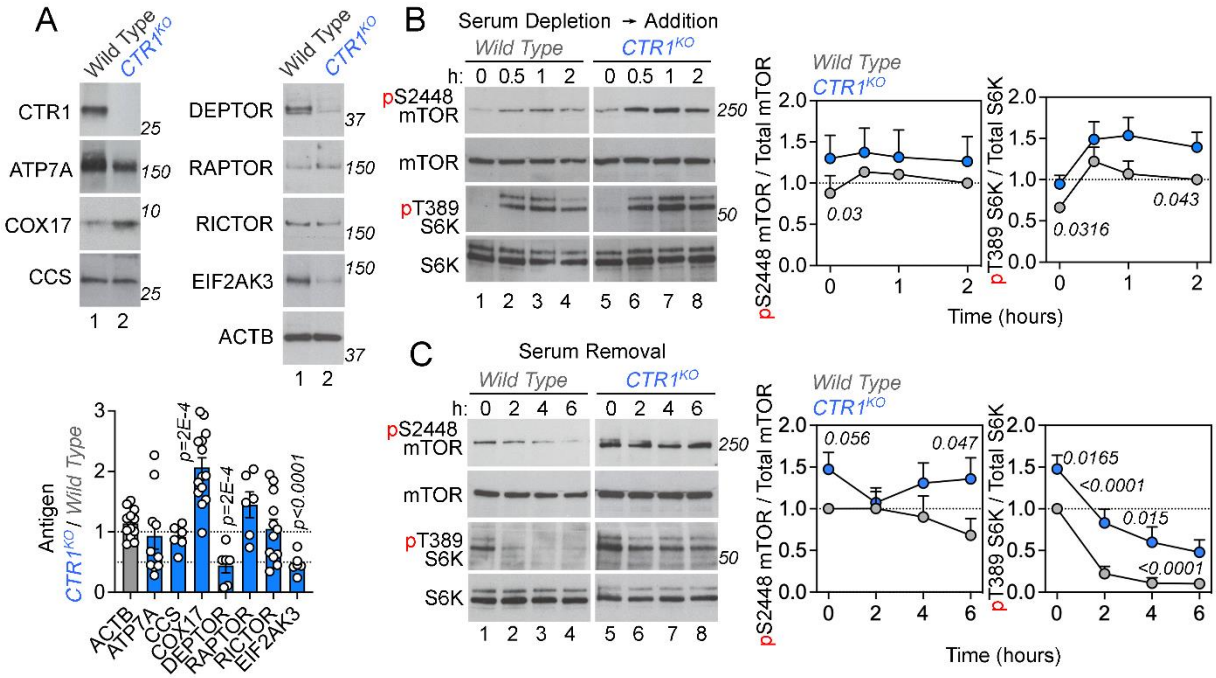

Figure 3. Increased activity of the mTOR-S6K pathway in CTR1 KO cells.

A. Immunoblots of whole-cell extracts from wild-type and CTR1 mutant cells probed for ATP7A, COX17, CCS, DEPTOR, RAPTOR, RICTOR, and EIF2AK3 with actin as a loading control. Immunoblots were quantified by normalizing protein abundance to wild-type cells. Italicized numbers represent p values analyzed by two-sided permutation t-test. **B,C.** Immunoblots with antibodies

detecting either phosphorylated or total mTOR or S6K as loading controls after overnight depletion of fetal bovine serum followed by serum addition for 0.5-2 hours (**B**, top) or at time 0 followed removal of fetal bovine serum for 2-6 hours (**C**, bottom). Graphs depict quantitation of blots on the left in 3-6 independent replicates as the ratio of the phosphorylated to total protein content, normalized to control at time 0 (**C**) or time at 2 hours (**B**) (Two-Way ANOVA followed by Benjamini, Krieger, and Yekutiel corrections).

3.3.4 Activation of the mTOR-S6K signaling pathway is necessary for CTR1 KO cell survival

mTOR signaling is necessary for cell division, growth, and differentiation (Liu and Sabatini, 2020). We asked whether increased mTOR-S6K activation contributes to cell division and growth in CTR1 KO cells by measuring cell survival after pharmacological manipulation of mTOR activity. We reasoned that the increased mTOR signaling in CTR1 KO cells (Figures 2 and 3, Supplemental Figure S2) would render mutant cells more sensitive to mTOR inhibition as compared to wild type cells. We quantitively assessed whether mTOR inhibition and cellular copper-modifying drugs interacted synergistically or antagonistically in cell survival assays (Ianevski et al., 2022). We used the zero-interaction potency (ZIP) model, which assumes there is no interaction between drugs, an outcome represented by a ZIP score of 0 (Yadav et al., 2015). ZIP scores above 10 indicate the interaction between two agents is likely to be synergistic, whereas a value less than -10 is likely to describe an antagonistic interaction (Yadav et al., 2015).

We first tested the individual effect of two activators of the mTOR-S6K signaling pathway, serum or insulin, on cell survival. CTR1 KO cells are more resistant to serum depletion and exhibit a reduced growth response when treated with insulin, which activates Akt and stimulates mTOR activity (Liu and Sabatini, 2020) (Figure 4A). This is consistent with increased mTOR activation in these cells. We next asked whether serum and the mTOR inhibitors rapamycin and Torin-2 (Supplemental Figure S4) would interact in a genotype-dependent manner to affect cell survival. Rapamycin is the canonical mTORC1 inhibitor, while Torin-2 inhibits both mTORC1 and mTORC2

with increased specificity and potency (Ballou and Lin, 2008; Zheng and Jiang, 2015). Based on our model, a synergistic response between serum and mTOR inhibitors (increased survival beyond the pro-survival effects of serum alone) would indicate that mTOR activity is deleterious for cell survival. Alternatively, an antagonistic response (negation of the pro-survival effect of serum by mTOR inhibition) would suggest cells are dependent on mTOR signaling for survival. Our results supported the latter, as the interaction between serum and either rapamycin or Torin-2 was antagonistic in both control and CTR1 KO cells (Figure 4, B–D; Supplemental Figure S5A). The antagonism between serum and both rapamycin and Torin-2 was more pronounced in CTR1 KO as compared to wild type cells (ZIP score between -22.1 to -27.7 for wild type and -30.9 to -34.6 for CTR1 mutant cells, Figure 4C), signifying that inhibiting mTOR is more detrimental to the pro-survival effects of serum in CTR1-null cells.

Importantly, genotype-dependent differences in cell survival after mTOR inhibition were sensitive to pharmacological manipulation of copper levels. mTOR inhibitors in combination with the copper chelator BCS abrogated ZIP score differences between genotypes (-35.6 to -38.3 for wild-type and -33.8 to -37.9 for CTR1 KO, Figure 4C; Supplemental Figure 5, B and C). Conversely, low doses of elesclomol, which are sufficient to rescue copper content phenotypes and mitochondrial respiration in CTR1-null cells (Figure 1, B, E, and F; Supplemental Figure S1, D and E), rendered CTR1 KO cells more resistant to increasing concentrations of Torin-2 (Figure 4, E–G; Supplemental Figure S5D). These pharmacogenetic epistasis studies indicate that CTR1-null cells are more dependent on mTOR activity for their survival in a copper-dependent manner. These findings support a model where the activation of mTOR is an adaptive response in CTR1 mutant and copper-deficient cells.

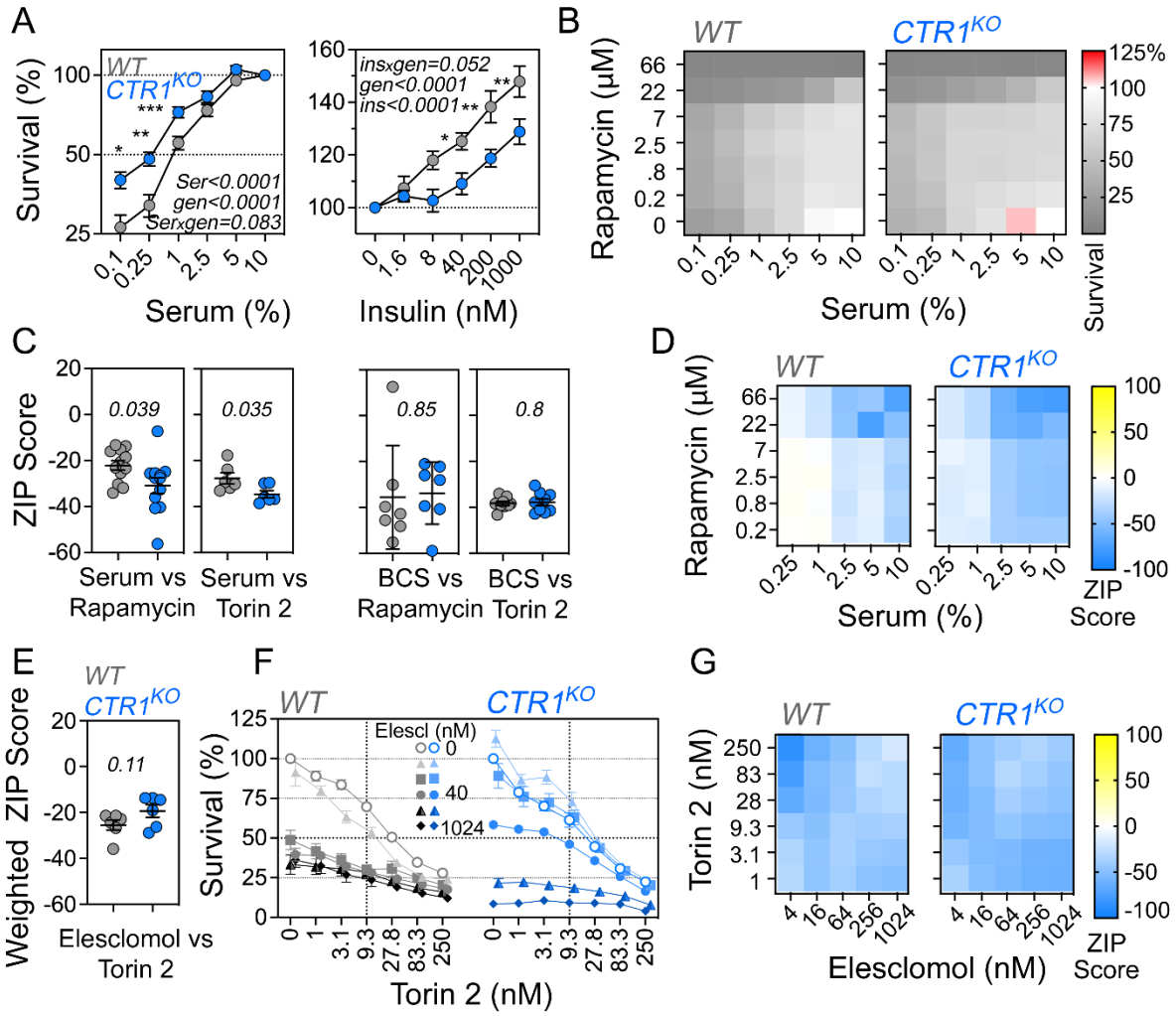

Figure 4. CTR1 knockout increases susceptibility to mTOR inhibition.

A. Cell survival analysis of CTR1 mutants with increasing concentrations of serum or insulin (average ± SEM, n = 7 for serum and 5 for insulin, two-way ANOVA followed by Benjamini, Krieger, and Yekutieli corrections). **B-G.** Synergy analysis of cell survival of CTR1 mutants treated with increasing concentrations of combinations of the compounds serum, rapamycin, Torin-2, BCS, and elesclomol. **B.** Cell survival map for cells treated with serum and rapamycin, with the corresponding interaction synergy map calculated using the Zero Interaction Potency (ZIP) score for cell survival (Yadav et al., 2015) (**D**). **C-G.** Scores below -10 indicate an antagonistic interaction between the compounds. Maps were generated with at least six independent experiments per pair that generated percent cell survival maps presented in Supplemental Fig. S5 and average ZIP score for drug interactions in **C** or weighted ZIP score in **E** (see Methods). Average ± SEM, two-sided permutation t-test. **E-G.** Synergy analysis

of CTR1 mutants with increasing concentrations of Torin-2 and elesclomol, with different colors and symbols indicating increasing concentrations of elesclomol (**F**) with average weighted ZIP score (**E**, two-sided permutation t-test) and elesclomol ZIP interaction synergy map (**G**).

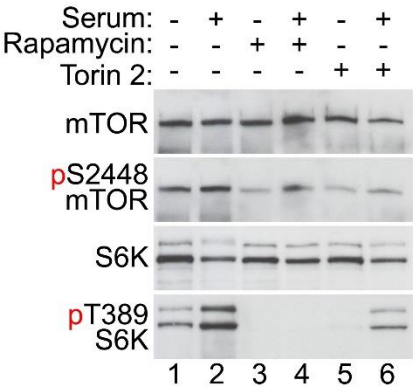

Figure S4. mTOR inhibitors reduce phosphorylation of mTOR and S6K.

Immunoblot of total and phosphorylated mTOR and S6K after overnight serum depletion in 0.2% serum, 30 minute pretreatment with rapamycin (270 nM) or Torin-2 (1 nM) in existing 0.2% serum media, followed by a switch to fresh media with 0.2% or 20% serum, rapamycin, and/or Torin-2 for 30 minutes.

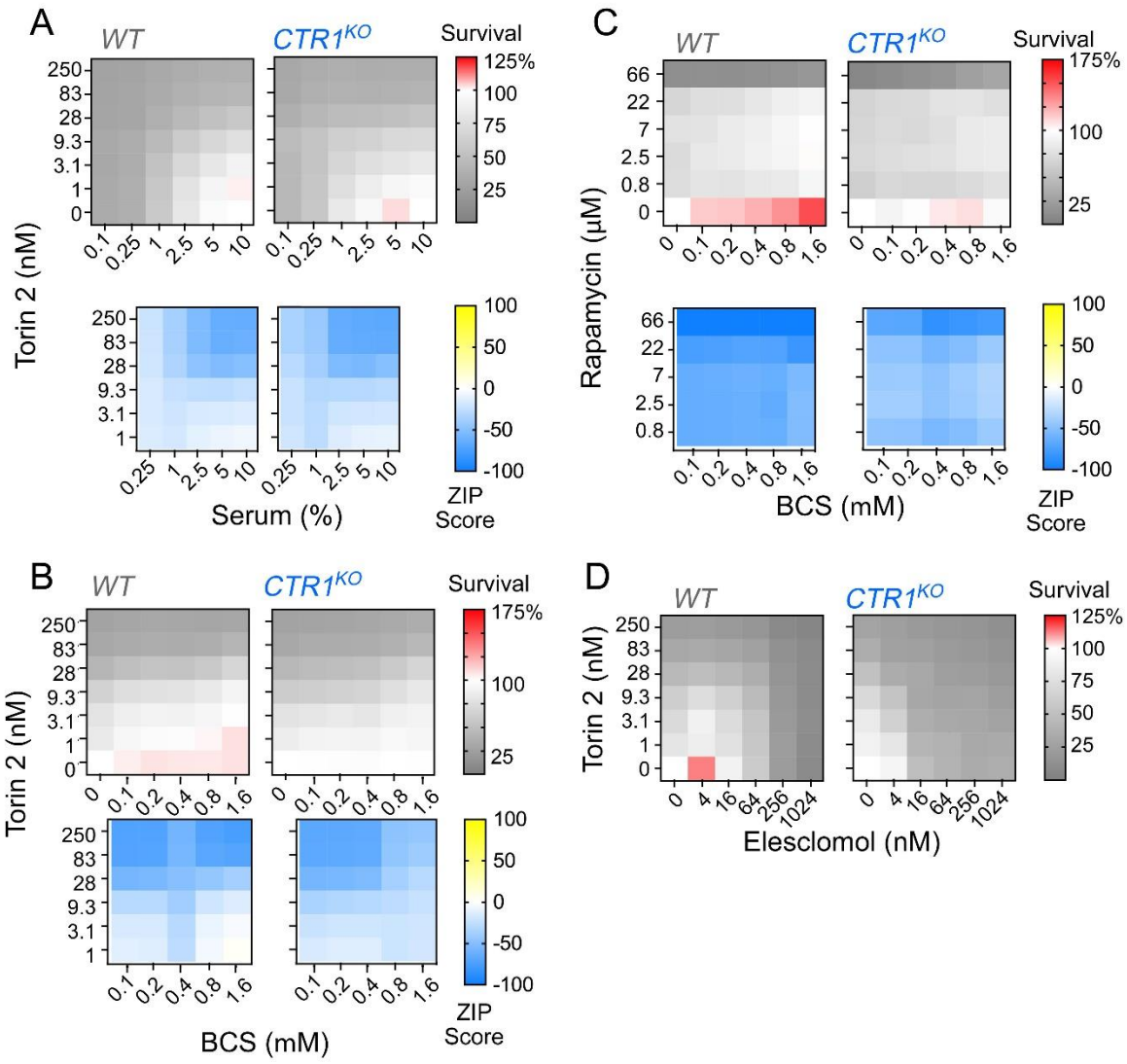

Figure S5. Synergy analysis of CTR1 mutant cells.

A-D. Quantification of survival and drug synergy in wild-type and CTR1 mutant cells treated with Torin-2 and serum (**A**), Torin-2 and BCS (**B**), rapamycin and BCS (**C**), or Torin-2 and elesclomol (**D**). Gray panels represent cell survival normalized to untreated cells, as described in Figure 4. Blue panels represent the corresponding interaction synergy map calculated using the Zero Interaction Potency (ZIP) score for cell survival (Yadav et al., 2015) (refer to Figure 4).

3.3.5 Interaction between mitochondrial respiration and increased protein synthesis in CTR1 KO cells

CTR1-null cells have increased activity of the mTOR-S6K pathway and decreased content of PERK (EIF2AK3), predicting increased protein synthesis in CTR1 KO cells as compared to wild type. We measured protein synthesis using puromycin pulse labeling of the proteome (Schmidt et al., 2009). Indeed, CTR1 KO cells display a 1.5-fold higher content of peptidyl-puromycin species as compared to wild type cells (Figure 5A; Supplemental Figure S6, A and B). Puromycin incorporation was sensitive to the cytoplasmic protein synthesis inhibitor emetine in both genotypes (Figure 5A). These results demonstrate increased protein synthesis in CTR1 mutant cells (Figure 5A; Supplemental Figure S6, A–B). To further explore the mechanism by which mTOR-S6K activation and upregulation of protein synthesis may be an adaptive response by CTR1 KO cells, we tested whether cell survival and mitochondrial respiration were susceptible to protein synthesis inhibition in a genotype-dependent manner. We indirectly inhibited protein synthesis using serum depletion or directly with emetine (Figure 5A) (Grollman, 1966; Mukhopadhyay et al., 2016). While CTR1 KO cell survival was resistant to serum depletion (Figure 4A), we found a discrete yet significant decrease in cell survival in CTR1 KO cells after emetine addition (Supplemental Figure S6, C and D).

To measure whole-cell mitochondrial respiration (as defined by its abrogation with a mix of rotenone plus antimycin) over extended periods of time, we employed the Resipher system, which utilizes platinum organo-metallic oxygen sensors (Grist et al., 2010; Wit et al., 2023). In contrast with Seahorse, which requires serum-free media and measures oxygen consumption over a few hours, Resipher allows oximetry over prolonged periods while maintaining cells in their own milieu. We first measured respiration continuously over 48 h in standard media with 10% fetal bovine serum. Respiration increased over time in both genotypes, a reflection of cell number expansion (Figure 5B1). CTR1 KO cell respiration was 35% of wild type levels (Figure 5B1), a phenotype that cannot be explained by differences in cell numbers between genotypes

(Supplemental Figure S6E) and reproducing the respiratory phenotypes observed in Seahorse (Figure 2E, compare columns 1 and 2, 53% of wild type basal respiration). However, a switch to low serum media decreased mitochondrial respiration in both genotypes (Figure 5B1). To compare the relative effect of serum depletion on each genotype, we normalized the OCR values to the last time point before serum switch and revealed that CTR1-null cells respire 1.5 times more efficiently than wild type cells during serum depletion (Figure 5B2). This effect cannot be explained by changes in cell number after switching to low serum (Supplemental Figure S6E). These results show that mitochondrial respiration is resistant to serum depletion in CTR1-null cells.

Next, we compared respiration in CTR1 KO and wild type cells treated with fresh complete media containing either vehicle or emetine to directly inhibit cytoplasmic protein synthesis (Figure 5, C and D). First, we observed genotype-dependent effects of vehicle treatment. After the addition of new media, wild-type cells respire at the same rate as before the media switch (Figure 5C), but CTR1 KO cells rapidly increase respiration, with a brief period where their raw OCR values are even greater than wild-type cells (Figure 5C1). Relative to the last timepoint before media switch, CTR1 KO cells respire 1.7-fold more efficiently than wild-type cells (Figure 5C2). Surprisingly, an increase in raw OCR was also observed in CTR1 KO cells after emetine treatment even above what was observed in vehicle-treated KO cells (Figure 5D1, compare to 3,4 in C1). Normalized wild type cell respiration was inhibited by 40% after emetine treatment (Figure 5D2). In contrast, the normalized respiration was resistant to emetine in CTR1-null cells (Figure 5D2). These effects cannot be attributed to differences in cell number (Supplemental Figure S6F). We conclude that CTR1-deficient cell respiration is resistant to direct inhibition of protein synthesis.

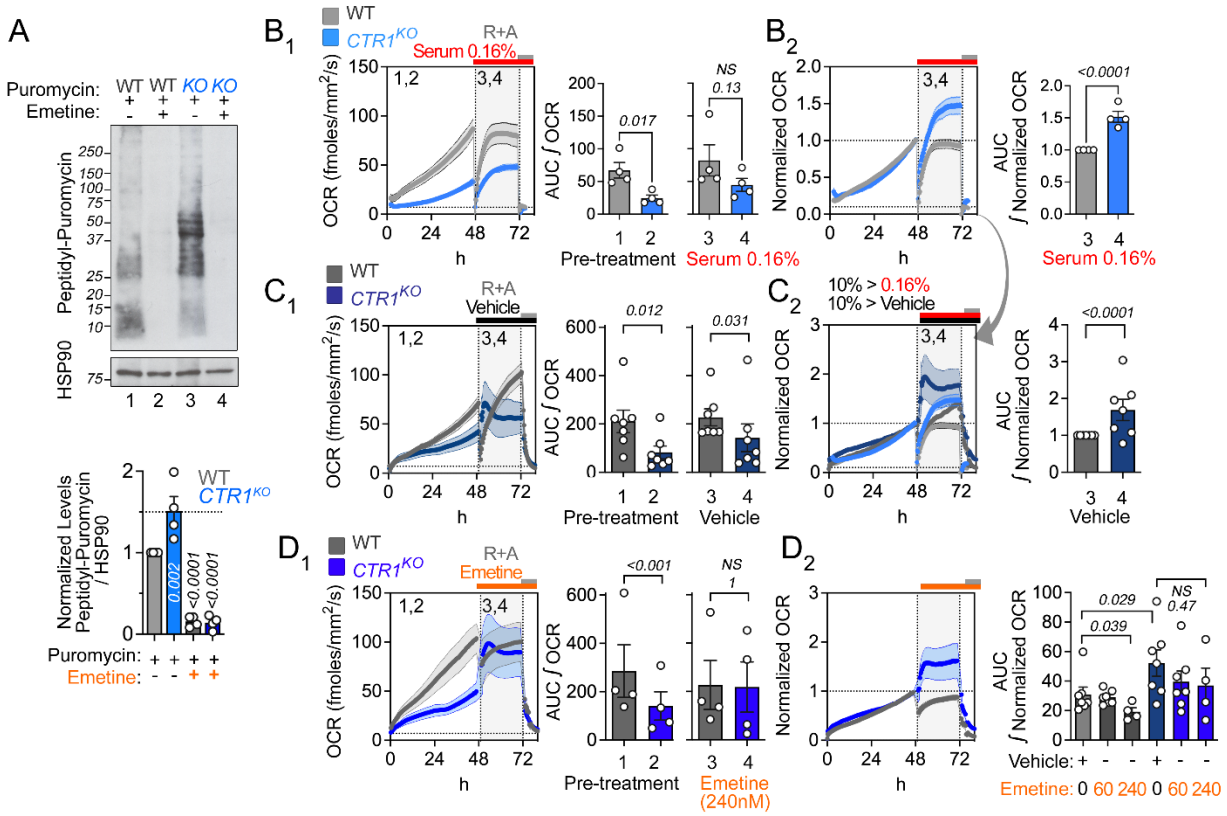

Figure 5. CTR1 mutant cells are resistant to protein synthesis inhibition.

A. Immunoblot for puromycin in wild-type (lanes 1 and 2) and CTR1 mutant cells (lanes 3 and 4) treated with either vehicle (lanes 1 and 3) or 240 nM emetine (lanes 2 and 4) for 24 hours, followed by a 30 min pulse of puromycin. Quantification of the puromycin signal between 250 and 15 kDa normalized to HSP90. One-Way ANOVA, followed by Holm-Šídák's multiple comparisons test. CTR1 clone KO20 was used for all experiments. **B-D.** Resipher respiration rates in wild type and CTR1 KO cells. Cells were grown in complete 10% serum media unless otherwise specified. Cells were incubated for 48h, followed by serum depletion (**B**, serum 0.16%), vehicle (**C**, DMSO), or emetine (**D**, 60 or 240 nM) for 24h. **B-D.** Assay was terminated at 72 h by the addition of rotenone plus antimycin (R+A). Columns 1 and 2 represent raw or normalized OCR, respectively, presented as OCR over time or the integrated area under the curve (AUC) for the indicated time periods. Each dot depicts a batch of concurrent experiments (n=4-7 per genotype for each experiment, average ± SEM, two-sided permutation t-test).

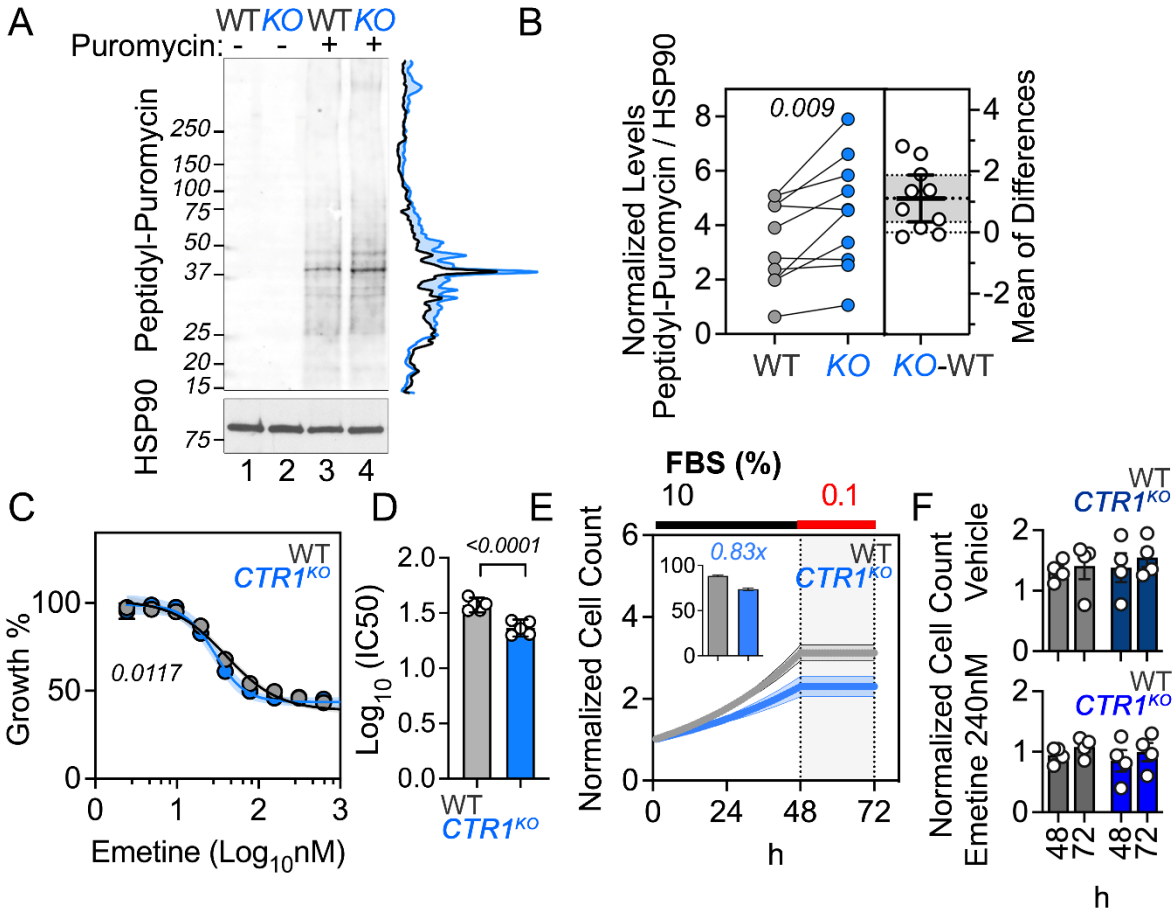

Figure S6. Cell survival under conditions inhibiting protein synthesis.

A-B. Immunoblot for puromycin using a nitrocellulose membrane in wild-type and CTR1 mutant cells treated with vehicle (lanes 1 and 2) or puromycin for 30 min (lanes 3 and 4). Line trace represents the corresponding quantification of signal intensity. **B.** Quantification of the puromycin signal between 250 and 15 kDa normalized to HSP90. Paired two-tailed t test (pairing r=0.86, p=0.0007). **C-D.** Cell growth analysis of wild type and CTR1 mutants with increasing concentrations of emetine for 24 hours (**D**, Average ± SEM, n = 6, p value calculated with Sum-of-squares F test analysis) and corresponding IC50 (**B**, two-sided permutation t-test), as measured by Alamar blue. **E.** Cell growth of wild type and CTR1 KO cells in complete media and serum depletion after 48h as measured by total protein, normalized to the seeding cell number at time zero. Insert shows the percent difference in cell counts after the initial 48h. n=4 Average ± SEM. **F.** Normalized cell counts in wild type and CTR1 KO cells either in the absence or presence of 240 nM emetine for the indicated times. CTR1 clone KO20 was used for all experiments in **C-F**.

3.3.6 Upregulation of protein synthesis machinery in a mouse model of copper deficiency

Next, we wanted to determine whether animal models of copper deficiency would corroborate our observations in CTR1 KO cells that copper depletion increases mTOR-S6K pathway activity and upregulates multiple pathways promoting protein synthesis. To address this question, we performed spatial transcriptomics of the cerebellum of *Atp7a*$^{flx/Y}$ *:: Vil1*$^{Cre/+}$ mice, a conditional mouse model of Menkes disease. These mice, which lack the copper efflux transporter ATP7A in intestinal enterocytes, are unable to absorb dietary copper, depleting the brain of this metal and inducing subsequent pathology that phenocopies Menkes disease (Wang et al., 2012). We selected the cerebellum as it is known to be one of the earliest brain regions affected in Menkes disease, with Purkinje cells being particularly affected (Barnes et al., 2005; Gaier et al., 2013; Zlatic et al., 2015). To focus on mechanisms that could serve as an adaptive response to brain copper deficiency, we chose to study the transcriptome of the cerebellum at postnatal day 10, a presymptomatic timepoint before Purkinje cell death and the rapid onset of high mortality in this model and other Menkes mouse models (Wang et al., 2012; Guthrie et al., 2020; Yuan et al., 2022). As Menkes is a sex-linked disease, we focused our analysis on male mice.

We first confirmed that *Atp7a*$^{flx/Y}$ *:: Vil1*$^{Cre/+}$ mice exhibit systemic copper depletion by ICP-MS as previously reported (Supplemental Figure S8A) (Wang et al., 2012). Next, we used the NanoString GeoMx Digital Spatial Profiler to generate anatomically resolved, quantitative, and PCR amplification-free transcriptomes (Decalf et al., 2019; Merritt et al., 2020; Zollinger et al., 2020) for two regions of interest (ROIs): the Purkinje cell and granular layers of the cerebellum (Figure 6A). Within these ROIs, we segmented our analyses by GFAP immunoreactivity to enrich for areas of illumination (AOIs) containing Purkinje cells (GFAP-) or astrocytes in the granular layer (GFAP+) (Figure 6B, Supplemental Figure S7A). Using the GeoMx Mouse Whole Transcriptome Atlas (mWTA) and a mouse cerebellar cortex atlas (Kozareva et al., 2021), we quantified the transcriptome in these ROIs with a sequencing saturation above 80% (Supplemental Figure S7B). After data normalization, we analyzed 19,963 genes across 58 AOIs

from 4 animals of each genotype selected across different cerebellar folia. 17,453 genes were expressed in 10% of AOIs, and 10,290 genes were expressed in 50% of AOIs (Supplemental Figure S7, C and D). Segmentation by GFAP produced expected patterns of gene expression in Purkinje cell or granular layer AOIs, such that genes associated with Purkinje cells like *Calb1* and *Pcp2* were highly expressed in corresponding AOIs and minimally expressed in AOIs within the granular layer (66-fold enrichment of *Calb1* in Purkinje cell AOIs, Figure 6C; Supplemental Figure S7E; Supplemental Figure S8, B and C). Genes associated with granule cells and astrocytes were enriched in AOIs within the granular layer but had little expression in Purkinje cell AOIs (Supplemental Figure S8, B and C). Furthermore, the transcriptome of wild type Purkinje cells was enriched in genes annotated to MitoCarta3.0 knowledgebase ((Rath et al., 2021), Supplemental Figure S8F), metabolic ontologies including oxidative phosphorylation (MSigDB p6.5E-43, Fisher exact test followed by Benjamini-Hochberg correction) and the mTOR pathway (MSigDB p2.4E-12) as compared to the granular layer (Supplemental Figure S8, E, G, and H).

In Purkinje cells from mutant mice, we revealed increased expression of several genes annotated to the Human MSigDB mTOR pathway (Liberzon et al., 2011). These include the most upstream mTOR activator, insulin (*Ins*, 1.75 fold); S6-related kinase (*Rskr*, 1.75 fold); Nerve Growth Factor Receptor (*Ngfr*, 1.48 fold); *Mertk*, a tyrosine kinase (1.42 fold); interferon-induced transmembrane protein 1 (*Ifitm1*, 1.5 fold); and leukotriene C4 synthase (*Ltc4s*, 1.66 fold) (Figure 6D). At the protein level, we observed increased phosphorylation of the insulin-like growth factor 1 receptor Igf1r at Tyr1135/Tyr1136 with no change in expression of the receptor, as measured by Luminex or label-free mass spectrometry of the cerebellum, respectively (Figure 6E). Notably, IGF1-R stimulation has been reported to activate the p70 S6K1 pathway (Cai et al., 2017). Together, this shows that brain copper deficiency increases the expression of components of the mTOR-S6K pathway activity in Purkinje cells. There were no genotype-dependent changes in expression of components of the electron transport chain in either the Purkinje or granular layer ROIs (Supplemental Figure S9). We analyzed the spatial transcriptomic data by Gene Set

Enrichment Analysis (GSEA) (Subramanian et al., 2005; Korotkevich et al., 2019) to unbiasedly identify pathways disrupted by brain copper depletion in cerebellar cortex. We observed a global upregulation of the protein synthesis machinery, including 82 ribosomal subunits and protein synthesis elongation factors, in Purkinje cells but not in the granular layer (Figure 6G; FGSEA estimated p value Benjamini-Hochberg-correction). Expression levels of cytoplasmic ribosome transcripts were similar in wild type Purkinje cells and granular layer cells (Supplemental Figure S8D). Our data support a model of mTOR-dependent upregulation of protein synthesis machinery in Purkinje neurons in presymptomatic copper-deficient mice.

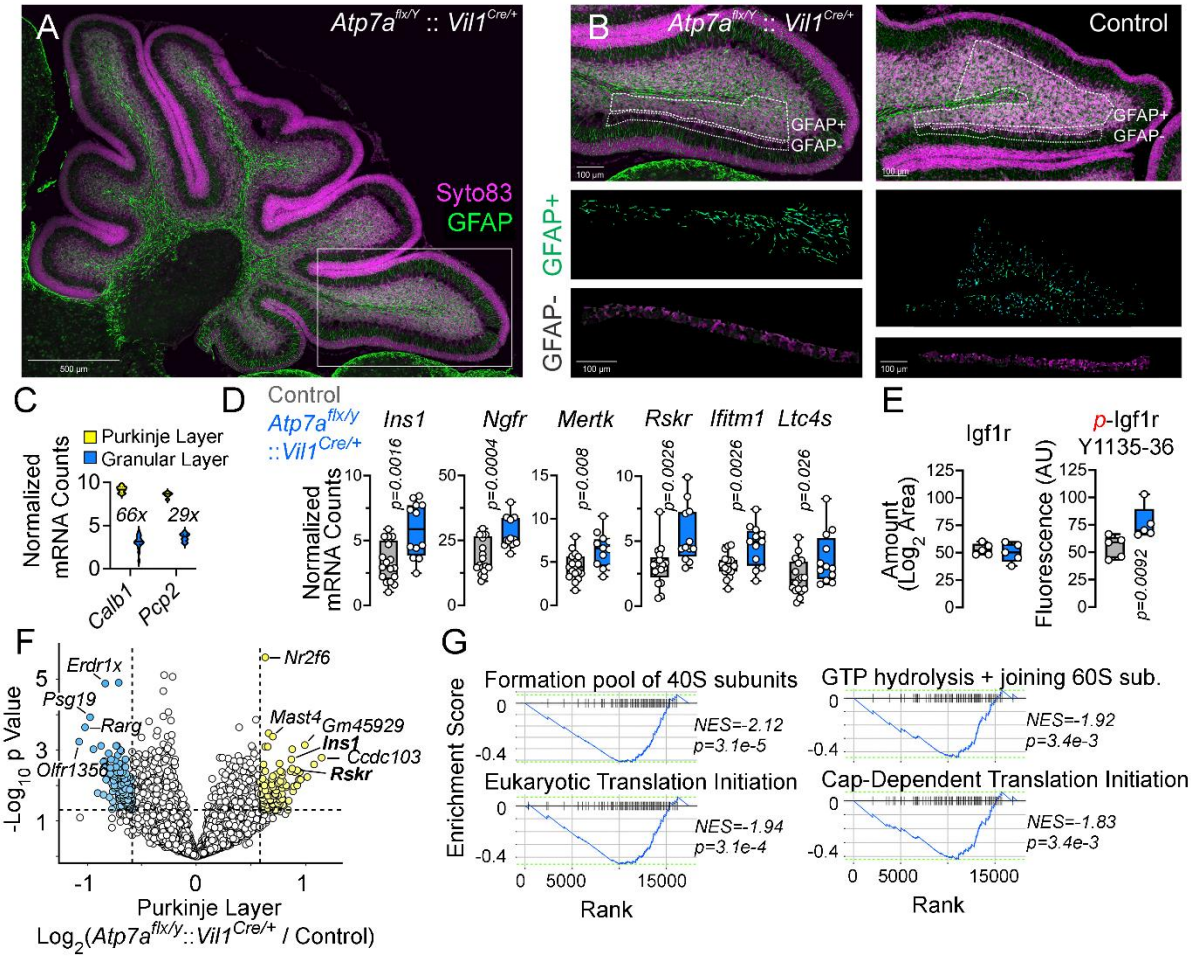

Figure 6. Transcriptome of cerebellar cortex layers in a presymptomatic Menkes mouse model.

A. Sagittal sections of control and *Atp7a*$^{flx/Y}$ :: *Vil1*$^{Cre/+}$ mutants at day 10 stained with Syto83 and GFAP to distinguish cerebellar layers. **B.** ROIs corresponding to the two AOIs analyzed: the GFAP-negative Purkinje cell layer AOI and the GFAP-positive granular layer AOI. **C.** Normalized mRNA counts for the Purkinje cell markers *Calb1* and *Pcp2* in the Purkinje and granular layer AOIs. **D.** Normalized mRNA counts for insulin and mTOR-S6 kinase related genes. Blue denotes mutant. n = 16 control AOIs and 13 mutant *Atp7a*$^{flx/Y}$ :: *Vil1*$^{Cre/+}$ AOIs, 4 animals of each genotype. **E.** Abundance of Igf1r protein and p-Igf1r (Tyr1135/Tyr1136) as measured by LFQ-MS or Luminex, respectively. Box plots are all two-sided permutation t-tests. **F.** Volcano plot of mRNAs differentially expressed in mutant *Atp7a*$^{flx/Y}$ :: *Vil1*$^{Cre/+}$ Purkinje neurons vs control. Yellow symbols mark genes with increased expression in mutant *Atp7a*$^{flx/Y}$ :: *Vil1*$^{Cre/+}$ Purkinje cells. **G.** Gene Set Enrichment Analysis and normalized enrichment score (NES) of genes differentially expressed by comparing controls to

mutant *Atp7a*$^{flx/Y}$ :: *Vil1*$^{Cre/+}$ Purkinje cells. Gene sets enriched in mutants correspond to negative NES. p values are corrected. See Supplemental Data File 2 for raw data.

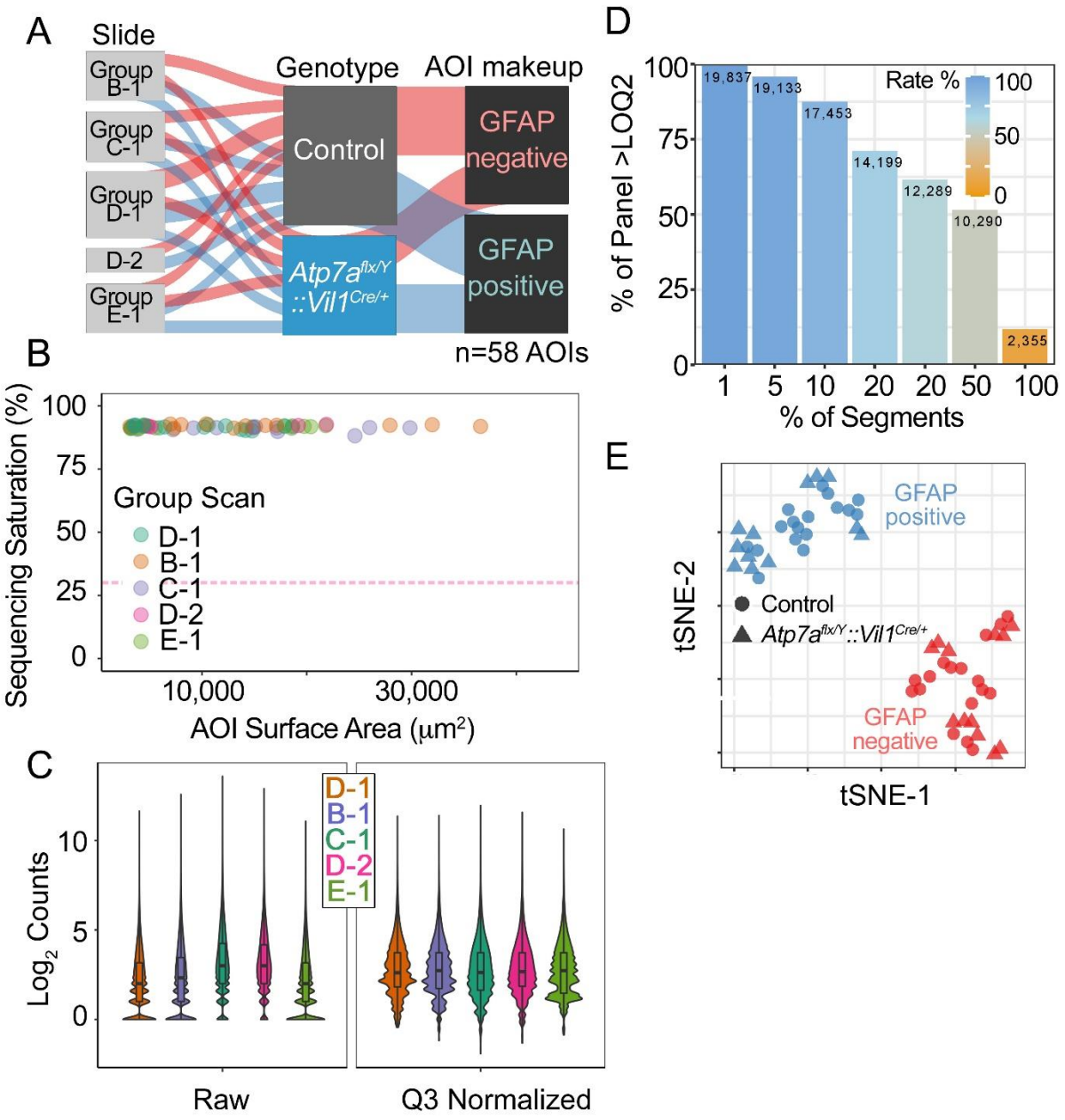

Figure S7. Spatial transcriptomics quality controls and descriptors.

A. Sankey diagram depicts an overview of samples (n=58) showing their annotations. **B**. Sequencing quality as measured by saturation to ensure sensitivity of low expressor genes. Sequencing saturation measures sequencing depth for a sample defined as (1 – % Unique reads). Threshold above 50% is considered a reliable determination. 0 samples below the 50% threshold. **C**. Sequencing reads raw and normalized to the third quartile (Q3) to account for differences in cellularity, area of interest (AOI) size, or other variables. **D.** number of genes in different percentages

of tissues expressed above LOQ2 (Limit of Quantitation), defined as the Geometric Mean of the negative probes, multiplied by the geometric standard deviation to the second power (^2). We assayed 19,963 genes across 58 AOIs. Of these 17,453 genes were expressed in 10% of AOIs and 10,290 genes expressed were expressed in 50% of AOIs. **E**. t-Distributed Stochastic Neighbor Embedding (t-SNE) of gene expression values per annotation. See Supplemental Data File 2 for raw data.

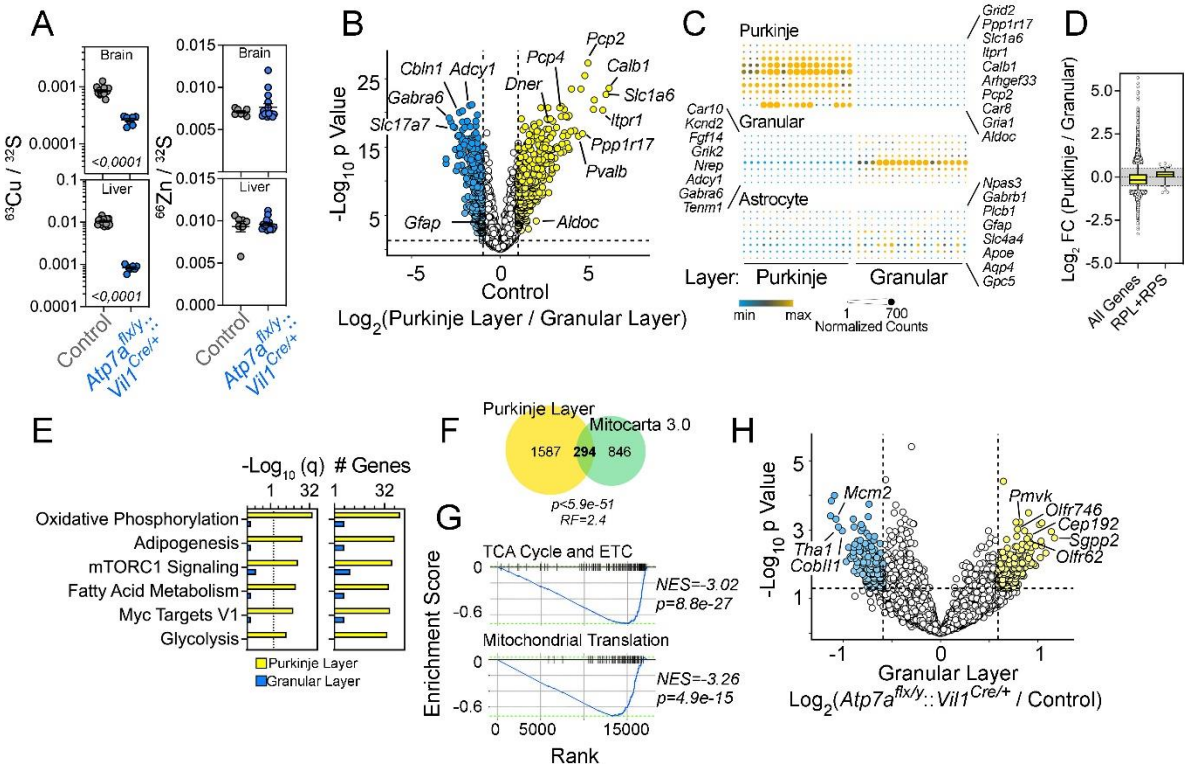

Figure S8. Cell type-specific gene expression in the cerebellar cortex in a presymptomatic Menkes mouse model.

A. 63Cu and 64Zn quantification in the brains of *Atp7a*$^{flx/Y}$ *:: Vil1*$^{Cre/+}$ mice at P10, normalized to 32S and analyzed by two-sided permutation t-test (italicized numbers represent p values). **B.** Volcano plot of mRNAs differentially expressed between the Purkinje and granular layer of control mice. **C.** Expression of selected cell type-specific markers (Kozareva et al., 2021). **D.** Differential expression of all transcripts compared to cytoplasmic ribosome subunits mRNAs. Whiskers correspond to 5-95 percentile, box represents 25 and 75 percentile, horizontal line marks the mean. Shaded area demotes ±1.5 fold difference. **E.** Gene ontology analysis of transcripts more highly expressed in Purkinje cells than granular layer cells. MSigDB was queried with the ENRICHR engine. Fisher exact test followed by Benjamini-Hochberg correction. **F.** 294 of the 1881 transcripts more highly expressed in wild-type Purkinje cells are annotated to the MitoCarta3.0 knowledgebase. **G.** GSEA and NES enrichment score of genes differentially expressed in wild-type Purkinje cells and granular layer cells reveal enrichment in metabolic ontologies. **H.** Volcano plot of mRNAs differentially expressed in the granular layer in mutant *Atp7a*$^{flx/Y}$ *:: Vil1*$^{Cre/+}$ mice vs control. Yellow symbols mark genes with

increased expression in the granular layer in mutant *Atp7a*$^{flx/Y}$ :: *Vil1*$^{Cre/+}$ mice. See Supplemental Data File 2 for raw data.

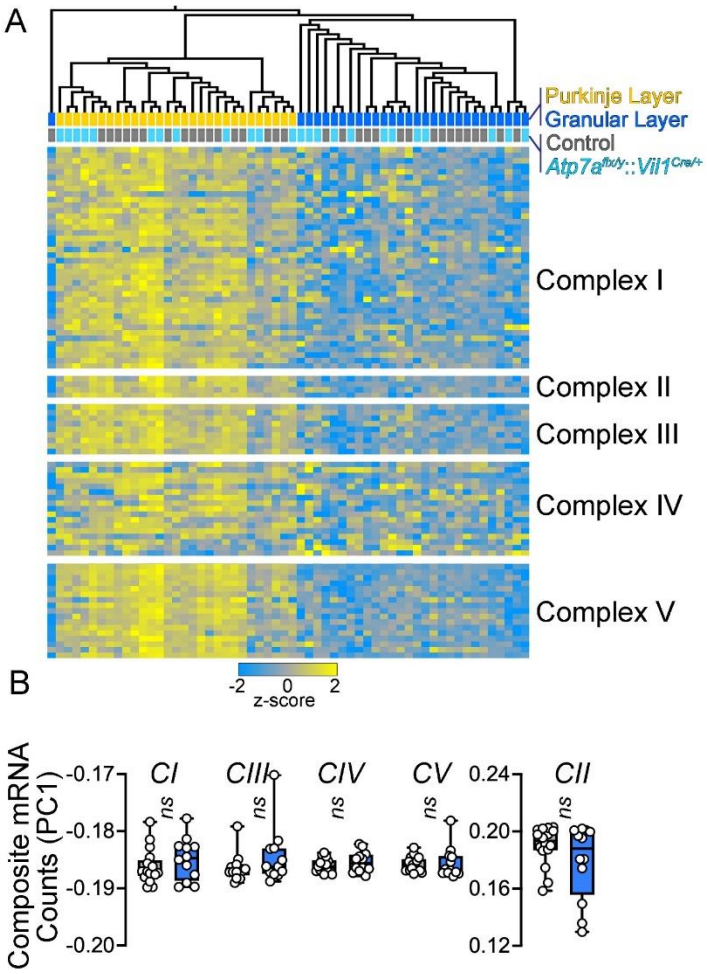

Figure S9. Respiratory complex subunit gene expression in a presymptomatic Menkes mouse model.

A. Hierarchical clustering of all transcripts annotated to electron transport chain subunits according to MitoCarta 3.0 across genotypes and AOIs quantified. **B.** Principal component 1 of data presented in A for the Purkinje layer. Permutation t test. See Supplemental Data File 2 for raw data.

3.3.7 Genetic modulation of mTOR pathway-dependent protein synthesis activity modifies copper deficiency phenotypes in Drosophila

We genetically tested whether increased activity of mTOR pathway-dependent protein synthesis was an adaptive or maladaptive mechanism in copper deficiency. We studied the effect of mTOR-S6K pathway gain- and loss-of-function on copper-deficiency phenotypes in *Drosophila.* While either full or intestinal KO of *ATP7A* in mice induces brain copper deficiency, overexpression of ATP7A phenocopies this neuronal copper deficiency in a cell-autonomous manner (Norgate et al., 2006; Binks et al., 2010; Hwang et al., 2014). In animals overexpressing *ATP7*, which induces copper depletion by metal efflux (*ATP7*-OE; Figure 7 and Supplemental Figure S10) (Norgate et al., 2006; Binks et al., 2010; Hwang et al., 2014; Gokhale et al., 2016; Hartwig et al., 2020), we also over-expressed and/or knocked down members of the mTOR pathway in either the epidermal epithelium (pnr-GAL4) or class IV sensory neurons (ppk-GAL4) (Figure 7 and Supplemental Figure S10) (Binks et al., 2010; Gokhale et al., 2016; Hartwig et al., 2020). *ATP7* overexpression in the dorsal midline caused depigmentation and bristle alterations in both males and females (Supplemental Figure S10). Loss of function of either S6k, raptor, or Akt by RNAi intensified epidermal *ATP7*-OE copper deficiency phenotypes (Supplemental Figure S10), including the induction of additional dorsal thoracic caving (*RAPTOR*-IR and *AKT*-IR), necrotic tissue (*RAPTOR*-IR and *AKT*-IR), thoracic “dimples’ (*S6K*-IR in males, see arrowheads), and ultimately with increased lethality in response to *Akt* RNAi, with the few surviving animals showing caving and necrosis of the thoracic dorsal midline and/or scutellum (Supplemental Figure S10). We did not detect overt *ATP7*-OE phenotype modifications by mTOR pathway transgene overexpression (*Akt* or *S6k*) or the two RNAi lines for *rictor* (Supplemental Figure S10). These results suggest an adaptive role of mTOR-Raptor-S6K-dependent protein synthesis machinery in copper deficiency.

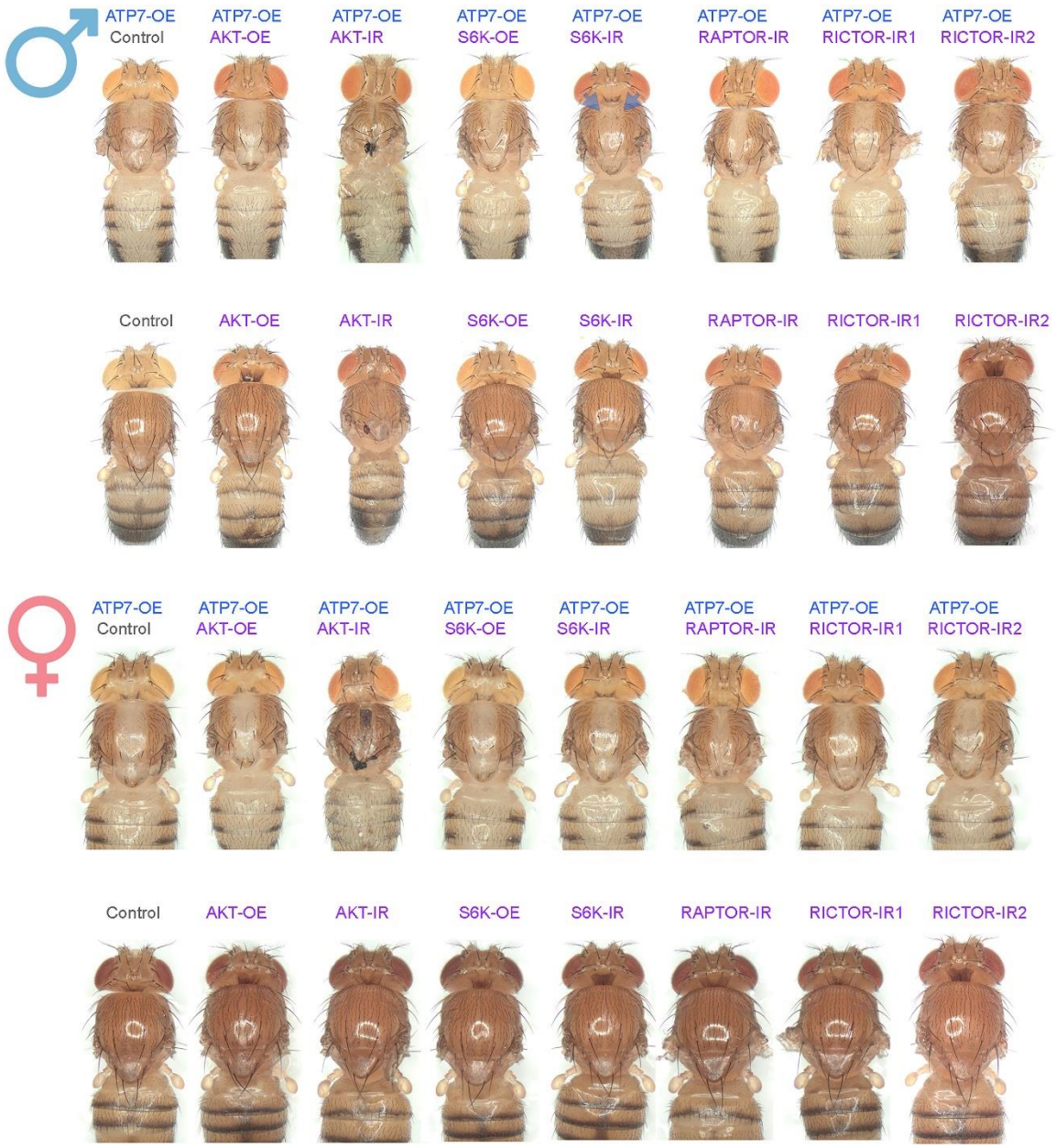

Figure S10. mTOR-Raptor-S6K pathway loss-of-function enhances copper-depletion phenotypes in *Drosophila* epidermis.

Expression of wild type ATP7 and/or wild type or RNAi of different components of the mTOR pathway in the epidermis of the thoracic segment using the pnr-GAL4 driver in males and females (see Table 3 and Methods). Arrowheads point to ‘dimples’ in the dorsal aspect of ATP7-OE; S6K-IR males.

To test whether gain-of-function of mTOR-dependent protein synthesis machinery would rescue *ATP7*-OE phenotypes, we measured the complexity of class IV sensory neuron dendritic arbors and mitochondrial distribution in the third instar *Drosophila* larva. Dendrites in this cell type are a sensitive and quantitative reporter to measure cell-autonomous mechanisms in neuronal copper homeostasis (Figure 7) (Gokhale et al., 2016; Hartwig et al., 2020). Copper deficiency due to overexpression of *ATP7* in these neurons decreased the complexity of the dendritic arbor (as quantified by average branch length and total dendritic length; Figure 7, A and B) and depleted mitochondria from dendrites (Figure 7C), as previously reported (Gokhale et al., 2016; Hartwig et al., 2020). The sole overexpression of *Akt* was not sufficient to modify *ATP7*-OE phenotypes (Figure 7, A and B). However, dendritic branch phenotypes were partially rescued by overexpression of either a constitutively active phosphomimetic mutant of *S6k* (*S6k*-STDETE, Figure 7, A and B) (Barcelo and Stewart, 2002) or RNAi against *Thor*, the *Drosophila* orthologue of 4-EBP1, an inhibitor of protein synthesis downstream of mTOR necessary for mitochondrial biogenesis (Figure 7, A and B) (Miron et al., 2001; Qin et al., 2016). 4E-BP1-dependent inhibition of protein synthesis is inhibited by mTOR-dependent phosphorylation; thus, 4-EBP1/Thor removal increases protein synthesis (Morita et al., 2013; Morita et al., 2015). *S6k*-STDETE-OE or *THOR*-IR increased the length of dendritic branches, a phenotype specific to the distal dendritic branches without changes in total dendritic length (Figure 7, A and B). This increase in the average branch length resulted in an expansion of the dendritic field coverage by class IV neurons (Figure 7, A and B). Simultaneously, mitochondria distribution was rescued in *ATP7*-OE neurons expressing *S6k*-STDETE-OE, with the redistribution of mitochondria to dendrites (Figure 7, C and D). These results demonstrate that activation of mTOR-dependent protein synthesis mechanisms partially revert copper-depletion neuronal phenotypes. We conclude that mTOR-dependent protein synthesis is an adaptive mechanism in neuronal copper deficiency.

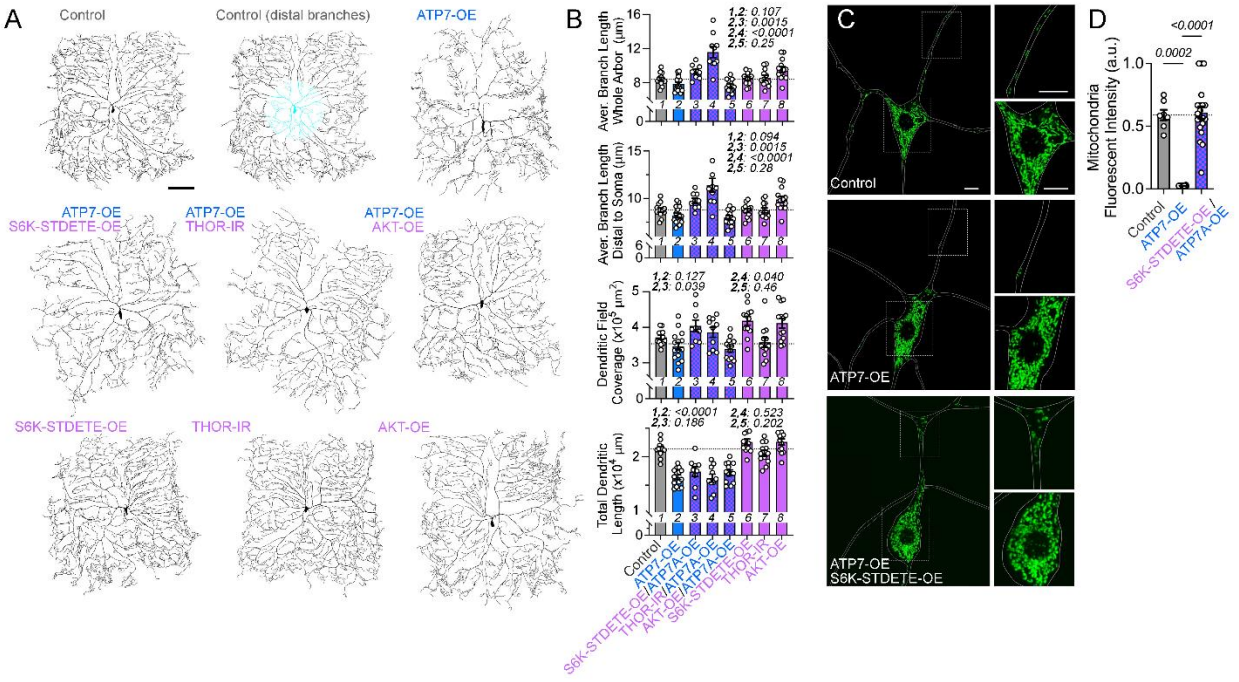

Figure 7. mTOR-dependent protein synthesis pathways ameliorate copper-depletion phenotypes in sensory neurons.

A. Representative reconstructed dendritic arbors from live confocal images of C-IV da neurons of the specified genotypes labeled by GFP (see Table 3 and Methods.) Scale bar: 100 µm. Right panel depicts 400 µM circle used to distinguish proximal and distal dendrites (see Methods). **B.** Quantitative analysis of dendritic parameters in the specified genotypes: average branch length for the entire dendritic arbor or for the region distal to the soma (see Methods), dendritic field coverage, and total dendritic length. Each dot represents an independent animal. Average ± SEM. Italicized numbers represent q values (One-Way ANOVA, followed by Benjamini, Krieger, and Yekutieli multiple comparisons correction). **C-D.** Representative live confocal images and quantification of C-IV da neurons of the specified genotypes expressing a mitochondria-targeted GFP that were manually traced using a plasma membrane marker (CD4-tdTomato, not shown). Scale bar: 5 µm. **D**. Quantitative analysis of mitochondrial fluorescence intensity [**_additional details to be provided by collaborator_]. Each dot represents an independent animal. Average ± SEM. Italicized numbers represent q values (Kruskal-Wallis test, followed by Dunn's multiple comparisons correction).

3.4 Discussion

Here, we report that concomitant to changes in bioenergetics, copper-depleted cells undergo mTOR and PERK signaling modifications which converge on an adaptive response of increased protein synthesis in cellular and animal models of copper depletion.

We first established a cellular model of copper depletion by CRISPR editing to knockout CTR1 in SH-SY5Y cells (Figure 1, Supplemental Figure S1). This cellular system recapitulates cardinal phenotypes of copper depletion such as compromises in copper-dependent enzymes including Complex IV of the respiratory chain, which drives cells into glycolysis with increased cellular lactate content (Figure 1, Supplemental Figure S1). This is consistent with previous reports that of the respiratory chain complexes, complex IV specifically is impaired in copper deficiency (Zeng et al., 2007; Ghosh et al., 2014; Soma et al., 2018). Importantly, respiration and metabolic phenotypes observed in CTR1 KO cells can be reverted by elesclomol (Figure 1, Supplemental Figure S1), a drug that rescues neurodegeneration and organismal survival in animal models of copper depletion (Guthrie et al., 2020; Yuan et al., 2022).

We used the CTR1 KO cell model to unbiasedly identify cellular processes sensitive to copper depletion. The proteome, phosphoproteome, and metabolic transcriptome of CTR1-null cells identified the mTOR signaling pathway as one of the most enriched terms (Figure 2, Supplemental Figure S2). Patterns of differential gene, protein, and phosphoresidues levels are indicative of increased mTORC1-S6K activation and downstream activation of protein synthesis through increased levels and phosphorylation of RPS6 (Figure 2, Figure 3). At least one of the mechanisms of this mTOR activation is through decreased expression and protein levels of the mTOR inhibitor DEPTOR (Figure 2, Supplemental Figure S2, Figure 3). We suspect additional mechanisms, such as increased receptor tyrosine activity, also contribute to increased mTOR activation, as evidenced by increased insulin-dependent activity observed in Purkinje neurons of copper-deficient *Atp7a*$^{flx/Y}$ *:: Vil1*$^{Cre/+}$ mice (Figure 6) and by the effect of *Akt*, *raptor*, and *S6k* RNAi enhancing *Drosophila* copper depletion epidermal phenotypes (Supplemental Figure S10).

Moreover, numerous proteins annotated to mTORC1-mediated signaling pathway exhibited increases in phosphorylation at residues responsive to mTOR and/or S6K activity, including mTOR, RPS6, EIF4G1, ACLY, UVRAG, and AKT1S1 (Figure 2). In support of the idea that CTR1-null cells increase mTORC1 signaling and downstream S6K activation, these cells exhibit increased phosphorylation at mTOR S2448 and S6K1 T389 at baseline as well as under conditions of serum depletion or addition as compared to wild-type cells (Figure 3). A notable finding is the discovery that concomitant to an upregulation of mTOR signaling and activation of S6K, we observed decreased protein expression and phosphorylation of EIF2AK3 (PERK) (Figure 2, Figure 3). As is expected by these changes in PERK and mTORC1 signaling, CTR1-null cells upregulate protein synthesis over wild-type cells (Figure 5, Supplemental Figure S6). In addition to these translational, post-translational, and functional changes in mTOR pathway activity in CTR1 KO cells, this signaling pathway also undergoes transcriptional regulation in both copper-deficient cells (Supplemental Figure S2) and Purkinje neurons in *Atp7a*$^{flx/Y}$ *::* *Vil1*$^{Cre/+}$ mice (Figure 6). The effects of mTOR activation in CTR1 KO cells span the RPTOR/Raptor (mTORC1) branch of the pathway, including increased expression of 14 transcripts annotated to mTOR and/or PI3K-Akt signaling (Supplemental Figure S2). Similarly, *Atp7a*$^{flx/Y}$ *::* *Vil1*$^{Cre/+}$ mice upregulate the protein synthesis machinery and expression of several genes in the mTOR pathway in Purkinje neurons at an early timepoint before the onset of cell death and mortality (Figure 6) (Wang et al., 2012; Guthrie et al., 2020; Yuan et al., 2022).

Increased mTOR signaling and protein synthesis in response to copper depletion appears to be a cell-type specific response that is observed in human SH-SY5Y neuroblastoma cells (Figure 2-5) and Purkinje cells but not granular layer cells in *Atp7a*$^{flx/Y}$ *::* *Vil1*$^{Cre/+}$ mice (Figure 6), suggesting that Purkinje cells are especially sensitive to copper depletion. CTR1 KO mouse embryonic fibroblasts were previously reported to show no changes in phosphorylation of either mTOR- or PI3K-Akt-specific substrates (Tsang et al., 2020). In Menkes disease, Purkinje cells experience rapid and specific pathology relative to other cell types and regions of the brain,

including enlarged and distended mitochondria, increased dendritic arborization, and cell death, which have been reported in both humans (Ghatak et al., 1972; Vagn-Hansen et al., 1973; Purpura et al., 1976; Hirano et al., 1977; Troost et al., 1982; Kodama et al., 2012) and various mouse models (Yamano and Suzuki, 1985; Niciu et al., 2007; Lenartowicz et al., 2015; Guthrie et al., 2020). Importantly, some of these phenotypes are recapitulated by cell-autonomous hyperactivation of mTOR; however, in contrast to Menkes disease, mTOR activation in copper-sufficient Purkinje cells *increases* the size and respiratory activity of their mitochondria (Sakai et al., 2019). Dramatic differences in the mitochondrial proteome between Purkinje cells and other cell types in the cerebellum have been reported (Fecher et al., 2019). Thus, Purkinje neurons and their mitochondria may be uniquely susceptible to copper depletion due to cell-type specific mitochondrial properties and/or abundance, as well as their dependency on mTOR signaling (Supplemental Figure S8). This is consistent with the enrichment of nuclear-encoded mitochondrial transcripts and mitochondrial activity in GABAergic neurons, particularly those expressing parvalbumin (Wynne et al., 2021; Bredvik and Ryan, 2024).

Previous reports have connected mitochondrial dysfunction with mTOR or PERK signaling. Mouse models of Leigh syndrome (caused by a deficiency in the Complex I subunit Ndufs4) and mitochondrial myopathy exhibit increased mTORC1 activity (Johnson et al., 2013; Khan et al., 2017), and downregulation of the mitochondrial respiratory complexes I, III, or IV stimulates TOR activity in the *Drosophila* wing disc (Perez-Gomez et al., 2020). Multiple diseases with impairments in mitochondrial respiration have been reported to benefit from mTOR inhibition, which is proposed to help alleviate metabolic stress. For example, rapamycin promotes survival and ameliorates pathology in a mouse model of Leigh syndrome (Johnson et al., 2013), and death due to energy stress in cells that are Coenzyme-Q-deficient is rescued by several mTORC1/2 inhibitors as well as protein synthesis inhibition by cycloheximide (Wang and Hekimi, 2021). These studies stand in contrast with our results. Our pharmacogenetic epistasis studies in CTR1 KO cells demonstrate that mTOR activation and increased protein synthesis is adaptive (Figure

4, Supplemental Figure S5) and that these cells are more sensitive to protein synthesis inhibition (Figure 5, Supplemental Figure S6). Additionally, stimulating protein synthesis in copper depleted *Drosophila* by either *S6k* overexpression or *Thor* RNAi partially rescues dendritic branching and mitochondrial phenotypes in class IV sensory neurons (Figure 7), while downregulation of *S6k*, *Akt*, or *raptor* increases the severity of copper deficiency phenotypes in the epidermis (Supplemental Figure S10). This suggests that mTOR-Raptor-S6K-dependent protein synthesis is adaptive in copper-deficient neurons and is necessary and sufficient to partially revert the effects of copper depletion in *Drosophila* (Figure 7 and Supplemental Figure S10). Based on these data and the fact that two distinct pathways favoring increased protein synthesis are activated in response to copper deficiency, we conclude that increased protein synthesis downstream of increased mTORC1 activity and/or decreased PERK represents a pro-survival response to copper depletion.

It is perhaps counterintuitive for cells to upregulate a nutrient sensing pathway like mTOR when deficient in an important micronutrient and enzyme cofactor like copper, which might be expected to decrease mTOR activity (Dennis et al., 2001). It is particularly surprising given that metabolic and mitochondrial diseases benefit from mTOR inhibition (see above). We speculate this could be a way to rectify an imbalance in proteostasis and metabolism due to copper deficiency. Impaired autophagic flux has been reported in hyperglycolytic neurons (Jimenez-Blasco et al., 2024), and as copper is required for ULK1 activity and autophagy (Tsang et al., 2020), copper deficiency may inhibit autophagy, limiting the availability of a recycled pool of amino acids for *de novo* protein synthesis or as fuel for mitochondrial respiration. Thus, mTOR activation could lead to an increase in the efficiency of protein synthesis and cell cycle progression by increasing amino acid uptake from the media, as suggested by our findings of increased mRNA for the amino acid transporters SLC7A5 and SLC3A2 in CTR1 KO cells and wild-type cells treated with the copper chelator BCS (Supplemental Figure S2), and/or by increased translation efficiency of particular RNA splice variants (Ma et al., 2008; Ma and Blenis, 2009). Increased demand for

amino acids is also consistent with a recent report that endothelial cells depleted of amino acids increase phosphorylation of eIF2α (Hamada et al., 2024). Increased levels of amino acid transporters at the cell surface may relate to the perplexing result that CTR1-null cells increase normalized respiration more than wild-type cells after the addition of fresh media (Figure 5). While CTR1 KO cells exhibit increased glycolysis and lactate levels and decreased basal and ATP-dependent respiration under baseline condition (Figures 1, 1-1), mTOR activation and the upregulation of COX17 and other chaperones for Complex IV may prime these cells to utilize nutrients such that fresh media enables increased respiration even under low serum conditions (Figure 5C2, compare the blue groups) or when treated with emetine to inhibit protein synthesis (Figure 5D2). Interestingly, while SLC7A5 is a subunit of a complex known to transport large amino acids including histidine (Kanai et al., 1998; Prasad et al., 1999; Scalise et al., 2018), it has recently been reported that copper histidinate complexes can be transported by SLC7A5 in an ATP-independent manner (Scanga et al., 2023). Thus, upregulation of SLC7A5 in CTR1 KO cells may represent a strategy to increase uptake of both copper and histidine.

A highly orchestrated and dynamic signaling network regulates metabolism, copper homeostasis, and protein synthesis in the developing brain. In this context, while we have shown that increased protein synthesis can fully or partially rescue mitochondrial and dendritic phenotypes in copper-deficient *Drosophila* neurons, an important consideration is whether this response remains adaptive over time. Neurological symptoms of Menkes disease are not apparent at birth and arise in the early neonatal period in both human (Menkes et al., 1962; Tümer and Møller, 2010; Kaler, 2011; Skjørringe et al., 2017) and mouse (Yajima and Suzuki, 1979; Iwase et al., 1996; Donsante et al., 2011; Kaler, 2011; Lenartowicz et al., 2015; Guthrie et al., 2020; Yuan et al., 2022). This suggests the existence of a development-sensitive mechanism of resilience to copper deficiency that could delay neurological phenotypes and may be causally linked to concurrent changes in brain mitochondrial metabolism and proteostasis early in life. It is possible that increased protein synthesis is a resilience mechanism in copper deficiency early in

neurodevelopment when the brain is highly glycolytic (Goyal et al., 2014; Kuzawa et al., 2014; Steiner, 2020; Oyarzábal et al., 2021; Bülow et al., 2022) and before there is a global decrease in translation (Bülow et al., 2022; Harnett et al., 2022; Castillo et al., 2023; Borisova et al., 2024). The increasing demand for copper over time (Hatori et al., 2016; Chakraborty et al., 2022) and failure of the copper-deficient brain to switch to mitochondrial respiration after birth dramatically changes the molecular landscape of the brain, which may interact with accumulating cellular stress due to impaired autophagy and redox stress to ultimately become pathological. This speculation requires additional studies comparing different timepoints in mouse models of Menkes disease but would resolve the incongruency between our results and the proven benefits of mTOR inhibition in Leigh syndrome and other mitochondrial and metabolic diseases (Johnson et al., 2013; Khan et al., 2017; Perez-Gomez et al., 2020; Wang and Hekimi, 2021).

To our knowledge, our cellular and animal models of copper depletion provide the first evidence that 1) genetic defects that impair cellular copper homeostasis simultaneously modify two signaling pathways regulating protein synthesis and 2) in which the upregulation of protein synthesis is adaptive for cell-autonomous disease phenotypes. We propose that neuronal cell pathology occurs when resilience mechanisms engaged in response to copper deficiency are outpaced by the increasing bioenergetic demands of the cell during neurodevelopment.

3.5 Materials and Methods

3.5.1 Cell lines, gene editing, and culture conditions

Human neuroblastoma SH-SY5Y cells (ATCC, CRL-2266; RRID:CVCL_0019) were grown in DMEM media (Corning, 10-013) containing 10% FBS (VWR, 97068-085) at 37°C in 10% CO_2, unless otherwise indicated. SH-SY5Y cells deficient in SLC31A1 were generated by genome editing using gRNA and Cas9 preassembled complexes by Synthego with a knock-out efficiency of 97%. The gRNAs used were UUGGUGAUCAAUACAGCUGG, which targeted transcript ENST00000374212.5 exon 3. Wild-type and mutant cells were cloned by limited dilution and

mutagenesis was confirmed by Sanger sequencing with the primer: 5'GGTGGGGGCCTAGTAGAATA. All controls represent either a single wild-type clone or a combination of two wild-type clones. All experiments used two separate mutant clones of cells (KO3 and KO20, see Supplemental Figure S1, A and B) were used to exclude clonal or off-target effects unless otherwise indicated.

3.5.2 Mouse husbandry

Animal husbandry and euthanasia was carried out as approved by the Emory University Institutional Animal Care and Use Committees. Genotyping was performed by Transnetyx using real-time PCR with the Vil1-Cre-1 Tg, Atp7a-2 WT, and Atp7a-2 FL probes.

3.5.3 Antibodies

Table 1 lists the antibodies used at the indicated concentrations for western blots and immunofluorescence.

Table 1. Antibodies

Antibody	Dilution	Catalog Number	RRID
Actin B	1:5000	Sigma-Aldrich A5441	AB_476744
ATP7A	1:500	NeuroMab 75-142	AB_10672736
CCS	1:500	ProteinTech 22802-1-AP	AB_2879172
COX17	1:500	ProteinTech 11464-1-AP	AB_2085109
COX4	1:1000	Cell Signaling 4850	AB_2085424
CTR1 (SLC31A1)	1:2000	ProteinTech 67221-1-IG	AB_2919440
DBH	1:500	Millipore AB1536	AB_2089474
DEPTOR	1:1000	Cell Signaling 11816	AB_2750575
GFAP-AF594	1:400	Cell Signaling 8152	AB_10998775
HSP90	1:1000	BD Biosciences 610418	AB_397798
mTOR	1:1000	Cell Signaling 2983	AB_2105622
mTOR pSer2448	1:1000	Cell Signaling 5536	AB_10691552
NDUFB11	1:500	Abcam ab183716	AB_2927481
OXPHOS mix	1:250	Abcam ab110412	AB_2847807

PERK (EIF2AK3)	1:1000	Cell Signaling 5683	AB_10841299
Puromycin	1:500	Sigma MABE342	AB_2737590
Raptor	1:1000	Cell Signaling 2280	AB_561245
Rictor	1:1000	Cell Signaling 2114	AB_2179963
S6K P70	1:1000	Cell Signaling 9202	AB_331676
S6K pThr389	1:1000	Cell Signaling 9234	AB_2269803
SDHA	1:1000	11998	AB_2750900
UQCRC2	1:500	Abcam ab14745	AB_2213640
Mouse IRDye 680RD	1:1000	LI-COR 926-68070	AB_10956588
mouse HRP	1:5000	A10668	AB_2534058
rabbit HRP	1:5000	G21234	AB_2536530

3.5.4 Drugs

Table 2 lists the drugs used at the indicated concentrations or concentration ranges as described in their corresponding figure legends.

Table 2. Drugs

Drug	**Source/Cat. No**	**Storage/Stock**	**Concentration range**
Elesclomol	VWR, 101758-608	1 mM, DMSO, -20C	1 nM - 1024 nM
Copper chloride	Sigma, 203149	120 mM, water, -20C	25 μM - 600 μM
BCS	Sigma, B1125	400 mM, DMSO, -20C	0.1 mM - 1.6 mM
Oligomycin	Sigma, 75351	10 mM, DMSO, -20C	1.0 μM
FCCP	Sigma, C2920	10 mM, DMSO, -20C	0.25 μM
Rotenone	Sigma, R8875	10 mM, DMSO, -20C	0.5 μM
Antimycin A	Sigma, A8674	10 mM, DMSO, -20C	0.5 μM
D-Glucose	Sigma, G8769	2.5M, 4C	10 mM
2-deoxyglucose	Sigma, D3179-1G	500 mM, Glycolysis Stress Test Media, -20C	50 mM
Emetine	Sigma, E2375	100 mM, DMSO, -20C	2 nM - 2500 nM
Puromycin	Sigma, P7255	10 mg/mL, DMSO, -20C	1 mg/mL
Insulin	Sigma, 91077C	1 mM, water, 4C	1.6 nM - 1000 nM
Torin-2	VWR, 103542-338	1 mM, DMSO, -20C	1 nM - 250 nM

Rapamycin	VWR, 101762-276	50 mM, DMSO, -20C	0.8 μM - 66 μM

3.5.5 Immunoblotting and puromycin pulse

Cells were grown in 12 or 24 well plates up to required confluency. Treatments are described in each figure. For puromycin pulse experiments, puromycin was added to the media 30 minutes before lysis to a final concentration of 1 mg/mL. The plates were placed on ice, and the cells were washed with cold phosphate-buffered saline (PBS) (Corning, 21-040-CV). Lysis buffer containing 150 mM NaCl, 10 mM HEPES, 1 mM ethylene glycol-bis(β-aminoethylether)-*N*,*N*,*N′*,*N′*-tetraacetic acid (EGTA), and 0.1 mM MgCl2, pH 7.4 (Buffer A), with 0.5% Triton X-100 (Sigma, T9284) and Complete anti-protease (Roche, 11245200) was added to each plate. For samples of interest for phosphorylated proteins, PhosSTOP phosphatase inhibitor (Roche, 04906837001) was also added to the lysis buffer. Cells were then scraped and placed in Eppendorf tubes on ice for 20 min and centrifuged at 16,100 × *g* for 10 min. The insoluble pellet was discarded, and the clarified supernatant was recovered. The Bradford Assay (Bio-Rad, 5000006) was used to determine protein concentration, and all lysates were flash frozen on dry ice and stored at -80C.

Cell lysates were reduced and denatured with Laemmli buffer (SDS and 2-mercaptoethanol) and heated for 5 min at 75C. Equivalent amounts of samples were loaded onto 4-20% Criterion gels (Bio-Rad, 5671094) for SDS-PAGE in running buffer (25 mM TRIS, 130 mM glycine, and 0.1% SDS) and transferred using the semidry transfer method with transfer buffer (48 mM TRIS, 39 mM glycine, 0.037% SDS, 20% methanol) to polyvinylidene difluoride (PVDF) membranes (Millipore, IPFL00010) unless otherwise specified in the figure legend that a nitrocellulose membrane was used (Sigma, 10600009). The membranes were incubated in TRIS-Buffered Saline (TBS: 1.36 M NaCl, 26.8 mM KCl, 247 mM TRIS) containing 5% nonfat milk and 0.05% Triton X-100 (TBST; blocking solution) for 30 min at room temperature (RT). The membrane was then rinsed thoroughly and incubated overnight with optimally diluted primary

antibody in a buffer containing PBS with 3% bovine serum albumin (BSA) and 0.2% sodium azide. The next day, membranes were rinsed in TBST and treated with horseradish peroxidase-conjugated secondary antibodies against mouse or rabbit (see Table 1) diluted 1:5000 in the blocking solution for at least 30 min at RT. The membranes were washed in TBST at least three times and probed with Western Lightning Plus ECL reagent (PerkinElmer, NEL105001EA) and exposed to GE Healthcare Hyperfilm ECL (28906839). Additional staining was repeated as described above follows stripping of blots (200 mM glycine, 13.8 mM SDS, pH 2.5).

3.5.6 Mitochondrial isolation and blue native gel electrophoresis

Starting material was two 150 mm dishes with cells at 80-90% confluency for each condition. The cells were released with trypsin and the pellet washed with PBS. Crude mitochondria were enriched according to Wieckowski xx. Briefly, cells were homogenized in isolation buffer (225 mM mannitol, 75 mM sucrose, 0.1 mM EGTA, and 30 mM Tris-HCl, pH 7.4) with 20 strokes in a Potter-Elvehjem homogenizer at 6000 rpm, 4°C. Unbroken cells and nuclei were collected by centrifugation at 600 × g for 5 min and mitochondria recovered from this supernatant by centrifugation at 7000 × g for 10 min. After one wash of this pellet, membranes were solubilized in 1.5 M aminocaproic acid, 50 mM Bis-Tris, pH 7.0, buffer with antiproteases and 4 g/g (detergent/protein) digitonin or DDM (n-dodecyl β-D-maltoside) to preserve or dissolve supercomplexes, respectively (Wittig et al., 2006; Timón-Gómez et al., 2020). Proteins were separated by blue native electrophoresis in 3-12% gradient gels (Novex, BN2011BX10) (Díaz et al., 2009; Timón-Gómez et al., 2020) using 10 mg/ml ferritin (404 and 880 kDa, Sigma F4503) and BSA (66 and 132 kDa) as molecular weight standards.

3.5.7 Cell survival and Synergy analysis

For all cell survival assays with a single drug, cells were counted using an automated Bio-Rad cell counter (Bio-Rad, TC20, 1450102) and plated in 96 well plates at 5,000-10,000 cells/well and allowed to sit overnight before drugs were added. Cells were treated with the drug

concentrations indicated in each figure and summarized in Table 2 for 72 hours with the exception of emetine, for which double the number of cells were plated and cells were treated for 24 hours. Fresh media with 10% Alamar blue (Resazurin, R&D Systems #AR002) was added to each well and after 2 hours in the incubator absorbance was measured using a microplate reader (BioTek, Synergy HT; excitation at 530–570 nm and emission maximum at 580–590 nm) using a BioTek Synergy HT microplate reader with Gen5 software 3.11. For each experiment, percent survival was calculated by subtracting the background value of an empty well with only Alamar blue and normalizing to the untreated condition for each genotype. Individual data points represent the average survival of duplicate or triplicate treatments for each concentration.

For Synergy survival assays with two drugs, cells were plated in 96 well plates, treated with drugs, and incubated with Alamar blue as described above. Concentrations used are depicted in the corresponding figures and summarized in Table 2. For each experiment, percent survival was calculated by normalizing to the untreated condition for each genotype. For experiments with fetal bovine serum, values were normalized to the 10% serum condition, equivalent to the normal growth media. Individual data points represent the average survival of single replicates for each concentration. Synergy calculations were performed using the ZIP score with the SynergyFinder engine https://synergyfinder.org/ (Yadav et al., 2015; Ianevski et al., 2022). For Torin 2-elesclomol experiments, the weighted ZIP score was used, a calculation which identifies synergy at lower drug doses with less toxicity by weighting the synergy distribution at each dose level using the proportion of responses from each drug in isolation (Ianevski et al., 2022).

3.5.8 Seahorse metabolic oximetry

Extracellular flux analysis of the Mito Stress Test was performed on the Seahorse XFe96 Analyzer (Seahorse Bioscience) following manufacturer recommendations. SH-SY5Y cells were seeded at a density of 30,000 cells/well on Seahorse XF96 V3-PS Microplates (Agilent

Technologies, 101085-004) after being trypsinized and counted (Bio-Rad TC20 automated Cell Counter) the day before the experiment. When appropriate, cells were treated with drugs in 10 cm plates before seeding in Seahorse XF96 microplates and treated overnight (see indicated times and concentrations in figure legends). XFe96 extracellular flux assay kit probes (Agilent Technologies, 102416-100) incubated with the included manufacturer calibration solution overnight at 37°C without CO_2 injection. The following day, wells were washed twice in Seahorse Mito Stress Test Media. The Mito Stress Test Media consisted of Seahorse XF base media (Agilent Technologies, 102353-100) with the addition of 2 mM L-glutamine (HyClone, SH30034.01), 1 mM sodium pyruvate (Sigma, S8636), and 10 mM D-glucose (Sigma, G8769). After the washes, cells were incubated at 37°C without CO_2 injection for 1 hour prior to the stress test. During this time, flux plate probes were loaded and calibrated. After calibration, the flux plate containing calibrant solution was exchanged for the Seahorse cell culture plate and equilibrated. Seahorse injection ports were filled with 10-fold concentrated solution of oligomycin A, FCCP, and rotenone mixed with antimycin A (see Table 2 for final testing conditions and catalog numbers). All Seahorse drugs were dissolved in DMSO and diluted in Seahorse Mito Stress Test Media for the Seahorse protocol. The flux analyzer protocol included three basal read cycles and three reads following injection of oligomycin A, FCCP, and rotenone plus antimycin A. Each read cycle included a 3-minute mix cycle followed by a 3-minute read cycle where oxygen consumption rate (OCR) and extracellular acidification rate (ECAR) were determined over time. In all experiments, OCR and ECAR readings in each well were normalized by protein concentration in the well. Cells were washed twice with phosphate buffered saline (Corning 21-040-CV) supplemented with 1 mM $MgCl_2$ and 100 µM $CaCl_2$ and lysed in Buffer A. Protein concentration was measured using the Pierce BCA Protein Assay Kit (Thermo Fisher Scientific, 23227) according to manufacturer protocol. The BCA assay absorbance was read by a BioTek Synergy HT microplate reader using Gen5 software. For data analysis of OCR and ECAR, the Seahorse Wave Software version 2.2.0.276 was used. Individual data points represent the average values

of a minimum of three replicates. Non-mitochondrial respiration was determined as the lowest OCR following injection of rotenone plus antimycin A. Basal respiration was calculated from the OCR just before oligomycin injection minus the non-mitochondrial respiration. Non-mitochondrial respiration was determined as the lowest OCR following injection of rotenone plus antimycin A. ATP-dependent respiration was calculated as the difference in OCR just before oligomycin injection to the minimum OCR following oligomycin injection but before FCCP injection. Maximal respiration was calculated as the maximum OCR of the three readings following FCCP injection minus non-mitochondrial respiration.

Extracellular flux analysis of the Glycolysis Stress Test was performed as above with the following changes. The Glycolysis Stress Test Media contained only 2 mM L-glutamine. Seahorse injection ports were filled with 10-fold concentrated solution of D-glucose, oligomycin, and 2-Deoxy-D-glucose (2-DG) (see Table 2 for final testing conditions and catalog numbers). All drugs were diluted in Seahorse Glycolysis Stress Test Media for the Seahorse protocol. Glycolysis is calculated as the difference in ECAR between the maximum rate measurements before oligomycin injection and the last rate measurement before glucose injection. Glycolytic capacity was calculated as the difference in ECAR between the maximum rate measurement after oligomycin injection and the last rate measurement before glucose injection. Glycolytic reserve was calculated as the glycolytic capacity minus glycolysis. Non-glycolytic acidification was defined as the last rate measurement prior to glucose injection.

3.5.9 Resipher

Poly-L-lysine coated Nunc 96 well (Thermo, 269787) or Falcon 96 well (Falcon, 353072) plates were seeded with 40,000 cells per well with 200 µL culture media (DMEM/10% FBS media). The following day, 150 µL of culture media was replaced with fresh, prewarmed, DMEM/10% FBS media. The Resipher sensing probe lid (Nunc Plates, NS32-N; Falcon Plates, NS32-101A) and Resipher system (Lucid Scientific, Atlanta, GA) were placed on one of the replicate plates and

incubated in a humidified, 37C, 5% CO2 incubator while data was collected. For serum switch assays, at 48 hours after starting Resipher surveillance, 150 µL of warmed, un-supplemented DMEM media was replaced 3 times in 200 µL total volume to serially dilute assay to DMEM/0.16% FBS. For emetine assays, at approximately 48 hours after beginning Resipher surveillance, 150 µL of media was replaced with warmed DMEM/10% FBS media containing DMSO vehicle (VWR, WN182) or emetine (Sigma, E2375) to bring the final concentration in the wells to 3.2e-4% DMSO and 60 nM, 120 nM, or 240 nM emetine. After approximately 24 hours of DMEM/0.16%FBS or DMEM/10% FBS with vehicle/emetine treatment, rotenone (Sigma, R8875) and antimycin A (Sigma, A8674) were diluted to 10x in un-supplemented media and added to bring the well concentration to 1 mM rotenone and 1 mM Antimycin A. After about 24 hours of rotenone/antimycin treatment, the Resipher system assay was stopped. Cell counts were performed in parallel plates by measuring protein content at 24h, 48h (at the addition of emetine/DMSO/vehicle media), and 72h (at the addition of rotenone/antimycin A) and on the final Resipher plate after respiration was stably down following the addition of rotenone and antimycin A. To determine protein concentrations, wells were washed three times with phosphate buffered saline (Corning 21-040-CV) supplemented with 1 mM MgCl2 and 100 µM CaCl2, and cells were lysed in Buffer A with Complete antiprotease. Protein concentration was measured using the Pierce BCA Protein Assay Kit (Thermo Fisher Scientific, 23227) according to manufacturer protocol. Experiments were repeated in quadruplicate. Doubling time (T_d) was estimated using the equation $N(t)=N(0)2^{t/Td}$ where N(0) is the protein at either 24 or 48h and N(t) is the protein 24h later. Accumulated cell counts were estimated by determining areas under the curve using Prism Version 10.2.2.

3.5.10 Total RNA extraction and NanoString mRNA Quantification

Cells were grown on 10 cm plates, and total RNA was extracted using the TRIzol reagent (Invitrogen, 15596026). When applicable, cells were treated with 200 µM BCS for 3 days. For

preparation of samples, all cells were washed twice in ice-cold PBS containing 0.1 mM CaCl2 and 1.0 mM MgCl2. 1 ml of TRIzol (Invitrogen, 15596026) was added to the samples and the TRIzol mixture was flash frozen and stored at -80C for a few weeks until RNA Extraction and NanoString processing was completed by the Emory Integrated Genomics Core. The Core assessed RNA quality before proceeding with the NanoString protocol. The NanoString Neuropathology gene panel kit (XT-CSO-HNROP1-12) or Metabolic Pathways Panel (XT-CSO-HMP1-12) was used for mRNA quantification. mRNA counts were normalized to either the housekeeping genes AARS or TBP, respectively, using NanoString nSolver software. Normalized data were further processed and visualized by Qlucore.

3.5.11 ICP mass spectrometry

Procedures were performed as described previously (Lane et al., 2022). Briefly, cells were plated on 10 or 15 cm dishes. After reaching desired confluency, cells were treated with 1 nM elesclomol for 24 hours. On the day of sample collection, the plates were washed three times with PBS, detached with trypsin, and neutralized with media and pelleted at 800 × g for 5 min at 4C. The cell pellet was resuspended with ice-cold PBS, aliquoted into 3-5 tubes, centrifuged at 16,100 × g for 10 min. The supernatant was aspirated, and the residual pellet was immediately frozen on dry ice and stored at -80C. Mitochondria were isolated as described above. Tissue samples were collected following euthanasia, weighed, and immediately flash frozen on dry ice. Cell or mitochondrial pellets were digested by adding 50 µL of 70% trace metal basis grade nitric acid (Millipore Sigma, 225711) followed by heating at 95C for 10 min. Tissue was digested by adding 70% nitric acid (50-75% w/v, i.e. 50 mg of tissue was digested in 100 µL of acid) and heated at 95C for 20 min, followed by the addition of an equal volume of 32% trace metal basis grade hydrogen peroxide (Millipore Sigma, 95321) and heated at 65C for 15 minutes. After cooling, 20 µL of each sample was diluted to 800 µL to a final concentration of 2% nitric acid using either 2% nitric acid or 2% nitric acid with 0.5% hydrochloric acid (VWR, RC3720-16) (vol/vol). Metal levels

were quantified using a triple quad ICP-MS instrument (Thermo Fisher, iCAP-TQ) operating in oxygen mode under standard conditions (RF power 1550 W, sample depth 5.0 mm, nebulizer flow 1.12L/min, spray chamber 3C, extraction lens 1,2 -195, –-15 V). Oxygen was used as a reaction gas (0.3 mL/min) to remove polyatomic interferences or mass shift target elements (analytes measured; 32S.16O, 63Cu, 66Zn). External calibration curves were generated using a multielemental standard (ICP-MSCAL2-1, AccuStandard, USA) and ranged from 0.5 to 1000 µg/L for each element. Scandium (10 µg/L) was used as internal standards and diluted into the sample in-line. Samples were introduced into the ICP-MS using the 2DX PrepFAST M5 autosampler (Elemental Scientific) equipped with a 250 µL loop and using the 0.25 mL precision method provided by the manufacturer. Serumnorm (Sero, Norway) was used as a standard reference material, and values for elements of interest were within 20% of the accepted value. Quantitative data analysis was conducted with Qtegra software, and values were exported to Excel for further statistical analysis.

3.5.12 Preparation of brain tissue for proteomics, immunoblots, or Luminex analysis

Brain samples were collected after euthanasia and immediately flash frozen in liquid nitrogen and stored at -80C. Brains were lysed in 8M urea in 100 µM potassium phosphate buffer (pH 8.0; 47.6 mL 1M K_2HPO_4 + 4.8 mL 1M KH_2PO_4, bring to 525 mL total volume) with Complete anti-protease and PhosSTOP phosphatase inhibitor and homogenized by sonication (Fisher Scientific, Sonic Dismembrator Model 100). After incubation on ice for 30 minutes, samples were spun at 7000 × g for 10 minutes at 4C, and the supernatant was transferred to a new tube. Protein concentration was measured in triplicate using the Pierce BCA Protein Assay Kit (Thermo Fisher Scientific, 23227) according to manufacturer protocol. Samples were stored at -80C until use.

3.5.13 TMT mass spectrometry for proteomics

Cells were grown in standard media as described above (Figure 2C, TMT1; DMEM (Corning, 10-013), 10% FBS, 25 mM D-glucose, 4 mM L-glutamine, 1 mM sodium pyruvate) or

media with dialyzed FBS supplemented with D-glucose, sodium pyruvate, and L-glutamine (Figure 2C, TMT2; DMEM (Thermo Fisher, A14430-01), 10% dialyzed FBS (Thermo Fisher, 26400-044), 10 mM D-glucose, 2 mM L-glutamine, 1 mM pyruvate). There was no difference in total cellular copper as measured by ICP-MS (not shown; manuscript in preparation containing the complete TMT2 dataset). Cells were detached with PBS-EDTA (ethylenediaminetetraacetic acid, 10 mM) and pelleted as described above for ICP-MS. The supernatant was aspirated, and the pellet was immediately frozen on dry ice and stored at -80C.

Each cell pellet was lysed in 300 uL of urea lysis buffer (8M urea, 100 mM $NaHPO_4$, pH 8.5), including 3 µL (100x stock) HALT protease and phosphatase inhibitor cocktail (Pierce). Protein supernatants were sonicated (Sonic Dismembrator, Fisher Scientific) 3 times for 5 s with 15 s intervals of rest at 30% amplitude to disrupt nucleic acids and subsequently vortexed. Protein concentration was determined by the bicinchoninic acid (BCA) method, and samples were frozen in aliquots at −80°C. Protein homogenates (100 µg) were diluted with 50 mM NH_4HCO_3 to a final concentration of 4M urea and then treated with 5 mM dithiothreitol (DTT) at 25°C for 30 minutes, followed by 10 mM iodoacetimide (IAA) at 25°C for 30 minutes in the dark. Protein was digested with 1:100 (w/w) lysyl endopeptidase (Wako) at 25°C for 2 hours and further digested overnight with 1:50 (w/w) trypsin (Promega) at 25°C. Resulting peptides were desalted with a 10mg hydrophilic-lipophilic balanced (HLB) column (Waters). An aliquot from each sample was used to create a global internal standard (GIS) and all samples were dried under vacuum. TMT labeling was performed according to the manufacturer's protocol and as described previously (Ping et al., 2018; Wynne et al., 2023). Briefly, all samples were resuspended in 100 mM triethylammonium bicarbonate (TEAB) buffer followed by the addition of anhydrous acetonitrile (ACN), and solutions were transferred to their respective channel tubes. After 1 hr, the reaction was quenched with 5% hydroxylamine and all samples were combined and dried. Dried samples were re-suspended in high pH loading buffer (0.07% vol/vol NH_4OH, 0.045% vol/vol formic acid (FA), 2% vol/vol ACN) and loaded onto a Water's Ethylene Bridged Hybrid (BEH) 1.7 µm 2.1mm by 150mm. A Thermo

Vanquish was used to carry out the fractionation. Solvent A consisted of 0.0175% (vol/vol) NH_4OH, 0.01125% (vol/vol) FA, and 2% (vol/vol) ACN; solvent B consisted of 0.0175% (vol/vol) NH_4OH, 0.01125% (vol/vol) FA, and 90% (vol/vol) ACN. The sample elution was performed over a 25 min gradient with a flow rate of 0.6 mL/min. A total of 192 individual equal volume fractions were collected across the gradient and subsequently pooled by concatenation into 96 fractions. All fractions were dried to completeness using a SpeedVac.

Each of the 96 high-pH fractions was resuspended in loading buffer (0.1% FA, 0.03% trifluoroacetic acid (TFA), 1% ACN). Peptide eluents were separated on a self-packed C18 (1.7 µm Water's BEH) fused silica column (laser pulled 15 cm × 150µM inner diameter (ID)) by Ultimate 3000 RSLCnano (Thermo Scientific). Elution was performed over a 30-min gradient at a rate of 1µL/min with buffer B ranging from 1% to 38% (buffer A: 0.1% FA in water, buffer B: 0.1 % FA in 80% ACN). Mass spectrometry was performed with a FAIMS Pro frontend equipped Orbitrap Eclipse (Thermo) in positive ion mode using data-dependent acquisition with 1.5 second top speed cycles for each FAIMS compensative voltage (CV). Each cycle consisted of one full MS scan followed by as many MS/MS events that could fit within the given 1.5 second cycle time limit. MS scans were collected at a resolution of 60,000 (410-1600 m/z range, 4x10^5 automatic gain control (AGC), 50 ms maximum ion injection time, FAIMS CV of -45 and -65). Only precursors with charge states between 2+ and 6+ were selected for MS/MS. All higher energy collision-induced dissociation (HCD) MS/MS spectra were acquired at a resolution of 30,000 (0.7 m/z isolation width, 35% collision energy, 1.25^5 AGC target, 54 ms maximum ion time, turboTMT on). Dynamic exclusion was set to exclude previously sequenced peaks for 20 seconds within a 10-ppm isolation window. MS/MS spectra were searched against the Uniprot human database (downloaded on 02/2019) with Proteome Discoverer 2.4.1.15 (Thermo Fisher Scientific). Variable and static modifications included methionine oxidation, asparagine, glutamine deamidation, protein N-terminal acetylation, cysteine carbamidomethyl, peptide N-terminus TMT, and lysine TMT. Percolator was used to filter MS/MS spectra matches false discovery rate of <1%.

Abundance calculations used only razor and unique peptides, and the ratios of sample over the GIS of normalized channel abundances were used for comparison across all samples.

3.5.14 Metabolite quantification by LC mass spectrometry

Cells were seeded in duplicate 6 wells per replicate at 100,000 or 190,000 cells per well for wild-type and CTR1 KO cells, respectively, and treated with 1 nM elesclomol for 2 days. Media was replaced with pyruvate-free media (Thermo Fisher 11966-025, supplemented with 25 mM glucose) with dialyzed FBS (Thermo Fisher 26400044) and 1 nM elesclomol and 5 μM $CuCl_2$ for 24 hours. (Media prepared with dialyzed FBS must be supplemented with copper as dialysis removes copper from the serum.) After a total of 72h elesclomol treatment, cells were washed with ice-cold PBS supplemented with 1 mM $MgCl_2$ and 100 μM $CaCl_2$ and extracted with 400 μL of lysis buffer (0.1M formic acid at 4:4:2 dilution (MeOH: ACN: Water) containing 25 μM $^{13}C_3$ alanine as an internal standard. After 2 min on ice, 35 μL of 15% NH_4HCO_3 was added, mixed well by gently swirling the plate, and incubated for another 20 min on ice. Cell lysates were then transferred into pre-chilled 1.5 ml centrifuge tubes, vortexed briefly, and spun at 21,300xg for 30 min at 4°C. 360 μL of supernatant was then transferred into pre-chilled 1.5 ml centrifuge tubes and dried down using a Savant Speedvac Plus vacuum concentrator. Samples were resuspended in 120 μL of 60:40 (ACN: Water), sonicated for 5 minutes at 4°C, and centrifuged at 21,300xg for 20 min at 4°C. 100 μL of supernatant was transferred into a pre-chilled LC-MS vial. 5 μL of this sample was injected into a HILIC-Z column (Agilent Technologies) on an Agilent 6546 QTOF mass spectrometer coupled with an Agilent 1290 Infinity II UHPLC system (Agilent Technologies). The column temperature was maintained at 15 °C and the autosampler was at 4 °C. Mobile phase A: 20 mM Ammonium Acetate, pH = 9.3 with 5 μM Medronic acid, and mobile phase B: acetonitrile. The gradient run at a flow rate of 0.4 ml/min was: 0min: 90% B, 1min 90% B, 8 min: 78% B, 12 min: 60% B, 15 min: 10% B, 18 min: 10 %B, 19-23 min: 90% B. The MS data were collected in the negative mode within an m/z = 20-1100 at 1 spectrum/sec, Gas temperature: 225

ºC, Drying Gas: 9 l/min, Nebulizer: 10 psi, Sheath gas temp: 375 ºC, Sheath Gas flow: 12 l/min, VCap: 3000V, Nozzle voltage 500 V, Fragmentor: 100V, and Skimmer: 45V. Data were analyzed using Masshunter Qualitative Analysis 10 and Masshunter Quantitative Analysis 11 (Agilent Technologies). Metabolite levels from different treatments were normalized to cell numbers.

3.5.15 Insulin receptor phosphorylation quantification

The cerebellum was isolated from mice at postnatal day 10 and flash frozen in liquid nitrogen and stored at -80C. Tissue was dissolved in 300 µL 8M urea in 100 mM PO_4 containing protease and phosphatase inhibitors, sonicated 5-10 times in 1 second bursts, and incubated on ice for 30 minutes with periodic vortexing. Samples were spun at 13,500 RCF for 10 min at 4C and the supernatant was transferred to a new tube. Protein concentration was measured in triplicate by BCA as described above. Mouse brain lysates were stored at -80°C, then thawed on ice and normalized to 1µg of total protein in Milliplex Assay buffer prior to the start of the assay protocol. We measured Tyr1135/Tyr1136 phosphosites in IGF1R with the Milliplex® MAP kit (48-611MAG) read out on a MAGPIX Luminex instrument (Luminex, Austin, TX, USA).

3.5.16 Digital spatial profiling of mouse brain tissue

Formalin-fixed paraffin-embedded mouse brain tissue was profiled using GeoMx® DSP (Merritt et al., 2020). Brains were isolated at P10 after euthanasia and immediately fixed overnight at room temperature in 10% neutral buffered formalin (Thermo Fisher 28906, diluted to 10% NBF with 0.9% sterile saline solution) at a ratio of 20:1 fixative to sample. Thin (5 µm) sagittal tissue sections were prepared on positively charged slides by the Emory University Cancer Tissue and Pathology shared resource according to manufacturer's recommendations for Semi-Automated RNA Slide Preparation Protocol (FFPE) (manual no. MAN-10151-04). Sections were air-dried at room temperature overnight and shipped to NanoString at room temperature.

Following an overnight bake at 65°C, slides underwent deparaffinization, rehydration, heat-induced epitope retrieval (for 20 minutes at 100°C with Bond Epitope Retrieval 2 Solution),

and enzymatic digestion (0.1 µg/mL proteinase K for 15 minutes at 37°C). Tissues were then incubated with 10% neutral buffered formalin for 5 minutes and 5 minutes with NBF Stop buffer. All steps following overnight baking were carried out on a Leica BOND-RX. Slides were then removed from the Leica BOND-RX and *in situ* hybridization with GeoMx® Mouse Whole Transcriptome Atlas (mWTA) probes was carried out overnight in a humidified hybridization chamber kept at 37°C. Following rounds of stringent washing with a 1:1 volumetric mixture of 4X SSC and 100% formamide to remove off-target probes, the tissue was blocked with Buffer W blocking solution (NanoString Technologies) then incubated with a mouse anti-GFAP antibody (see Table 2) and a stain for the nuclear marker Syto83.

Tissue morphology was visualized using fluorescent antibodies and Syto83 on the GeoMx® DSP instrument. Regions of interest (ROIs) were selected from the cerebellum of the samples using the polygon tool. Either a GFAP+ or GFAP- mask was generated within each ROI using the fluorescence signal associated with the GFAP antibody, and UV light was utilized to release and collect oligonucleotides from each ROI. Areas of UV light irradiation within an ROI are referred to as areas of illumination (AOI). During PCR, Illumina i5 and i7 dual-indexing primers were added to each photocleaved oligonucleotide allowing for unique indexing of each AOI. Library concentration was measured using a Qubit fluorometer (Thermo Fisher Scientific), and quality was assessed using a Bioanalyzer (Agilent). The Illumina Novaseq 6000 was used for sequencing, and the resulting FASTQ files were then processed by the NanoString DND pipeline to generate count data for each target probe in every AOI.

Quality control and preprocessing of GeoMx transcript data

The GeoMx DSP Analysis Suite was utilized for conducting both quality control (QC) and data exploration. First, each AOI was QC checked to ensure contamination was avoided during PCR and library preparation and that sequencing was sufficient. All AOIs passed QC so none were removed from downstream analysis. Next, any global outliers in the target list were identified

and removed from the panel. Finally, the dataset was normalized using third quantile (Q3) normalization. The QC checked, Q3 normalized dataset was used for downstream analysis.

3.5.17 Drosophila husbandry and genotypes

Fly strains used are listed in Table 3. All fly strains were reared at 25C on standard molasses media (Genessee Scientific) on a 12hr:12hr light:dark cycle. All fly strains were isogenized and bred into the same genetic background. For epidermis experiments (Supplemental Figure S10), flies were aged 4-7 days and imaged using an Olympus SZ-61 stereomicroscope and an Olympus DP23 color camera. Images were then stacked using Zyrene stacker. Dendritic characterization experiments were performed in both male and female flies as described previously (Hartwig et al., 2020). Briefly, virgin females from mCD8-GFP were outcrossed to male flies from individual transgenic fly lines (AKT-OE, S6K-STDETE-OE, THOR-IR, and THOR-IR2) to first determine their effects on dendritic morphology. Of the two Thor RNAi lines tested, THOR-IR was the most phenotypic and all further experiments were performed using this line. The effect of ATP7-OE was determined using the ATP7-OE;mCD8-GFP transgenic fly line. Rescue analyses were performed by outcrossing ATP7-OE;mCD8-GFP virgin female flies to male flies from the fly lines previously mentioned. For both mCD8-GFP and ATP7-OE;mCD8-GFP, CD4-tdGFP was used as control. For super-resolution imaging, UAS-mito-HA-GFP;GAL4ppk1.9,UAS-mCD8::GFP virgin female flies were outcrossed to male flies from UAS-ATP7, UAS-ATP7;UAS-S6k.STDETE, or UAS-CD4-tdTOM (control).

Table 3. *Drosophila* strains

Short name	Genotype	Source	Fig
ATP7-OE	UAS-ATP7-wt-FLAG	Gift from RB (Norgate et al., 2006)	7, S10

mCD8-GFP	UAS-mCD8::GFP	Gift from YJ (Grueber et al., 2007)	7
GAL4ppk1.9	GAL4ppk1.9	Gift from YJ (Grueber et al., 2007)	7
AKT-OE	y[1] w[1118]; P{w[+mC]=UAS-Akt.Exel}cm2	BDSC 8191	7
S6K-STDETE-OE	w[1118]; P{w[+mC]=UAS-S6k.STDETE}2	BDSC 6914	7
THOR-IR	y[1] sc[*] v[1] sev[21]; P{y[+t7.7] v[+t1.8]=TRiP.HMS01555}attP40	BDSC 36667	7
THOR-IR2	y[1] v[1]; P{y[+t7.7] v[+t1.8]=TRiP.HMS06007}attP40	BDSC 80427	-
MitoGFP	UAS-mito-HA-GFP	BDSC 8442	7
mCD8-RFP	UAS-mCD8::RFP	Gift from YJ (Grueber et al., 2003)	7
CD4-tdTOM	w[1118]; PBac{y[+mDint2] w[+mC]=UAS-CD4-tdTom}VK00033	BDSC 35837	7
CD4-tdGFP	y[1] w[*]; P{w[+mC]=UAS-CD4-tdGFP}8M2	BDSC 35839	7
Control	w1118	BDSC 5905	S10
AKT-OE	y[1] w[1118]; P{w[+mC]=UAS-Akt.Exel}2	BDSC 8191	S10
AKTRNAi	y[1] v[1]; P{y[+t7.7] v[+t1.8]=TRiP.HM04007}attP2	BDSC 31701	S10
S6K-OE	w[1118]; P{w[+mC]=UAS-S6k.M}2/CyO	BDSC 6910	S10
S6K-IR	y[1] v[1]; P{y[+t7.7] v[+t1.8]=TRiP.HMS02267}attP2	BDSC 41702	S10
RAPTOR-IR	y[1] v[1]; P{y[+t7.7] v[+t1.8]=TRiP.JF01088}attP2	BDSC 31529	S10
RICTOR-IR1	y[1] v[1]; P{y[+t7.7] v[+t1.8]=TRiP.JF01370}attP2	BDSC 31388	S10
RICTOR-IR2	y[1] sc[*] v[1] sev[21]; P{y[+t7.7] v[+t1.8]=TRiP.HMS01588}attP2	BDSC 36699	S10

pnr-GAL4	y[1] w[1118]; P{w[+mW.hs]=GawB}pnr[MD237]/TM3, P{w[+mC]=UAS-y.C}MC2, Ser[1]	BDSC 3039	S10

3.5.18 Drosophila *dendritic imaging and analysis*

Live confocal imaging was done as previously described (Hartwig et al., 2020). Neurons were imaged from wandering third-instar larvae on a Zeiss LSM780 microscope. Individual animals were placed on a microscopic slide and anesthetized by immersion in 1:5 (v/v) diethyl ether to halocarbon oil solution and covered with 22 x 50 mm coverslip. Images were acquired as z-stacks using a 20x dry objective (NA 0.8) and step size 2µm. Maximum intensity projections of the images were acquired, and the images were exported as .jpeg files using the Zen Blue software. Images were then stitched using Adobe Photoshop and manually curated using the Flyboys software to remove background noise (Das et al., 2017). The images were skeletonized and processed on ImageJ (Schneider et al., 2012; Arshadi et al., 2021) using a custom macro (https://github.com/CoxLabGSU/Drosophila_Sensory_Neuron_Quantification) to get quantitative metrics such as total dendritic length, branches, maximum intersection (Sholl), radius of maximum intersection (Sholl), and dendritic field coverage (convex hull). For proximal-distal analysis, a circular region of 400 pixels diameter from the soma was selected and considered as proximal to the soma. The region beyond 400 pixels was considered as distal. These regions were then analyzed separately. Average branch length was calculated by dividing the total dendritic length by the branches. The data obtained were then compiled using R6 (R Core Team, 2021) and exported to Excel (Microsoft).

Super-resolution imaging was performed on a Zeiss LSM980 Airyscan 2 confocal microscope on live animals. Animals were prepared as described above, and images were acquired as z-stacks using a 63x oil objective on Airyscan mode (SuperResolution:9.0 (3d, Auto)). Maximum intensity projections of the images were created using the Zen Blue software and exported as .TIFF files.

3.5.19 Data availability

The mass spectrometry proteomics data have been deposited to the ProteomeXchange Consortium via the PRIDE (Perez-Riverol et al., 2022) partner repository with the dataset identifier PXD059097.

3.5.20 Bioinformatic analyses and statistical analyses

Transcriptomics and proteomics data were processed with Qlucore Omics Explorer Version 3.6(33). Data were normalized to a variance of 1 and an average of 0 for statistical analysis and thresholding. Permutation statistical analyses were performed with the engine https://www.estimationstats.com/#/ with a two-sided permutation t-test using 5000 reshuffles (Ho et al., 2019). ANOVA and paired analyses were conducted with Prism Version 10.2.2 (341). Gene ontology studies were performed with Metascape and ENRICHR (Zhou et al., 2019).

Chapter 4. Discussion

4.1 Summary of findings

This thesis began with the overall hypothesis that neurological phenotypes in genetic forms copper deficiency are the result of an equilibrium between adaptive and maladaptive mechanisms. My work identified the first of these adaptive mechanisms in the form of increased protein synthesis dependent on the activity of mTOR and PERK. This conclusion is founded on and technical and experimental strategies described in Chapters 2 and 3.

In Chapter 2, we developed a protocol for measurement of trace elements in biological samples using ICP-MS. This technique was validated in multiple human cell lines and *Drosophila* and can detect drug treatments affecting copper levels. Normalization with sulfur or phosphorus reduces variability, minimizes human error, and streamlines sample preparation for metal quantification.

In Chapter 3, we generated a human neuroblastoma cell model in which copper deficiency was induced by KO of CTR1. In these CTR1-null cells, we observed impairments in copper-dependent mitochondrial and Golgi enzymes. Blue native gel electrophoresis and immunoblots of the respiratory chain complexes revealed specific impairments in Complex IV but not other respiratory complexes. Seahorse extracellular flux oximetry and measurement of certain key metabolites demonstrated that CTR1 KO cells alter their balance between mitochondrial respiration and glycolysis in favor of increased glycolysis, a phenotype which can be rescued by delivery of copper to the mitochondria with elesclomol.

In both CTR1 KO cells and Purkinje neurons in a presymptomatic model of Menkes disease, we observed increased mTOR activation and upregulation of protein synthesis. The CTR1 KO cell proteome and phosphoproteome were profiled by TMT-MS and RNA expression by Nanostring nCounter technology to reveal that mTORC1 signaling and downstream S6K signaling are two of the most altered ontologies in CTR1 KO cells. More granular analysis of

molecules annotated to these ontologies and confirmatory immunoblots established an upregulation in activity of both of these pathways in copper deficient cells, including dramatic decreases in DEPTOR protein and RNA and increased phosphorylation of mTOR, S6K, and RPS6. We also observed that CTR1 KO cells exhibit decreased abundance and phosphorylation of PERK (EIF2AK3). Collectively, these changes in PERK along with mTOR-S6K activity and downstream phosphorylation of RPS6 are predictive of increased protein synthesis in copper deficient cells, which we confirmed by puromycin incorporation and subsequent immunoblots. In copper-deficient Purkinje neurons in *At7pa*$^{flx/Y}$ :: *Vil1*$^{Cre/+}$ mice, we also identified an upregulation of the protein synthesis machinery. Gene set enrichment analysis identifying increased expression of genes associated with translation initiation and the formation of the 40S and 60S subunits of the ribosome in mutant Purkinje neurons. We also observed upregulation of a set of mTOR-associated genes in Purkinje neurons from mutant mice as well as increased phosphorylation of Igf1r, consistent with increased mTOR activation.

Using cell autonomous models of copper deficiency, we demonstrate that mTOR activation and increased protein synthesis are adaptive mechanisms in CTR1 KO cells and *Drosophila*. Pharmacogenomics and drug Synergy assays in CTR1 KO cells demonstrate that mTOR inhibition is more deleterious to cell survival in copper deficiency. Similarly, mitochondrial respiration is more resistant to protein synthesis inhibition with emetine in CTR1 KO cells than control cells. Dendritic phenotypes in class IV sensory neurons in *Drosophila*, including dendritic arborization and distribution of mitochondria, can be fully or partially rescued by genetically increasing protein synthesis through the mTOR pathway. Similarly, *Drosophila* epidermis phenotypes caused by copper deficiency can be partially rescued by these same genetic approaches or exacerbated by reducing protein synthesis downstream of mTOR.

Altogether, these data in three distinct model systems demonstrate increased mTOR activation and protein synthesis as an adaptive mechanism downstream of copper deficiency.

4.2 Cell type-specific responses to copper deficiency in the brain

This dissertation identifies the mTOR-S6K signaling pathway and protein synthesis as pathways that are upregulated in copper-deficient human neuroblastoma cells and reports similar findings in Purkinje neurons in the brain of a mouse model of Menkes disease. We chose to focus on Purkinje cells due to their particular sensitivity to copper deficiency in Menkes disease (see section 1.3.1); however, our preliminary analysis hints at cell-type specific copper deficiency phenotypes within the brain. For example, we report distinct changes in gene expression in the copper-deficient brain in Purkinje neurons and granular layer astrocytes. Of the 252 genes with altered expression in mutant Purkinje neurons and 400 genes in the granule cell layer ($FC \geq 1.5$, $p<0.05$), only 10 overlap and only 7 exhibit the same pattern of differential expression (decreased expression of *Erdr1*, *Napepld*, *Pcdhb7*, and *Vcam1* and increased expression of *Prss47*, *Sgpp2*, and *Slc25a47*). These cell-type specific differences in copper-deficient Purkinje neurons as compared to granule cell layer cells may be the result unique properties of Purkinje cells within the cerebellum. For example, we reported the enrichment of genes in Purkinje cells related to metabolism (both oxidative phosphorylation and glycolysis) and mTORC1 signaling as compared to astrocytes (see Chapter 3, Supplemental Fig. S8E-G). GABAergic interneurons such as Purkinje neurons are enriched in genes associated with mitochondrial activity (Wynne et al., 2021; Bredvik and Ryan, 2024), and Fecher et al. (2019) report dramatic differences in the mitochondrial proteome between Purkinje cells and other cell types in the cerebellum. In addition, Burnett et al. (2024) demonstrated that dendritic arborization in the cerebellum is impaired specifically in Purkinje neurons in a genetic mouse model with reduced phosphorylation of EIF2α, which is predicted in copper deficiency based on reduced PERK/EIF2AK3 activity in CTR1 KO cells. Altogether, this points to the particular importance of mitochondria and protein synthesis to Purkinje cell development and function.

More broadly, these data suggest that cell types with increased expression of mitochondrial and mTORC1-pathway genes may be particularly susceptible to altered protein

synthesis and/or disruption of mitochondrial functions like respiration as a result of copper deficiency or other triggers. Given the high expression of ATP7A/B in Purkinje neurons and elevation of copper in the cerebellum throughout life and in mouse and human (see section 1.2.3), it is likely that regional and cell-type specific demands for copper also play a role in the response of a particular cell type to mitochondrial dysfunction and altered proteostasis. Additional studies characterizing overall gene and protein expression across the brain will provide more information about the interaction of copper homeostasis, proteostasis, and metabolism in particular cell types within the brain and may clarify the mechanisms increasing susceptibility of Purkinje neurons to copper deficiency phenotypes.

4.3 Resilience mechanisms to copper deficiency during neurodevelopment

Our observations of upregulation of genes and/or proteins involved in protein synthesis in CTR1 KO cells and Purkinje neurons in *Atp7a*$^{flx/Y}$ :: *Vil1*$^{Cre/+}$ mice stand in contrast to the only published transcriptomics studies to date in the copper-deficient human brain or animal models of copper deficiency. Liu et al. (2005) quantified the transcriptome in the frontal lobe of the cortex and in the cerebellum of a patient with Menkes disease, reporting a *down*regulation of a number of ribosomal genes, among others, in both brain regions. Similar results were observed in a study of *atp7a*-null zebrafish larvae (Wu et al., 2023). This is contrary to what might be expected based on our evidence that increased protein synthesis is adaptive in copper deficiency (sections 3.3.4, 3.3.5, and 3.3.7) and the observed upregulation of genes associated with protein synthesis in Purkinje neurons (see section 3.3.6).

We speculate that the dichotomy between our results in the mouse cerebellum and published results in the human cerebellum or zebrafish could arise for two reasons. First, Liu et al. and Wu et al. quantified the transcriptome in bulk cerebellum or whole zebrafish, respectively, while we segmented our analysis using GFAP immunoreactivity and spatially by drawing regions of interest. Thus, cell-type specific mechanisms involved in copper deficiency, discussed in the

previous section, may have been masked in the analysis of bulk tissue. Secondly, the study by Liu et al. was performed in a single post-mortem human brain with ongoing neurodegeneration and disease pathology. We propose the intriguing possibility that mechanisms that are initially adaptive in copper deficiency may interact with key stereotypical features and aspects of neurodevelopment such that they become maladaptive over time.

As is discussed in detail in section 1.2.4, there is a characteristic switch from glycolysis to oxidative phosphorylation that occurs in the brain during neurodevelopment and specifically in neurons during differentiation, which also experience increased copper flow to the secretory pathway following differentiation. Protein synthesis is also tightly regulated in the brain during neurodevelopment, with aberrant cytoplasmic and mitochondrial protein synthesis linked to multiple neurodevelopmental disorders (Bülow et al., 2022; Castillo et al., 2023). Recent reports have determined that cortical neuron diversity is regulated in part by rates of translation at embryonic day E15.5 in mouse neocortex, including a global downregulation of ribosomal subunits (Harnett et al., 2022; Borisova et al., 2024). Between E12.5 to P0, there is a drop in ribosome number, altered ribosomal occupancy of start codons in developing neurons, and accompanying changes in expression and phosphorylation 4E-BP1 (eIF4E binding protein 1), suggesting gradual slowing of translation over time (Harnett et al., 2022). Importantly, 4E-BP1 is activated to ultimately promote translation downstream of mTOR signaling (Ma and Blenis, 2009). Collectively, this represents a highly orchestrated and dynamic signaling network regulating metabolism, copper homeostasis, and protein synthesis in the developing brain. Within this context, it is plausible that while we have demonstrated that mTOR activation and increased protein synthesis can increase resilience to copper deficiency in vitro and in vivo (see sections 3.3.4, 3.3.5, and 3.3.7), these mechanisms may become detrimental after birth and over time as neuronal cells mature. This idea is explored in a representative example in the following section.

4.3.1 Adaptive and maladaptive proteostasis in copper deficiency

For example, consider proteostasis in copper deficiency. We report increased protein synthesis in copper depletion, but the source of amino acids and purpose of this increased protein synthesis remains unknown. Impaired autophagy has been reported in hyperglycolytic neurons and is linked to copper deficiency by the requirement of copper for ULK1 activity (Tsang et al., 2020; Jimenez-Blasco et al., 2024). We have confirmed decreased autophagy by immunoblot in CTR1 KO cells (unpublished results by S. Zlatic). Thus, faced with impaired autophagy and respiratory activity, we speculate copper-deficient neurons may increase glycolysis to satisfy ATP demands and upregulate mTOR signaling to generate required proteins and provide substrates for metabolism by increasing amino acid uptake and/or translation efficiency (Ma et al., 2008; Ma and Blenis, 2009). This is consistent with the increased expression of the amino acid transporters SLC7A5 and SLC3A2 in copper-deficient CTR1 KO cells or wild-type cells treated with the copper chelator BCS. Additional support for this idea comes from Hamada et al. (2024), who reported increased phosphorylation of eIF2α in endothelial cells when depleted of amino acids. Thus, the predicted decrease in eIF2α phosphorylation in copper deficiency due to decreased activity of PERK/EIF2AK3 (which we documented in CTR1 KO cells) may be associated with increased levels of amino acids. It is also possible that impaired autophagy due to insufficient copper and aberrant elevations in glycolysis initiates a cascade by which cytoplasmic proteins are transported into the nucleus through the nuclear pore to be degraded by nuclear proteasomes, as recently reported by Park et al. (2024). While not explored in this dissertation, in the replication proteomics dataset used in Fig. 2 (TMT2, Chapter 3, section 3.3.2), we used the Enrichr engine to determine that 9 proteins annotated to the GO term Nuclear Transport (GO:0051169, p = 0.002231) had increased abundance in CTR1 KO cells as compared to wildtype cells. 8 of these upregulated proteins annotated to Postmitotic Nuclear Pore Complex (NPC) Reformation (Reactome 2022, R-HSA-9615933, p = 6.7223E-4). These conjectures need to be thoroughly vetted and tested but

are possibilities as to why copper-deficient neuroblastoma cells and presymptomatic Purkinje neurons increase or upregulate protein synthesis.

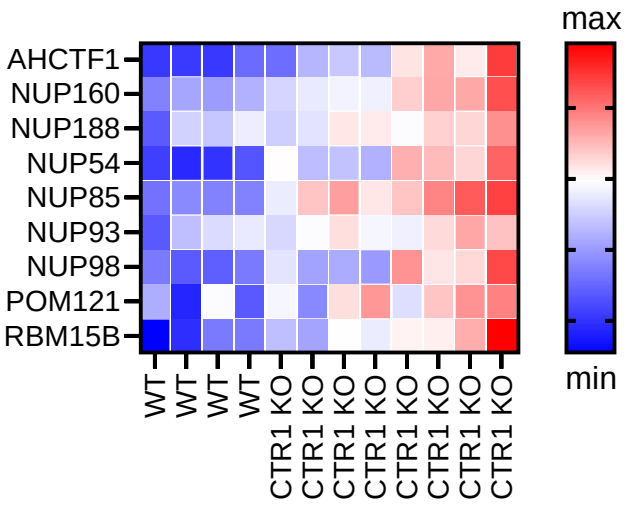

Figure 4-1. Nuclear transport protein levels in CTR1 KO cells.

Abundance of the GO term Nuclear Transport (GO:0051169, p = 0.002231) annotated proteins with differential abundance identified in CTR1 KO cells in TMT2 (see Chapter 3 section 3.3.2, Fig. 2; q<0.05, FC≥ 1.5, t-test followed by Benjamini-Hochberg FDR correction).

In this context, while we have shown that increased protein synthesis can fully or partially rescue mitochondrial and dendritic phenotypes in copper-deficient *Drosophila* neurons, an important consideration is whether this response remains adaptive over time. It is possible that increased protein synthesis is a resilience mechanism in copper deficiency early in neurodevelopment when the brain is highly glycolytic and before there is a global decrease in translation. The increasing demands of copper over time and failure of the copper-deficient brain to switch to mitochondrial respiration after birth dramatically changes the molecular landscape of the brain, which may interact with accumulating cellular stress due to impaired autophagy and redox stress to ultimately become pathological. How one could test these hypotheses is described in the following section.

4.4 Future directions for this research

Though we have documented increased protein synthesis in CTR1 KO neuroblastoma cells and speculated as to the purpose of this response to copper deficiency (section 4.3), the most direct interrogation of this question is to identify the proteins that are being synthesized. We are optimizing a technique to treat cells with a short puromycin pulse and immunoprecipitate puromycylated polypeptides to be analyzed by TMT-MS. Alternatively, SILAC (stable isotope labeling by amino acids in cell culture) can also be used to identify recently synthesized proteins. In conjunction with these experiments, similar pharmacogenomics studies blocking nuclear import (ivermectin, an importin α/β inhibitor) and proteasome inhibitors (MG132) (Park et al., 2024) alone or in combination with elesclomol or Torin-2 will clarify the interactions between copper levels and proteostasis. These results will provide context for our preliminary data that CTR1 KO cells have impaired autophagy (not shown).

The intentional choice to focus on Purkinje neurons in a mouse model of copper deficiency at a presymptomatic timepoint (postnatal day 10) enabled the identification of disease mechanisms engaged before the onset of neurodegeneration in a cell type known to be particularly impacted in Menkes disease. Additional experiments that more comprehensively assess the transcriptome across the cerebellum at P16, when mortality is observed in approximately half of copper-deficient Menkes mice and degeneration in Purkinje neurons can be detected, are currently underway. These experiments will facilitate 1) the identification of cell type-specific responses to copper deficiency throughout the cerebellum and 2) enable the comparison of the Purkinje neuron transcriptome between P10 and P16, providing clarity about the role of protein synthesis in disease pathogenesis. Additionally, we have collected cerebella at P10 and P16 in our Menkes mouse models that are heterozygous for TSC2 (*ATP7A*$^{flx/Y}$ :: *Vil1*$^{Cre/+}$ :: *TSC2*$^{+/-}$) and should exhibit elevated mTOR activity, which we plan assess by proteomics to further characterize changes in mTOR signaling and protein synthesis as the disease progresses. As mice heterozygous for TSC2 will have elevated mTOR activity, we expect these experiments

along with longitudinal measurements of mouse weight and survival to clarify whether mTOR activation is adaptive or maladaptive in this mouse model. Should TSC2-heterozygous copper-deficient mice fair more poorly than their TSC2-WT littermates, we can instead inhibit mTOR pharmacologically with brain-targeted delivery of rapamycin or Torin-2 (Khonsari et al., 2022). We are also working with collaborators to perform proteomics of the cerebellum of *ATP7A*$^{flx/Y}$ :: *Vil1*$^{Cre/+}$ mice treated with elesclomol to determine the molecular mechanisms by which copper delivery rescues animal survival. Under the conditions which best promote survival, quantification of protein synthesis by puromycin incorporation will confirm whether increased protein synthesis is observed in the brain of mouse models of Menkes disease and whether it is impacted by pharmacological or genetic manipulations of mTOR activity.

4.5 Conclusions

In this dissertation research, I tested the overall hypothesis that neurological phenotypes in genetic forms of copper deficiency are the result of an equilibrium between adaptive and maladaptive mechanisms. My work identified the first of these adaptive mechanisms in the form of increased protein synthesis downstream of altered mTOR and PERK signaling.

To our knowledge, this work contains the first proteomics study of a genetic model of copper deficiency. Additionally, our cellular and animal models of copper depletion provide the first evidence that 1) genetic defects that impair cellular copper homeostasis simultaneously modify two signaling pathways regulating protein synthesis and 2) in which the upregulation of protein synthesis is adaptive for cell-autonomous disease phenotypes. We propose that neuronal cell pathology occurs when resilience mechanisms engaged in response to copper deficiency are outpaced by the increasing bioenergetic demands of the cell during neurodevelopment.

References

Acosta-Jaquez HA, Keller JA, Foster KG, Ekim B, Soliman GA, Feener EP, Ballif BA, Fingar DC (2009) Site-specific mTOR phosphorylation promotes mTORC1-mediated signaling and cell growth. Mol Cell Biol 29:4308-4324.

Akçimen F, Lopez ER, Landers JE, Nath A, Chiò A, Chia R, Traynor BJ (2023) Amyotrophic lateral sclerosis: translating genetic discoveries into therapies. Nature Reviews Genetics 24:642-658.

Almeida LM, Pinho BR, Duchen MR, Oliveira JMA (2022) The PERKs of mitochondria protection during stress: insights for PERK modulation in neurodegenerative and metabolic diseases. Biol Rev Camb Philos Soc 97:1737-1748.

Andrade-Guerrero J, Santiago-Balmaseda A, Jeronimo-Aguilar P, Vargas-Rodríguez I, Cadena-Suárez AR, Sánchez-Garibay C, Pozo-Molina G, Méndez-Catalá CF, Cardenas-Aguayo MD, Diaz-Cintra S, Pacheco-Herrero M, Luna-Muñoz J, Soto-Rojas LO (2023) Alzheimer's Disease: An Updated Overview of Its Genetics. Int J Mol Sci 24.

Antos A, Członkowska A, Smolinski L, Bembenek J, Przybyłkowski A, Skowrońska M, Kurkowska-Jastrzębska I, Litwin T (2023) Early neurological deterioration in Wilson's disease: a systematic literature review and meta-analysis. Neurol Sci 44:3443-3455.

Arshadi C, Günther U, Eddison M, Harrington KIS, Ferreira TA (2021) SNT: a unifying toolbox for quantification of neuronal anatomy. Nat Methods 18:374-377.

Ashraf A, Michaelides C, Walker TA, Ekonomou A, Suessmilch M, Sriskanthanathan A, Abraha S, Parkes A, Parkes HG, Geraki K, So P-W (2019) Regional Distributions of Iron, Copper and Zinc and Their Relationships With Glia in a Normal Aging Mouse Model. Frontiers in Aging Neuroscience 11:351.

Atkinson DE, Walton GM (1967) Adenosine triphosphate conservation in metabolic regulation. Rat liver citrate cleavage enzyme. J Biol Chem 242:3239-3241.

Bagur R, Hajnóczky G (2017) Intracellular Ca(2+) Sensing: Its Role in Calcium Homeostasis and Signaling. Mol Cell 66:780-788.

Balcaen L, Woods G, Resano M, Vanhaecke F (2013) Accurate determination of S in organic matrices using isotope dilution ICP-MS/MS. Journal of Analytical Atomic Spectrometry 28:33-39.

Ballou LM, Lin RZ (2008) Rapamycin and mTOR kinase inhibitors. J Chem Biol 1:27-36.

Barcelo H, Stewart MJ (2002) Altering Drosophila S6 kinase activity is consistent with a role for S6 kinase in growth. Genesis 34:83-85.

Barnes N, Tsivkovskii R, Tsivkovskaia N, Lutsenko S (2005) The copper-transporting ATPases, Menkes and Wilson disease proteins, have distinct roles in adult and developing cerebellum. J Biol Chem 280:9640-9645.

Batzios S, Tal G, DiStasio AT, Peng Y, Charalambous C, Nicolaides P, Kamsteeg EJ, Korman SH, Mandel H, Steinbach PJ, Yi L, Fair SR, Hester ME, Drousiotou A, Kaler SG (2022) Newly identified disorder of copper metabolism caused by variants in CTR1, a high-affinity copper transporter. Hum Mol Genet 31:4121-4130.

Bertinato J, Iskandar M, L'Abbé MR (2003) Copper deficiency induces the upregulation of the copper chaperone for Cu/Zn superoxide dismutase in weanling male rats. J Nutr 133:28-31.

Binks T, Lye JC, Camakaris J, Burke R (2010) Tissue-specific interplay between copper uptake and efflux in Drosophila. J Biol Inorg Chem 15:621-628.

Blackman RK, Cheung-Ong K, Gebbia M, Proia DA, He S, Kepros J, Jonneaux A, Marchetti P, Kluza J, Rao PE, Wada Y, Giaever G, Nislow C (2012) Mitochondrial electron transport is the cellular target of the oncology drug elesclomol. PLoS One 7:e29798.

Borisova E et al. (2024) Protein translation rate determines neocortical neuron fate. Nature Communications 15:4879.

Boulet A, Vest KE, Maynard MK, Gammon MG, Russell AC, Mathews AT, Cole SE, Zhu X, Phillips CB, Kwong JQ, Dodani SC, Leary SC, Cobine PA (2018) The mammalian phosphate carrier SLC25A3 is a mitochondrial copper transporter required for cytochrome c oxidase biogenesis. J Biol Chem 293:1887-1896.

Brady DC, Crowe MS, Turski ML, Hobbs GA, Yao X, Chaikuad A, Knapp S, Xiao K, Campbell SL, Thiele DJ, Counter CM (2014) Copper is required for oncogenic BRAF signalling and tumorigenesis. Nature 509:492-496.

Brand AH, Perrimon N (1993) Targeted gene expression as a means of altering cell fates and generating dominant phenotypes. Development 118:401-415.

Bredvik K, Ryan TA (2024) Differential Control of Inhibitory and Excitatory Nerve Terminal Function by Mitochondria. bioRxiv:2024.2005.2019.594864.

Büchler P, Reber HA, Büchler M, Shrinkante S, Büchler MW, Friess H, Semenza GL, Hines OJ (2003) Hypoxia-inducible factor 1 regulates vascular endothelial growth factor expression in human pancreatic cancer. Pancreas 26:56-64.

Bülow P, Patgiri A, Faundez V (2022) Mitochondrial Protein Synthesis and the Bioenergetic Cost of Neurodevelopment. iScience 45:283-296.

Burnett PE, Barrow RK, Cohen NA, Snyder SH, Sabatini DM (1998) RAFT1 phosphorylation of the translational regulators p70 S6 kinase and 4E-BP1. Proc Natl Acad Sci U S A 95:1432-1437.

Burnett SB, Culver AM, Simon TA, Rowson T, Frederick K, Palmer K, Murray SA, Davis SW, Patel RC (2024) A frameshift mutation in the murine Prkra gene exhibits cerebellar abnormality and reduced eIF2α phosphorylation. Dis Model Mech 17.

Cabrera A, Alonzo E, Sauble E, Chu YL, Nguyen D, Linder MC, Sato DS, Mason AZ (2008) Copper binding components of blood plasma and organs, and their responses to influx of large doses of (65)Cu, in the mouse. Biometals 21:525-543.

Cai W, Sakaguchi M, Kleinridders A, Gonzalez-Del Pino G, Dreyfuss JM, O'Neill BT, Ramirez AK, Pan H, Winnay JN, Boucher J, Eck MJ, Kahn CR (2017) Domain-dependent effects of insulin and IGF-1 receptors on signalling and gene expression. Nat Commun 8:14892.

Calabresi P, Mechelli A, Natale G, Volpicelli-Daley L, Di Lazzaro G, Ghiglieri V (2023) Alpha-synuclein in Parkinson's disease and other synucleinopathies: from overt neurodegeneration back to early synaptic dysfunction. Cell death & disease 14:176.

Cao Y, Feng J, Tang L, Yu C, Mo G, Deng B (2020) A highly efficient introduction system for single cell- ICP-MS and its application to detection of copper in single human red blood cells. Talanta 206:120174.

Carballo-Carbajal I, Laguna A, Romero-Giménez J, Cuadros T, Bové J, Martinez-Vicente M, Parent A, Gonzalez-Sepulveda M, Peñuelas N, Torra A, Rodríguez-Galván B, Ballabio A, Hasegawa T, Bortolozzi A, Gelpi E, Vila M (2019) Brain tyrosinase overexpression implicates age-dependent neuromelanin production in Parkinson's disease pathogenesis. Nat Commun 10:973.

Carmona A, Carboni E, Gomes LC, Roudeau S, Maass F, Lenz C, Ortega R, Lingor P (2024) Metal dyshomeostasis in the substantia nigra of patients with Parkinson's disease or multiple sclerosis. J Neurochem 168:128-141.

Casimir P, Iwata R, Vanderhaeghen P (2024) Linking mitochondria metabolism, developmental timing, and human brain evolution. Curr Opin Genet Dev 86:102182.

Castillo PE, Jung H, Klann E, Riccio A (2023) Presynaptic Protein Synthesis in Brain Function and Disease. The Journal of Neuroscience 43:7483.

Chakraborty K, Kar S, Rai B, Bhagat R, Naskar N, Seth P, Gupta A, Bhattacharjee A (2022) Copper dependent ERK1/2 phosphorylation is essential for the viability of neurons and not glia. Metallomics 14.

Cheng SW, Fryer LG, Carling D, Shepherd PR (2004) Thr2446 is a novel mammalian target of rapamycin (mTOR) phosphorylation site regulated by nutrient status. J Biol Chem 279:15719-15722.

Chiang GG, Abraham RT (2005) Phosphorylation of mammalian target of rapamycin (mTOR) at Ser-2448 is mediated by p70S6 kinase. J Biol Chem 280:25485-25490.

Cobine PA, Brady DC (2022) Cuproptosis: Cellular and molecular mechanisms underlying copper-induced cell death. Mol Cell 82:1786-1787.

Cobine PA, Moore SA, Leary SC (2021) Getting out what you put in: Copper in mitochondria and its impacts on human disease. Biochim Biophys Acta Mol Cell Res 1868:118867.

Colledge M, Snyder EM, Crozier RA, Soderling JA, Jin Y, Langeberg LK, Lu H, Bear MF, Scott JD (2003) Ubiquitination regulates PSD-95 degradation and AMPA receptor surface expression. Neuron 40:595-607.

Comstra H, Faundez V (2017) Molecular Genetics of Menkes Disease. In: eLS, pp 1-6.

Comstra HS, McArthy J, Rudin-Rush S, Hartwig C, Gokhale A, Zlatic SA, Blackburn JB, Werner E, Petris M, D'Souza P, Panuwet P, Barr DB, Lupashin V, Vrailas-Mortimer A, Faundez V (2017) The interactome of the copper transporter ATP7A belongs to a network of neurodevelopmental and neurodegeneration factors. eLife 6:e24722.

Copp J, Manning G, Hunter T (2009) TORC-specific phosphorylation of mammalian target of rapamycin (mTOR): phospho-Ser2481 is a marker for intact mTOR signaling complex 2. Cancer Res 69:1821-1827.

Corona JC, Duchen MR (2016) PPARγ as a therapeutic target to rescue mitochondrial function in neurological disease. Free Radic Biol Med 100:153-163.

Covarrubias AJ, Aksoylar HI, Yu J, Snyder NW, Worth AJ, Iyer SS, Wang J, Ben-Sahra I, Byles V, Polynne-Stapornkul T, Espinosa EC, Lamming D, Manning BD, Zhang Y, Blair IA, Horng T (2016) Akt-mTORC1 signaling regulates Acly to integrate metabolic input to control of macrophage activation. Elife 5.

Culotta VC, Yang M, O'Halloran TV (2006) Activation of superoxide dismutases: Putting the metal to the pedal. Biochimica et Biophysica Acta (BBA) - Molecular Cell Research 1763:747-758.

Członkowska A, Litwin T, Dusek P, Ferenci P, Lutsenko S, Medici V, Rybakowski JK, Weiss KH, Schilsky ML (2018) Wilson disease. Nat Rev Dis Primers 4:21.

Dame C, Horn D, Schomburg L, Grünhagen J, Chillon TS, Tietze A, Vogt A, Bührer C (2022) Fatal congenital copper transport defect caused by a homozygous likely pathogenic variant of SLC31A1. Clin Genet 103:585-589.

Das R, Bhattacharjee S, Patel AA, Harris JM, Bhattacharya S, Letcher JM, Clark SG, Nanda S, Iyer EPR, Ascoli GA, Cox DN (2017) Dendritic Cytoskeletal Architecture Is Modulated by Combinatorial Transcriptional Regulation in Drosophila melanogaster. Genetics 207:1401-1421.

Davies KM, Hare DJ, Cottam V, Chen N, Hilgers L, Halliday G, Mercer JF, Double KL (2013) Localization of copper and copper transporters in the human brain. Metallomics 5:43-51.

Davies KM, Bohic S, Carmona A, Ortega R, Cottam V, Hare DJ, Finberg JP, Reyes S, Halliday GM, Mercer JF, Double KL (2014) Copper pathology in vulnerable brain regions in Parkinson's disease. Neurobiol Aging 35:858-866.

Decalf J, Albert ML, Ziai J (2019) New tools for pathology: a user's review of a highly multiplexed method for in situ analysis of protein and RNA expression in tissue. J Pathol 247:650-661.

Dennis PB, Jaeschke A, Saitoh M, Fowler B, Kozma SC, Thomas G (2001) Mammalian TOR: a homeostatic ATP sensor. Science 294:1102-1105.

Díaz F, Barrientos A, Fontanesi F (2009) Evaluation of the mitochondrial respiratory chain and oxidative phosphorylation system using blue native gel electrophoresis. Curr Protoc Hum Genet Chapter 19:Unit19.14.

Diez Fernández S, Sugishama N, Ruiz Encinar J, Sanz-Medel A (2012) Triple quad ICPMS (ICPQQQ) as a new tool for absolute quantitative proteomics and phosphoproteomics. Anal Chem 84:5851-5857.

Domart F, Cloetens P, Roudeau S, Carmona A, Verdier E, Choquet D, Ortega R (2020) Correlating STED and synchrotron XRF nano-imaging unveils cosegregation of metals and cytoskeleton proteins in dendrites. Elife 9.

Donsante A, Yi L, Zerfas PM, Brinster LR, Sullivan P, Goldstein DS, Prohaska J, Centeno JA, Rushing E, Kaler SG (2011) ATP7A gene addition to the choroid plexus results in long-term rescue of the lethal copper transport defect in a Menkes disease mouse model. Mol Ther 19:2114-2123.

Dusek P, Litwin T, Członkowska A (2019) Neurologic impairment in Wilson disease. Ann Transl Med 7:S64.

El Meskini R, Cline LB, Eipper BA, Ronnett GV (2005) The Developmentally Regulated Expression of Menkes Protein ATP7A Suggests a Role in Axon Extension and Synaptogenesis. Developmental Neuroscience 27:333-348.

El Meskini R, Crabtree KL, Cline LB, Mains RE, Eipper BA, Ronnett GV (2007) ATP7A (Menkes protein) functions in axonal targeting and synaptogenesis. Mol Cell Neurosci 34:409-421.

Ellison G, Hollings AL, Hackett MJ (2022) A review of the "metallome" within neurons and glia, as revealed by elemental mapping of brain tissue. BBA Adv 2:100038.

Fatjó-Vilas M, Papiol S, Estrada G, Bombín I, Peralta V, Rosa A, Parellada M, Miret S, Martín M, Lázaro L, Campanera S, Muñoz MJ, Lera-Miguel S, Arias B, Navarro ME, Castro-Fornieles J, Cuesta MJ, Arango C, Fañanás L (2011) Dysbindin-1 gene contributes differentially to early- and adult-onset forms of functional psychosis. Am J Med Genet B Neuropsychiatr Genet 156b:322-333.

Fecher C, Trovò L, Müller SA, Snaidero N, Wettmarshausen J, Heink S, Ortiz O, Wagner I, Kühn R, Hartmann J, Karl RM, Konnerth A, Korn T, Wurst W, Merkler D, Lichtenthaler SF, Perocchi F, Misgeld T (2019) Cell-type-specific profiling of brain mitochondria reveals functional and molecular diversity. Nature Neuroscience 22:1731-1742.

Festa RA, Thiele DJ (2011) Copper: an essential metal in biology. Curr Biol 21:R877-R883.

Fu S, Jiang W, Zheng W (2015) Age-dependent increase of brain copper levels and expressions of copper regulatory proteins in the subventricular zone and choroid plexus. Frontiers in Molecular Neuroscience 8:22.

Fujii T, Ito M, Tsuda H, Mikawa H (1990) Biochemical study on the critical period for treatment of the mottled brindled mouse. J Neurochem 55:885-889.

Fujisawa C, Kodama H, Sato Y, Mimaki M, Yagi M, Awano H, Matsuo M, Shintaku H, Yoshida S, Takayanagi M, Kubota M, Takahashi A, Akasaka Y (2022) Early clinical signs and treatment of Menkes disease. Mol Genet Metab Rep 31:100849.

Gaier ED, Miller MB, Ralle M, Aryal D, Wetsel WC, Mains RE, Eipper BA (2013) Peptidylglycine α-amidating monooxygenase heterozygosity alters brain copper handling with region specificity. J Neurochem 127:605-619.

Gale J, Aizenman E (2024) The physiological and pathophysiological roles of copper in the nervous system. Eur J Neurosci 60:3505-3543.

Galler T, Lebrun V, Raibaut L, Faller P, Wezynfeld NE (2020) How trimerization of CTR1 N-terminal model peptides tunes Cu-binding and redox-chemistry. Chem Commun (Camb) 56:12194-12197.

Ganio K, James SA, Hare DJ, Roberts BR, McColl G (2016) Accurate biometal quantification per individual Caenorhabditis elegans. Analyst 141:1434-1439.

Garza NM, Zulkifli M, Gohil VM (2022a) Elesclomol elevates cellular and mitochondrial iron levels by delivering copper to the iron import machinery. J Biol Chem 298:102139.

Garza NM, Swaminathan AB, Maremanda KP, Zulkifli M, Gohil VM (2022b) Mitochondrial copper in human genetic disorders. Trends Endocrinol Metab 34:21-33.

Ghatak NR, Hirano A, Poon TP, French JH (1972) Trichopoliodystrophy. II. Pathological changes in skeletal muscle and nervous system. Arch Neurol 26:60-72.

Ghosh A, Trivedi PP, Timbalia SA, Griffin AT, Rahn JJ, Chan SSL, Gohil VM (2014) Copper supplementation restores cytochrome c oxidase assembly defect in a mitochondrial disease model of COA6 deficiency. Human Molecular Genetics 23:3596-3606.

Gokhale A, Vrailas-Mortimer A, Larimore J, Comstra HS, Zlatic SA, Werner E, Manvich DF, Iuvone PM, Weinshenker D, Faundez V (2015) Neuronal copper homeostasis susceptibility by genetic defects in dysbindin, a schizophrenia susceptibility factor. Hum Mol Genet 24:5512-5523.

Gokhale A, Hartwig C, Freeman AH, Das R, Zlatic SA, Vistein R, Burch A, Carrot G, Lewis AF, Nelms S, Dickman DK, Puthenveedu MA, Cox DN, Faundez V (2016) The Proteome of BLOC-1 Genetic Defects Identifies the Arp2/3 Actin Polymerization Complex to Function Downstream of the Schizophrenia Susceptibility Factor Dysbindin at the Synapse. J Neurosci 36:12393-12411.

Goyal Manu S, Hawrylycz M, Miller Jeremy A, Snyder Abraham Z, Raichle Marcus E (2014) Aerobic Glycolysis in the Human Brain Is Associated with Development and Neotenous Gene Expression. Cell Metabolism 19:49-57.

Grasso M, Bond GJ, Kim YJ, Boyd S, Matson Dzebo M, Valenzuela S, Tsang T, Schibrowsky NA, Alwan KB, Blackburn NJ, Burslem GM, Wittung-Stafshede P, Winkler DD, Marmorstein R, Brady DC (2021) The copper chaperone CCS facilitates copper binding to MEK1/2 to promote kinase activation. J Biol Chem 297:101314.

Grist SM, Chrostowski L, Cheung KC (2010) Optical oxygen sensors for applications in microfluidic cell culture. Sensors (Basel) 10:9286-9316.

Grollman AP (1966) Structural basis for inhibition of protein synthesis by emetine and cycloheximide based on an analogy between ipecac alkaloids and glutarimide antibiotics. Proc Natl Acad Sci U S A 56:1867-1874.

Grueber WB, Jan LY, Jan YN (2003) Different Levels of the Homeodomain Protein Cut Regulate Distinct Dendrite Branching Patterns of Drosophila Multidendritic Neurons. Cell 112:805-818.

Grueber WB, Ye B, Yang CH, Younger S, Borden K, Jan LY, Jan YN (2007) Projections of Drosophila multidendritic neurons in the central nervous system: links with peripheral dendrite morphology. Development 134:55-64.

Guthrie LM, Soma S, Yuan S, Silva A, Zulkifli M, Snavely TC, Greene HF, Nunez E, Lynch B, De Ville C, Shanbhag V, Lopez FR, Acharya A, Petris MJ, Kim B-E, Gohil VM, Sacchettini JC (2020) Elesclomol alleviates Menkes pathology and mortality by escorting Cu to cuproenzymes in mice. Science 368:620.

Hamada Y, Masuda T, Ito S, Ohtsuki S (2024) Regulatory Role of eIF2αK4 in Amino Acid Transporter Expression in Mouse Brain Capillary Endothelial Cells. Pharm Res 41:2213-2223.

Hare DJ, Grubman A, Ryan TM, Lothian A, Liddell JR, Grimm R, Matsuda T, Doble PA, Cherny RA, Bush AI, White AR, Masters CL, Roberts BR (2013) Profiling the iron, copper and zinc content in primary neuron and astrocyte cultures by rapid online quantitative size exclusion chromatography-inductively coupled plasma-mass spectrometry. Metallomics 5:1656-1662.

Harnett D, Ambrozkiewicz MC, Zinnall U, Rusanova A, Borisova E, Drescher AN, Couce-Iglesias M, Villamil G, Dannenberg R, Imami K, Münster-Wandowski A, Fauler B, Mielke T, Selbach M, Landthaler M, Spahn CMT, Tarabykin V, Ohler U, Kraushar ML (2022) A critical period of translational control during brain development at codon resolution. Nat Struct Mol Biol 29:1277-1290.

Hartwig C et al. (2020) Golgi-Dependent Copper Homeostasis Sustains Synaptic Development and Mitochondrial Content. J Neurosci 41:215-233.

Hatori Y, Yan Y, Schmidt K, Furukawa E, Hasan NM, Yang N, Liu CN, Sockanathan S, Lutsenko S (2016) Neuronal differentiation is associated with a redox-regulated increase of copper flow to the secretory pathway. Nat Commun 7:10640.

Hirano A, Llena JF, French JH, Ghatak NR (1977) Fine structure of the cerebellar cortex in Menkes Kinky-hair disease. X-chromosome-linked copper malabsorption. Arch Neurol 34:52-56.

Ho J, Tumkaya T, Aryal S, Choi H, Claridge-Chang A (2019) Moving beyond P values: data analysis with estimation graphics. Nature Methods 16:565-566.

Hodgkinson VL, Zhu S, Wang Y, Ladomersky E, Nickelson K, Weisman GA, Lee J, Gitlin JD, Petris MJ (2015) Autonomous requirements of the Menkes disease protein in the nervous system. Am J Physiol Cell Physiol 309:C660-C668.

Holz MK, Blenis J (2005) Identification of S6 kinase 1 as a novel mammalian target of rapamycin (mTOR)-phosphorylating kinase. J Biol Chem 280:26089-26093.

Horn D, Barrientos A (2008) Mitochondrial copper metabolism and delivery to cytochrome c oxidase. IUBMB Life 60:421-429.

Hsieh SI, Castruita M, Malasarn D, Urzica E, Erde J, Page MD, Yamasaki H, Casero D, Pellegrini M, Merchant SS, Loo JA (2013) The proteome of copper, iron, zinc, and manganese micronutrient deficiency in Chlamydomonas reinhardtii. Mol Cell Proteomics 12:65-86.

Huang R, Grishagin I, Wang Y, Zhao T, Greene J, Obenauer JC, Ngan D, Nguyen DT, Guha R, Jadhav A, Southall N, Simeonov A, Austin CP (2019) The NCATS BioPlanet - An Integrated Platform for Exploring the Universe of Cellular Signaling Pathways for Toxicology, Systems Biology, and Chemical Genomics. Front Pharmacol 10:445.

Hughes DT, Halliday M, Smith HL, Verity NC, Molloy C, Radford H, Butcher AJ, Mallucci GR (2020) Targeting the kinase insert loop of PERK selectively modulates PERK signaling without systemic toxicity in mice. Sci Signal 13.

Hwang JE, de Bruyne M, Warr CG, Burke R (2014) Copper overload and deficiency both adversely affect the central nervous system of Drosophila. Metallomics 6:2223-2229.

Ianevski A, Giri AK, Aittokallio T (2022) SynergyFinder 3.0: an interactive analysis and consensus interpretation of multi-drug synergies across multiple samples. Nucleic Acids Research 50:W739-W743.

Iverson TM, Singh PK, Cecchini G (2023) An evolving view of complex II-noncanonical complexes, megacomplexes, respiration, signaling, and beyond. J Biol Chem 299:104761.

Iwase T, Nishimura M, Sugimura H, Igarashi H, Ozawa F, Shinmura K, Suzuki M, Tanaka M, Kino I (1996) Localization of Menkes gene expression in the mouse brain; its association with neurological manifestations in Menkes model mice. Acta Neuropathol 91:482-488.

Iwata R, Vanderhaeghen P (2024) Metabolic mechanisms of species-specific developmental tempo. Dev Cell 59:1628-1639.

Iwata R et al. (2023) Mitochondria metabolism sets the species-specific tempo of neuronal development. Science 0:eabn4705.

Jimenez-Blasco D, Agulla J, Lapresa R, Garcia-Macia M, Bobo-Jimenez V, Garcia-Rodriguez D, Manjarres-Raza I, Fernandez E, Jeanson Y, Khoury S, Portais JC, Padro D, Ramos-Cabrer P, Carmeliet P, Almeida A, Bolaños JP (2024) Weak neuronal glycolysis sustains cognition and organismal fitness. Nat Metab 6:1253-1267.

Johnson SC, Yanos ME, Kayser EB, Quintana A, Sangesland M, Castanza A, Uhde L, Hui J, Wall VZ, Gagnidze A, Oh K, Wasko BM, Ramos FJ, Palmiter RD, Rabinovitch PS, Morgan PG, Sedensky MM, Kaeberlein M (2013) mTOR inhibition alleviates mitochondrial disease in a mouse model of Leigh syndrome. Science 342:1524-1528.

Kaler SG (2011) ATP7A-related copper transport diseases-emerging concepts and future trends. Nat Rev Neurol 7:15-29.

Kaler SG, Ferreira CR, Yam LS (2020) Estimated birth prevalence of Menkes disease and ATP7A-related disorders based on the Genome Aggregation Database (gnomAD). Mol Genet Metab Rep 24:100602.

Kaler SG, Holmes CS, Goldstein DS, Tang J, Godwin SC, Donsante A, Liew CJ, Sato S, Patronas N (2008) Neonatal diagnosis and treatment of Menkes disease. The New England journal of medicine 358:605-614.

Kanai Y, Segawa H, Miyamoto K-i, Uchino H, Takeda E, Endou H (1998) Expression Cloning and Characterization of a Transporter for Large Neutral Amino Acids Activated by the Heavy Chain of 4F2 Antigen (CD98)*. Journal of Biological Chemistry 273:23629-23632.

Kang S, Xiao G, Ren D, Zhang Z, Le N, Trentalange M, Gupta S, Lin H, Bondarenko PV (2014) Proteomics analysis of altered cellular metabolism induced by insufficient copper level. J Biotechnol 189:15-26.

Karabasheva D, Smyth JT (2020) Preparation of Drosophila Larval and Pupal Testes for Analysis of Cell Division in Live, Intact Tissue. J Vis Exp:e60961.

Khan NA, Nikkanen J, Yatsuga S, Jackson C, Wang L, Pradhan S, Kivelä R, Pessia A, Velagapudi V, Suomalainen A (2017) mTORC1 Regulates Mitochondrial Integrated Stress Response and Mitochondrial Myopathy Progression. Cell Metabolism 26:419-428.e415.

Khonsari F, Heydari M, Dinarvand R, Sharifzadeh M, Atyabi F (2022) Brain targeted delivery of rapamycin using transferrin decorated nanostructured lipid carriers. Bioimpacts 12:21-32.

Kim BE, Turski ML, Nose Y, Casad M, Rockman HA, Thiele DJ (2010) Cardiac copper deficiency activates a systemic signaling mechanism that communicates with the copper acquisition and storage organs. Cell Metab 11:353-363.

Kim YM, Jung CH, Seo M, Kim EK, Park JM, Bae SS, Kim DH (2015) mTORC1 phosphorylates UVRAG to negatively regulate autophagosome and endosome maturation. Mol Cell 57:207-218.

Kirshner JR, He S, Balasubramanyam V, Kepros J, Yang CY, Zhang M, Du Z, Barsoum J, Bertin J (2008) Elesclomol induces cancer cell apoptosis through oxidative stress. Mol Cancer Ther 7:2319-2327.

Kirsipuu T, Zadorožnaja A, Smirnova J, Friedemann M, Plitz T, Tõugu V, Palumaa P (2020) Copper(II)-binding equilibria in human blood. Scientific Reports 10:5686.

Kodama H, Fujisawa C, Bhadhprasit W (2012) Inherited copper transport disorders: biochemical mechanisms, diagnosis, and treatment. Curr Drug Metab 13:237-250.

Korotkevich G, Sukhov V, Sergushichev A (2019) Fast gene set enrichment analysis. bioRxiv:060012.

Kozareva V, Martin C, Osorno T, Rudolph S, Guo C, Vanderburg C, Nadaf N, Regev A, Regehr WG, Macosko E (2021) A transcriptomic atlas of mouse cerebellar cortex comprehensively defines cell types. Nature 598:214-219.

Kühlbrandt W (2015) Structure and function of mitochondrial membrane protein complexes. BMC Biology 13:89.

Kuzawa CW, Chugani HT, Grossman LI, Lipovich L, Muzik O, Hof PR, Wildman DE, Sherwood CC, Leonard WR, Lange N (2014) Metabolic costs and evolutionary implications of human brain development. Proceedings of the National Academy of Sciences 111:13010-13015.

Lambert R, Srodulski S, Peng X, Margulies KB, Despa F, Despa S (2015) Intracellular Na+ Concentration ([Na+]i) Is Elevated in Diabetic Hearts Due to Enhanced Na+–Glucose Cotransport. Journal of the American Heart Association 4:e002183.

Lane A, Gokhale A, Werner E, Roberts A, Freeman A, Roberts B, Faundez V (2022) Sulfur- and phosphorus-standardized metal quantification of biological specimens using inductively coupled plasma mass spectrometry. STAR Protocols 3:101334.

Lee CE, Singleton KS, Wallin M, Faundez V (2020) Rare Genetic Diseases: Nature's Experiments on Human Development. iScience 23:101123.

Lee J, Prohaska JR, Thiele DJ (2001) Essential role for mammalian copper transporter Ctr1 in copper homeostasis and embryonic development. Proc Natl Acad Sci U S A 98:6842-6847.

Lenartowicz M, Krzeptowski W, Lipiński P, Grzmil P, Starzyński R, Pierzchała O, Møller LB (2015) Mottled Mice and Non-Mammalian Models of Menkes Disease. Frontiers in Molecular Neuroscience 8.

Levenson CW, Janghorbani M (1994) Long-term measurement of organ copper turnover in rats by continuous feeding of a stable isotope. Anal Biochem 221:243-249.

Li L, Tai Z, Liu W, Luo Y, Wu Y, Lin S, Liu M, Gao B, Liu J-X (2023) Copper overload impairs hematopoietic stem and progenitor cell proliferation via prompting HSF1/SP1 aggregation and the subsequently downregulating FOXM1-Cytoskeleton axis. iScience 26:106406.

Liberzon A, Subramanian A, Pinchback R, Thorvaldsdóttir H, Tamayo P, Mesirov JP (2011) Molecular signatures database (MSigDB) 3.0. Bioinformatics 27:1739-1740.

Lijnen P, M'Buyamba-Kabangu J-R, Fagard RH, Groeseneken DR, Staessen JA, Amery AK (1984) Intracellular Concentration and Transmembrane Fluxes of Sodium and Potassium in Erythrocytes of White Normal Male Subjects With and Without a Family History of Hypertension. Journal of Hypertension 2.

Lin C, Zhang Z, Wang T, Chen C, James Kang Y (2015) Copper uptake by DMT1: a compensatory mechanism for CTR1 deficiency in human umbilical vein endothelial cells. Metallomics 7:1285-1289.

Linder MC (1991) Biochemistry of Copper: Springer New York, NY.

Linder MC (2016) Ceruloplasmin and other copper binding components of blood plasma and their functions: an update. Metallomics 8:887-905.

Linder MC, Hazegh-Azam M (1996) Copper biochemistry and molecular biology. Am J Clin Nutr 63:797s-811s.

Litwin T, Dušek P, Członkowska A (2017) Symptomatic treatment of neurologic symptoms in Wilson disease. Handb Clin Neurol 142:211-223.

Liu GY, Sabatini DM (2020) mTOR at the nexus of nutrition, growth, ageing and disease. Nat Rev Mol Cell Biol 21:183-203.

Liu P-C, Chen Y-W, Centeno JA, Quezado M, Lem K, Kaler SG (2005) Downregulation of myelination, energy, and translational genes in Menkes disease brain. Molecular Genetics and Metabolism 85:291-300.

Liu P-P, Xie Y, Meng X-Y, Kang J-S (2019) History and progress of hypotheses and clinical trials for Alzheimer's disease. Signal Transduction and Targeted Therapy 4:29.

Loeffler DA, LeWitt PA, Juneau PL, Sima AAF, Nguyen HU, DeMaggio AJ, Brickman CM, Brewer GJ, Dick RD, Troyer MD, Kanaley L (1996) Increased regional brain concentrations of ceruloplasmin in neurodegenerative disorders. Brain Research 738:265-274.

Lothian A, Roberts BR (2016) Standards for Quantitative Metalloproteomic Analysis Using Size Exclusion ICP-MS. J Vis Exp:e53737.

Lutsenko S, Roy S, Tsvetkov P (2024) Mammalian Copper Homeostasis: Physiologic Roles and Molecular Mechanisms. Physiol Rev 105:441-491.

Ma XM, Blenis J (2009) Molecular mechanisms of mTOR-mediated translational control. Nat Rev Mol Cell Biol 10:307-318.

Ma XM, Yoon SO, Richardson CJ, Jülich K, Blenis J (2008) SKAR links pre-mRNA splicing to mTOR/S6K1-mediated enhanced translation efficiency of spliced mRNAs. Cell 133:303-313.

Magnuson B, Ekim B, Fingar DC (2012) Regulation and function of ribosomal protein S6 kinase (S6K) within mTOR signalling networks. Biochem J 441:1-21.

Maravall M, Mainen ZF, Sabatini BL, Svoboda K (2000) Estimating Intracellular Calcium Concentrations and Buffering without Wavelength Ratioing. Biophysical journal 78:2655-2667.

Martin RB (2006) Encyclopedia of Molecular Cell Biology and Molecular Medicine. In, 2 Edition (Meyers RA, ed).

Martinez Calejman C, Trefely S, Entwisle SW, Luciano A, Jung SM, Hsiao W, Torres A, Hung CM, Li H, Snyder NW, Villén J, Wellen KE, Guertin DA (2020) mTORC2-AKT signaling to ATP-citrate lyase drives brown adipogenesis and de novo lipogenesis. Nat Commun 11:575.

Maung MT, Carlson A, Olea-Flores M, Elkhadragy L, Schachtschneider KM, Navarro-Tito N, Padilla-Benavides T (2021) The molecular and cellular basis of copper dysregulation and its relationship with human pathologies. FASEB journal : official publication of the Federation of American Societies for Experimental Biology 35:e21810.

McAllum EJ, Hare DJ, Volitakis I, McLean CA, Bush AI, Finkelstein DI, Roberts BR (2020) Regional iron distribution and soluble ferroprotein profiles in the healthy human brain. Prog Neurobiol 186:101744.

McCann C, Quinteros M, Adelugba I, Morgada MN, Castelblanco AR, Davis EJ, Lanzirotti A, Hainer SJ, Vila AJ, Navea JG, Padilla-Benavides T (2022) The mitochondrial Cu(+) transporter PiC2 (SLC25A3) is a target of MTF1 and contributes to the development of skeletal muscle in vitro. Front Mol Biosci 9:1037941.

McNaughton PA, Cervetto L, Nunn BJ (1986) Measurement of the intracellular free calcium concentration in salamander rods. Nature 322:261-263.

Menkes JH, Alter M, Steigleder GK, Weakley DR, Sung JH (1962) A sex-linked recessive disorder with retardation of growth, peculiar hair, and focal cerebral and cerebellar degeneration. Pediatrics 29:764-779.

Merritt CR et al. (2020) Multiplex digital spatial profiling of proteins and RNA in fixed tissue. Nat Biotechnol 38:586-599.

Meyuhas O (2015) Ribosomal Protein S6 Phosphorylation: Four Decades of Research. Int Rev Cell Mol Biol 320:41-73.

Milo R, Jorgensen P, Moran U, Weber G, Springer M (2010) BioNumbers--the database of key numbers in molecular and cell biology. Nucleic Acids Research 38:D750-D753.

Miron M, Verdú J, Lachance PE, Birnbaum MJ, Lasko PF, Sonenberg N (2001) The translational inhibitor 4E-BP is an effector of PI(3)K/Akt signalling and cell growth in Drosophila. Nat Cell Biol 3:596-601.

Morgan MT, Bourassa D, Harankhedkar S, McCallum AM, Zlatic SA, Calvo JS, Meloni G, Faundez V, Fahrni CJ (2019) Ratiometric two-photon microscopy reveals attomolar copper buffering in normal and Menkes mutant cells. Proc Natl Acad Sci U S A 116:12167-12172.

Morita M, Gravel SP, Hulea L, Larsson O, Pollak M, St-Pierre J, Topisirovic I (2015) mTOR coordinates protein synthesis, mitochondrial activity and proliferation. Cell Cycle 14:473-480.

Morita M, Gravel SP, Chénard V, Sikström K, Zheng L, Alain T, Gandin V, Avizonis D, Arguello M, Zakaria C, McLaughlan S, Nouet Y, Pause A, Pollak M, Gottlieb E, Larsson O, St-Pierre J, Topisirovic I, Sonenberg N (2013) mTORC1 controls mitochondrial activity and biogenesis through 4E-BP-dependent translational regulation. Cell Metab 18:698-711.

Mounir Z, Krishnamoorthy JL, Wang S, Papadopoulou B, Campbell S, Muller WJ, Hatzoglou M, Koromilas AE (2011) Akt Determines Cell Fate Through Inhibition of the PERK-eIF2α Phosphorylation Pathway. Science Signaling 4:ra62-ra62.

Mukhopadhyay R, Roy S, Venkatadri R, Su YP, Ye W, Barnaeva E, Mathews Griner L, Southall N, Hu X, Wang AQ, Xu X, Dulcey AE, Marugan JJ, Ferrer M, Arav-Boger R (2016) Efficacy and Mechanism of Action of Low Dose Emetine against Human Cytomegalovirus. PLoS Pathog 12:e1005717.

Nagai M, Vo NH, Shin Ogawa L, Chimmanamada D, Inoue T, Chu J, Beaudette-Zlatanova BC, Lu R, Blackman RK, Barsoum J, Koya K, Wada Y (2012) The oncology drug elesclomol selectively transports copper to the mitochondria to induce oxidative stress in cancer cells. Free Radic Biol Med 52:2142-2150.

Navé BT, Ouwens M, Withers DJ, Alessi DR, Shepherd PR (1999) Mammalian target of rapamycin is a direct target for protein kinase B: identification of a convergence point for opposing effects of insulin and amino-acid deficiency on protein translation. Biochem J 344 Pt 2:427-431.

Niciu MJ, Ma XM, El Meskini R, Ronnett GV, Mains RE, Eipper BA (2006) Developmental changes in the expression of ATP7A during a critical period in postnatal neurodevelopment. Neuroscience 139:947-964.

Niciu MJ, Ma XM, El Meskini R, Pachter JS, Mains RE, Eipper BA (2007) Altered ATP7A expression and other compensatory responses in a murine model of Menkes disease. Neurobiol Dis 27:278-291.

Nopoulos PC (2016) Huntington disease: a single-gene degenerative disorder of the striatum. Dialogues Clin Neurosci 18:91-98.

Norgate M, Lee E, Southon A, Farlow A, Batterham P, Camakaris J, Burke R (2006) Essential roles in development and pigmentation for the Drosophila copper transporter DmATP7. Mol Biol Cell 17:475-484.

Ogawa E, Kodama H (2012) Effects of disulfiram treatment in patients with Menkes disease and occipital horn syndrome. Journal of Trace Elements in Medicine and Biology 26:102-104.

Ohgami RS, Campagna DR, McDonald A, Fleming MD (2006) The Steap proteins are metalloreductases. Blood 108:1388-1394.

Opazo CM, Greenough MA, Bush AI (2014a) Copper: from neurotransmission to neuroproteostasis. Frontiers in Aging Neuroscience 6.

Opazo CM, Greenough MA, Bush AI (2014b) Copper: from neurotransmission to neuroproteostasis. Frontiers in aging neuroscience 6:143-143.

Oyarzábal A, Musokhranova U, Barros L, García-Cazorla A (2021) Energy metabolism in childhood neurodevelopmental disorders. EBioMedicine 69.

Palm R, Wahlström G, Hallmans G (1990) Age related changes in weight and the concentrations of zinc and copper in the brain of the adult rat. Lab Anim 24:240-245.

Park SJ, Son SM, Barbosa AD, Wrobel L, Stamatakou E, Squitieri F, Balmus G, Rubinsztein DC (2024) Nuclear proteasomes buffer cytoplasmic proteins during autophagy compromise. Nat Cell Biol 26:1691-1699.

Peng Z, Aggarwal R, Zeng N, He L, Stiles EX, Debebe A, Chen J, Chen CY, Stiles BL (2020) AKT1 Regulates Endoplasmic Reticulum Stress and Mediates the Adaptive Response of Pancreatic β Cells. Mol Cell Biol 40.

Perea V, Baron KR, Dolina V, Aviles G, Rosarda JD, Guo X, Kampmann M, Wiseman RL (2023) Pharmacologic Activation of a Compensatory Integrated Stress Response Kinase Promotes Mitochondrial Remodeling in PERK-deficient Cells. bioRxiv.

Perez-Gomez R, Magnin V, Mihajlovic Z, Slaninova V, Krejci A (2020) Downregulation of respiratory complex I mediates major signalling changes triggered by TOR activation. Sci Rep 10:4401.

Perez-Riverol Y, Bai J, Bandla C, García-Seisdedos D, Hewapathirana S, Kamatchinathan S, Kundu DJ, Prakash A, Frericks-Zipper A, Eisenacher M, Walzer M, Wang S, Brazma A, Vizcaíno JA (2022) The PRIDE database resources in 2022: a hub for mass spectrometry-based proteomics evidences. Nucleic Acids Res 50:D543-d552.

Perrin L, Roudeau S, Carmona A, Domart F, Petersen JD, Bohic S, Yang Y, Cloetens P, Ortega R (2017) Zinc and Copper Effects on Stability of Tubulin and Actin Networks in Dendrites and Spines of Hippocampal Neurons. ACS Chem Neurosci 8:1490-1499.

Peters C, Muñoz B, Sepúlveda FJ, Urrutia J, Quiroz M, Luza S, De Ferrari GV, Aguayo LG, Opazo C (2011) Biphasic effects of copper on neurotransmission in rat hippocampal neurons. J Neurochem 119:78-88.

Peterson TR, Laplante M, Thoreen CC, Sancak Y, Kang SA, Kuehl WM, Gray NS, Sabatini DM (2009) DEPTOR is an mTOR inhibitor frequently overexpressed in multiple myeloma cells and required for their survival. Cell 137:873-886.

Pezacki AT, Matier CD, Gu X, Kummelstedt E, Bond SE, Torrente L, Jordan-Sciutto KL, DeNicola GM, Su TA, Brady DC, Chang CJ (2022) Oxidation state-specific fluorescent copper sensors reveal oncogene-driven redox changes that regulate labile copper(II) pools. Proceedings of the National Academy of Sciences 119:e2202736119.

Pham VN, Chang CJ (2023) Metalloallostery and Transition Metal Signaling: Bioinorganic Copper Chemistry Beyond Active Sites. Angewandte Chemie International Edition 62:e202213644.

Pierson H, Yang H, Lutsenko S (2019) Copper Transport and Disease: What Can We Learn from Organoids? Annu Rev Nutr 39:75-94.

Ping L, Duong DM, Yin L, Gearing M, Lah JJ, Levey AI, Seyfried NT (2018) Global quantitative analysis of the human brain proteome in Alzheimer's and Parkinson's Disease. Scientific Data 5:180036.

Polishchuk EV, Concilli M, Iacobacci S, Chesi G, Pastore N, Piccolo P, Paladino S, Baldantoni D, van ISC, Chan J, Chang CJ, Amoresano A, Pane F, Pucci P, Tarallo A, Parenti G, Brunetti-Pierri N, Settembre C, Ballabio A, Polishchuk RS (2014) Wilson disease protein ATP7B utilizes lysosomal exocytosis to maintain copper homeostasis. Dev Cell 29:686-700.

Popescu BF, George MJ, Bergmann U, Garachtchenko AV, Kelly ME, McCrea RP, Lüning K, Devon RM, George GN, Hanson AD, Harder SM, Chapman LD, Pickering IJ, Nichol H (2009) Mapping metals in Parkinson's and normal brain using rapid-scanning x-ray fluorescence. Phys Med Biol 54:651-663.

Popov LD (2020) Mitochondrial biogenesis: An update. J Cell Mol Med 24:4892-4899.

Poursani EM et al. (2023) Copper chelation suppresses epithelial-mesenchymal transition by inhibition of canonical and non-canonical TGF-β signaling pathways in cancer. Cell Biosci 13:132.

Pramatarova A, Figlewicz DA, Krizus A, Han FY, Ceballos-Picot I, Nicole A, Dib M, Meininger V, Brown RH, Rouleau GA (1995) Identification of new mutations in the Cu/Zn superoxide dismutase gene of patients with familial amyotrophic lateral sclerosis. American journal of human genetics 56:592-596.

Prasad PD, Wang H, Huang W, Kekuda R, Rajan DP, Leibach FH, Ganapathy V (1999) Human LAT1, a Subunit of System L Amino Acid Transporter: Molecular Cloning and Transport Function. Biochemical and Biophysical Research Communications 255:283-288.

Puck TT, Marcus PI, Cieciura SJ (1956) Clonal growth of mammalian cells in vitro; growth characteristics of colonies from single HeLa cells with and without a feeder layer. J Exp Med 103:273-283.

Pullen N, Dennis PB, Andjelkovic M, Dufner A, Kozma SC, Hemmings BA, Thomas G (1998) Phosphorylation and activation of p70s6k by PDK1. Science 279:707-710.

Purpura DP, Hirano A, French JH (1976) Polydendritic Purkinje cells in X-chromosome linked copper malabsorption: a Golgi study. Brain Res 117:125-129.

Pushkar Y, Robison G, Sullivan B, Fu SX, Kohne M, Jiang W, Rohr S, Lai B, Marcus MA, Zakharova T, Zheng W (2013) Aging results in copper accumulations in glial fibrillary acidic protein-positive cells in the subventricular zone. Aging Cell 12:823-832.

Qin X, Jiang B, Zhang Y (2016) 4E-BP1, a multifactor regulated multifunctional protein. Cell Cycle 15:781-786.

R Core Team (2021) R: A Language and Environment for Statistical Computing. In. Vienna: R Foundation for Statistical Computing.

Raab A, Feldmann J (2019) Biological sulphur-containing compounds - Analytical challenges. Anal Chim Acta 1079:20-29.

Rae TD, Schmidt PJ, Pufahl RA, Culotta VC, O'Halloran TV (1999) Undetectable intracellular free copper: the requirement of a copper chaperone for superoxide dismutase. Science 284:805-808.

Rajan A, Fame RM (2024) Brain development and bioenergetic changes. Neurobiol Dis 199:106550.

Raught B, Gingras AC, Gygi SP, Imataka H, Morino S, Gradi A, Aebersold R, Sonenberg N (2000) Serum-stimulated, rapamycin-sensitive phosphorylation sites in the eukaryotic translation initiation factor 4GI. Embo j 19:434-444.

Rauluseviciute I, Riudavets-Puig R, Blanc-Mathieu R, Castro-Mondragon JA, Ferenc K, Kumar V, Lemma RB, Lucas J, Chèneby J, Baranasic D, Khan A, Fornes O, Gundersen S, Johansen M, Hovig E, Lenhard B, Sandelin A, Wasserman WW, Parcy F, Mathelier A (2024) JASPAR 2024: 20th anniversary of the open-access database of transcription factor binding profiles. Nucleic Acids Res 52:D174-d182.

Rembach A, Hare DJ, Lind M, Fowler CJ, Cherny RA, McLean C, Bush AI, Masters CL, Roberts BR (2013) Decreased copper in Alzheimer's disease brain is predominantly in the soluble extractable fraction. Int J Alzheimers Dis 2013:623241-623241.

Reynolds THt, Bodine SC, Lawrence JC, Jr. (2002) Control of Ser2448 phosphorylation in the mammalian target of rapamycin by insulin and skeletal muscle load. J Biol Chem 277:17657-17662.

Richter JD, Zhao X (2021) The molecular biology of FMRP: new insights into fragile X syndrome. Nature Reviews Neuroscience 22:209-222.

Roberts BR, Ryan TM, Bush AI, Masters CL, Duce JA (2012) The role of metallobiology and amyloid-β peptides in Alzheimer's disease. J Neurochem 120 Suppl 1:149-166.

Rosen DR, Siddique T, Patterson D, Figlewicz DA, Sapp P, Hentati A, Donaldson D, Goto J, O'Regan JP, Deng HX, et al. (1993) Mutations in Cu/Zn superoxide dismutase gene are associated with familial amyotrophic lateral sclerosis. Nature 362:59-62.

Rosner M, Siegel N, Valli A, Fuchs C, Hengstschläger M (2010) mTOR phosphorylated at S2448 binds to raptor and rictor. Amino Acids 38:223-228.

Roux PP, Shahbazian D, Vu H, Holz MK, Cohen MS, Taunton J, Sonenberg N, Blenis J (2007) RAS/ERK signaling promotes site-specific ribosomal protein S6 phosphorylation via RSK and stimulates cap-dependent translation. J Biol Chem 282:14056-14064.

Roy S, Lutsenko S (2024) Mechanism of Cu entry into the brain: many unanswered questions. Neural Regen Res 19:2421-2429.

Rumble JR (2021) Chemical Composition Of The Human Body. In: CRC Handbook of Chemistry and Physics, 102nd Edition (Internet Version 2021) Edition: CRC Press/Taylor & Francis.

Sakai D, Murakami Y, Shigeta D, Tomosugi M, Sakata-Haga H, Hatta T, Shoji H (2023) Glycolytic activity is required for the onset of neural plate folding during neural tube closure in mouse embryos. Front Cell Dev Biol 11:1212375.

Sakai Y, Kassai H, Nakayama H, Fukaya M, Maeda T, Nakao K, Hashimoto K, Sakagami H, Kano M, Aiba A (2019) Hyperactivation of mTORC1 disrupts cellular homeostasis in cerebellar Purkinje cells. Sci Rep 9:2799.

Sancak Y, Thoreen CC, Peterson TR, Lindquist RA, Kang SA, Spooner E, Carr SA, Sabatini DM (2007) PRAS40 is an insulin-regulated inhibitor of the mTORC1 protein kinase. Mol Cell 25:903-915.

Sarkar B, Lingertat-Walsh K, Clarke JT (1993) Copper-histidine therapy for Menkes disease. J Pediatr 123:828-830.

Sato M, Ohtomo K, Daimon T, Sugiyama T, Iijima K (1994) Localization of copper to afferent terminals in rat locus ceruleus, in contrast to mitochondrial copper in cerebellum. J Histochem Cytochem 42:1585-1591.

Scalise M, Galluccio M, Console L, Pochini L, Indiveri C (2018) The Human SLC7A5 (LAT1): The Intriguing Histidine/Large Neutral Amino Acid Transporter and Its Relevance to Human Health. Frontiers in Chemistry 6:243.

Scanga R, Scalise M, Marino N, Parisi F, Barca D, Galluccio M, Brunocilla C, Console L, Indiveri C (2023) LAT1 (SLC7A5) catalyzes copper(histidinate) transport switching from antiport to uniport mechanism. iScience 26:107738.

Scarpulla RC, Vega RB, Kelly DP (2012) Transcriptional integration of mitochondrial biogenesis. Trends Endocrinol Metab 23:459-466.

Scheiber IF, Mercer JF, Dringen R (2010) Copper accumulation by cultured astrocytes. Neurochem Int 56:451-460.

Scheiber IF, Mercer JFB, Dringen R (2014) Metabolism and functions of copper in brain. Progress in Neurobiology 116:33-57.

Schlief ML, Craig AM, Gitlin JD (2005) NMDA receptor activation mediates copper homeostasis in hippocampal neurons. J Neurosci 25:239-246.

Schlief ML, West T, Craig AM, Holtzman DM, Gitlin JD (2006) Role of the Menkes copper-transporting ATPase in NMDA receptor-mediated neuronal toxicity. Proc Natl Acad Sci U S A 103:14919-14924.

Schmidt EK, Clavarino G, Ceppi M, Pierre P (2009) SUnSET, a nonradioactive method to monitor protein synthesis. Nat Methods 6:275-277.

Schneider CA, Rasband WS, Eliceiri KW (2012) NIH Image to ImageJ: 25 years of image analysis. Nat Methods 9:671-675.

Schoonover KE, Queern SL, Lapi SE, Roberts RC (2020) Impaired copper transport in schizophrenia results in a copper-deficient brain state: A new side to the dysbindin story. World J Biol Psychiatry 21:13-28.

Schoonover KE, Farmer CB, Morgan CJ, Sinha V, Odom L, Roberts RC (2021) Abnormalities in the copper transporter CTR1 in postmortem hippocampus in schizophrenia: A subregion and laminar analysis. Schizophr Res 228:60-73.

Schrag M, Mueller C, Oyoyo U, Smith MA, Kirsch WM (2011) Iron, zinc and copper in the Alzheimer's disease brain: a quantitative meta-analysis. Some insight on the influence of citation bias on scientific opinion. Prog Neurobiol 94:296-306.

Schulten A, Pietzenuk B, Quintana J, Scholle M, Feil R, Krause M, Romera-Branchat M, Wahl V, Severing E, Coupland G, Krämer U (2022) Energy status-promoted growth and development of Arabidopsis require copper deficiency response transcriptional regulator SPL7. Plant Cell 34:3873-3898.

Setty SR, Tenza D, Sviderskaya EV, Bennett DC, Raposo G, Marks MS (2008) Cell-specific ATP7A transport sustains copper-dependent tyrosinase activity in melanosomes. Nature 454:1142-1146.

Skjørringe T, Amstrup Pedersen P, Salling Thorborg S, Nissen P, Gourdon P, Birk Møller L (2017) Characterization of ATP7A missense mutants suggests a correlation between intracellular trafficking and severity of Menkes disease. Scientific reports 7:757-757.

Smeyers J, Banchi EG, Latouche M (2021) C9ORF72: What It Is, What It Does, and Why It Matters. Front Cell Neurosci 15:661447.

Smolen KA, Papke CM, Swingle MR, Musiyenko A, Li C, Salter EA, Camp AD, Honkanen RE, Kettenbach AN (2023) Quantitative proteomics and phosphoproteomics of PP2A-PPP2R5D variants reveal deregulation of RPS6 phosphorylation via converging signaling cascades. Journal of Biological Chemistry 299:105154.

Soma S, Latimer AJ, Chun H, Vicary AC, Timbalia SA, Boulet A, Rahn JJ, Chan SSL, Leary SC, Kim BE, Gitlin JD, Gohil VM (2018) Elesclomol restores mitochondrial function in genetic models of copper deficiency. Proc Natl Acad Sci U S A 115:8161-8166.

Song IS, Chen HH, Aiba I, Hossain A, Liang ZD, Klomp LW, Kuo MT (2008) Transcription factor Sp1 plays an important role in the regulation of copper homeostasis in mammalian cells. Mol Pharmacol 74:705-713.

Steiner P (2020) Brain fuel utilization in the developing brain. Annals of Nutrition and Metabolism 75:8-18.

Subramanian A, Tamayo P, Mootha VK, Mukherjee S, Ebert BL, Gillette MA, Paulovich A, Pomeroy SL, Golub TR, Lander ES, Mesirov JP (2005) Gene set enrichment analysis: a knowledge-based approach for interpreting genome-wide expression profiles. Proc Natl Acad Sci U S A 102:15545-15550.

Suryana E, Rowlands BD, Bishop DP, Finkelstein DI, Double KL (2024) Empirically derived formulae for calculation of age- and region-related levels of iron, copper and zinc in the adult C57BL/6 mouse brain. Neurobiol Aging 136:34-43.

Tashiro M, Tursun P, Konishi M (2005) Intracellular and Extracellular Concentrations of Na^+ Modulate Mg^{2+} Transport in Rat Ventricular Myocytes. Biophysical journal 89:3235-3247.

Tavera-Montañez C, Hainer SJ, Cangussu D, Gordon SJV, Xiao Y, Reyes-Gutierrez P, Imbalzano AN, Navea JG, Fazzio TG, Padilla-Benavides T (2019) The classic metal-sensing transcription factor MTF1 promotes myogenesis in response to copper. FASEB journal : official publication of the Federation of American Societies for Experimental Biology 33:14556-14574.

Telianidis J, Hung YH, Materia S, Fontaine SL (2013) Role of the P-Type ATPases, ATP7A and ATP7B in brain copper homeostasis. Frontiers in aging neuroscience 5:44-44.

Timón-Gómez A, Pérez-Pérez R, Nyvltova E, Ugalde C, Fontanesi F, Barrientos A (2020) Protocol for the Analysis of Yeast and Human Mitochondrial Respiratory Chain Complexes and Supercomplexes by Blue Native Electrophoresis. STAR Protoc 1.

Tokuda E, Furukawa Y (2016) Copper Homeostasis as a Therapeutic Target in Amyotrophic Lateral Sclerosis with SOD1 Mutations. International journal of molecular sciences 17:636.

Troost D, van Rossum A, Straks W, Willemse J (1982) Menkes' kinky hair disease. II. A clinicopathological report of three cases. Brain Dev 4:115-126.

Tsang T, Davis CI, Brady DC (2021) Copper biology. Curr Biol 31:R421-r427.

Tsang T, Posimo JM, Gudiel AA, Cicchini M, Feldser DM, Brady DC (2020) Copper is an essential regulator of the autophagic kinases ULK1/2 to drive lung adenocarcinoma. Nat Cell Biol 22:412-424.

Tsvetkov P, Coy S, Petrova B, Dreishpoon M, Verma A, Abdusamad M, Rossen J, Joesch-Cohen L, Humeidi R, Spangler RD, Eaton JK, Frenkel E, Kocak M, Corsello SM, Lutsenko S, Kanarek N, Santagata S, Golub TR (2022) Copper induces cell death by targeting lipoylated TCA cycle proteins. Science 375:1254-1261.

Tümer Z, Møller LB (2010) Menkes disease. Eur J Hum Genet 18:511-518.

Vagn-Hansen L, Reske-Nielsen E, Lou HC (1973) Menkes' disease--a new leucodystrophy (?). A clinical and neuropathological review together with a new case. Acta Neuropathol 25:103-119.

Vest KE, Paskavitz AL, Lee JB, Padilla-Benavides T (2018) Dynamic changes in copper homeostasis and post-transcriptional regulation of Atp7a during myogenic differentiation. Metallomics 10:309-322.

Viveiros A, Beliveau V, Panzer M, Schaefer B, Glodny B, Henninger B, Tilg H, Zoller H, Scherfler C (2021) Neurodegeneration in Hepatic and Neurologic Wilson's Disease. Hepatology 74:1117-1120.

Voli F, Valli E, Lerra L, Kimpton K, Saletta F, Giorgi FM, Mercatelli D, Rouaen JRC, Shen S, Murray JE, Ahmed-Cox A, Cirillo G, Mayoh C, Beavis PA, Haber M, Trapani JA, Kavallaris M, Vittorio O (2020) Intratumoral Copper Modulates PD-L1 Expression and Influences Tumor Immune Evasion. Cancer Res 80:4129-4144.

Waggoner DJ, Bartnikas TB, Gitlin JD (1999) The role of copper in neurodegenerative disease. Neurobiol Dis 6:221-230.
Walsh CT (2021) Chapter 1: Introduction to Phosphorus Chemical Biology. In: The Chemical Biology of Phosphorus, pp 3-26: The Royal Society of Chemistry.
Wang H, Xu J, Lazarovici P, Zheng W (2017) Dysbindin-1 Involvement in the Etiology of Schizophrenia. Int J Mol Sci 18.
Wang Y, Hekimi S (2021) Minimal mitochondrial respiration is required to prevent cell death by inhibition of mTOR signaling in CoQ-deficient cells. Cell Death Discov 7:201.
Wang Y, Zhu S, Hodgkinson V, Prohaska JR, Weisman GA, Gitlin JD, Petris MJ (2012) Maternofetal and neonatal copper requirements revealed by enterocyte-specific deletion of the Menkes disease protein. Am J Physiol Gastrointest Liver Physiol 303:G1236-1244.
Wilschefski SC, Baxter MR (2019) Inductively Coupled Plasma Mass Spectrometry: Introduction to Analytical Aspects. Clin Biochem Rev 40:115-133.
Wilson DM, 3rd, Cookson MR, Van Den Bosch L, Zetterberg H, Holtzman DM, Dewachter I (2023) Hallmarks of neurodegenerative diseases. Cell 186:693-714.
Wit N, Gogola E, West JA, Vornbäumen T, Seear RV, Bailey PSJ, Burgos-Barragan G, Wang M, Krawczyk P, Huberts D, Gergely F, Matheson NJ, Kaser A, Nathan JA, Patel KJ (2023) A histone deacetylase 3 and mitochondrial complex I axis regulates toxic formaldehyde production. Sci Adv 9:eadg2235.
Wittig I, Braun HP, Schägger H (2006) Blue native PAGE. Nat Protoc 1:418-428.
Wright EB, Lannigan DA (2023) Therapeutic targeting of p90 ribosomal S6 kinase. Front Cell Dev Biol 11:1297292.
Wu L, Zhou L, Liu DQ, Vogt FG, Kord AS (2011) LC-MS/MS and density functional theory study of copper(II) and nickel(II) chelating complexes of elesclomol (a novel anticancer agent). J Pharm Biomed Anal 54:331-336.
Wu Y, Liu W, Li L, Tai Z, Liu J-X (2023) Transcriptional profiles in zebrafish atp7a mutants and responses of atp7a mutants to Cu stress. Water Biology and Security 2:100186.
Wu Z, Zhang W, Kang YJ (2019) Copper affects the binding of HIF-1α to the critical motifs of its target genes. Metallomics 11:429-438.
Wynne ME, Lane AR, Singleton KS, Zlatic SA, Gokhale A, Werner E, Duong D, Kwong JQ, Crocker AJ, Faundez V (2021) Heterogeneous Expression of Nuclear Encoded Mitochondrial Genes Distinguishes Inhibitory and Excitatory Neurons. eNeuro 8:ENEURO.0232-0221.2021.
Wynne ME et al. (2023) APOE expression and secretion are modulated by mitochondrial dysfunction. eLife 12.
Yadav B, Wennerberg K, Aittokallio T, Tang J (2015) Searching for Drug Synergy in Complex Dose-Response Landscapes Using an Interaction Potency Model. Comput Struct Biotechnol J 13:504-513.
Yajima K, Suzuki K (1979) Neuronal Degeneration in the Brain of the Brindled Mouse—A Light Microscope Study. Journal of Neuropathology & Experimental Neurology 38:35-46.
Yamano T, Suzuki K (1985) Abnormalities of Purkinje cell arborization in brindled mouse cerebellum. A Golgi study. J Neuropathol Exp Neurol 44:85-96.
You H, Tsutsui S, Hameed S, Kannanayakal TJ, Chen L, Xia P, Engbers JD, Lipton SA, Stys PK, Zamponi GW (2012) Aβ neurotoxicity depends on interactions between copper ions, prion protein, and N-methyl-D-aspartate receptors. Proc Natl Acad Sci U S A 109:1737-1742.
Yuan S, Korolnek T, Kim BE (2022) Oral Elesclomol Treatment Alleviates Copper Deficiency in Animal Models. Front Cell Dev Biol 10:856300.
Zeng H, Saari JT, Johnson WT (2007) Copper deficiency decreases complex IV but not complex I, II, III, or V in the mitochondrial respiratory chain in rat heart. J Nutr 137:14-18.
Zhang Z, Qiu L, Lin C, Yang H, Fu H, Li R, Kang YJ (2014) Copper-dependent and -independent hypoxia-inducible factor-1 regulation of gene expression. Metallomics 6:1889-1893.

Zheng P, Zhou C, Lu L, Liu B, Ding Y (2022) Elesclomol: a copper ionophore targeting mitochondrial metabolism for cancer therapy. Journal of Experimental & Clinical Cancer Research 41:271.

Zheng X, Boyer L, Jin M, Mertens J, Kim Y, Ma L, Ma L, Hamm M, Gage FH, Hunter T (2016) Metabolic reprogramming during neuronal differentiation from aerobic glycolysis to neuronal oxidative phosphorylation. Elife 5.

Zheng Y, Jiang Y (2015) mTOR Inhibitors at a Glance. Mol Cell Pharmacol 7:15-20.

Zheng Z, White C, Lee J, Peterson TS, Bush AI, Sun GY, Weisman GA, Petris MJ (2010) Altered microglial copper homeostasis in a mouse model of Alzheimer's disease. J Neurochem 114:1630-1638.

Zhou Y, Zhou B, Pache L, Chang M, Khodabakhshi AH, Tanaseichuk O, Benner C, Chanda SK (2019) Metascape provides a biologist-oriented resource for the analysis of systems-level datasets. Nat Commun 10:1523.

Zlatic S, Comstra HS, Gokhale A, Petris MJ, Faundez V (2015) Molecular basis of neurodegeneration and neurodevelopmental defects in Menkes disease. Neurobiol Dis 81:154-161.

Zlatic SA, Vrailas-Mortimer A, Gokhale A, Carey LJ, Scott E, Burch R, McCall MM, Rudin-Rush S, Davis JB, Hartwig C, Werner E, Li L, Petris M, Faundez V (2018) Rare Disease Mechanisms Identified by Genealogical Proteomics of Copper Homeostasis Mutant Pedigrees. Cell Syst 6:368-380.e366.

Zollinger DR, Lingle SE, Sorg K, Beechem JM, Merritt CR (2020) GeoMx™ RNA Assay: High Multiplex, Digital, Spatial Analysis of RNA in FFPE Tissue. Methods Mol Biol 2148:331-345.